

UNIVERSITÁ DEGLI STUDI DI NAPOLI FEDERICO II

DIPARTIMENTO DI FISICA "ETTORE PANCINI"

Dottorato di Ricerca in Fisica Fondamentale e Applicata

CICLO XXVIII

2013-2016



Tesi di Dottorato

**CHANTI: a fast and efficient charged  
particle veto detector for the NA62  
experiment at CERN**

Supervisor: Prof. Fabio Ambrosino

Candidate: Dott. Marco Mirra

# Contents

<b>Introduction</b>	<b>1</b>
<b>1 The <math>K \rightarrow \pi\nu\bar{\nu}</math> decay</b>	<b>4</b>
1.1 CKM matrix and unitary triangle . . . . .	5
1.2 Branching ratio of the $K^+ \rightarrow \pi^+\nu\bar{\nu}$ . . . . .	7
1.3 Impact of BR( $K \rightarrow \pi\nu\bar{\nu}$ ) measurement on SM . . . . .	11
1.4 $K^+ \rightarrow \pi^+\nu\bar{\nu}$ experimental status . . . . .	14
<b>2 The NA62 experiment</b>	<b>19</b>
2.1 NA62 experimental strategy . . . . .	21
2.2 Main background rejection . . . . .	26
2.3 Beam line . . . . .	27
2.4 Kaon identification and tracking system . . . . .	29
2.4.1 KTAG . . . . .	29
2.4.2 GTK . . . . .	31
2.5 Pion tracking, identification and timing system . . . . .	32
2.5.1 STRAW . . . . .	32
2.5.2 RICH . . . . .	34
2.5.3 MUV 1-2 . . . . .	35
2.5.4 CHOD and NEW CHOD . . . . .	37
2.6 Veto system . . . . .	38
2.6.1 CHANTI . . . . .	39
2.6.2 Photon Veto detectors . . . . .	39
LAV . . . . .	40
LKr . . . . .	41
IRC and SAC . . . . .	43

2.6.3	MUV3 . . . . .	44
2.7	Trigger and data acquisition . . . . .	45
<b>3</b>	<b>The detector CHANTI: design and construction</b>	<b>48</b>
3.1	Detector requirements . . . . .	49
3.2	Basic elements of the detector . . . . .	50
3.2.1	Scintillators . . . . .	50
3.2.2	Optical fibers . . . . .	51
3.2.3	Silicon photomultiplier . . . . .	53
3.3	Layout and assembly . . . . .	54
3.3.1	SiPMs test . . . . .	56
3.3.2	Preparation of the bars with their fibers and connectors for SiPM . . . . .	57
3.3.3	Test of the bars . . . . .	57
3.3.4	Assembly of the station . . . . .	59
3.4	Detector rate . . . . .	61
<b>4</b>	<b>CHANTI front end electronics: calibration and signal simulation</b>	<b>71</b>
4.1	CHANTI-FE board . . . . .	71
4.1.1	CHANTI-FE description . . . . .	72
4.1.2	CHANTI-FE calibration . . . . .	73
4.2	ToT board . . . . .	80
4.2.1	ToT board description . . . . .	80
4.2.2	ToT board calibration . . . . .	82
4.3	Validation of the calibration procedure . . . . .	87
4.4	Simulation of SiPM signal . . . . .	89
<b>5</b>	<b>Detector performance</b>	<b>100</b>
5.1	CHANTI during the NA62 run in 2015 . . . . .	100
5.2	Time resolution . . . . .	103
5.3	Detection efficiency . . . . .	106
5.4	Spatial resolution . . . . .	109
5.5	Accidental veto . . . . .	109
5.5.1	Selection of $K_{2\pi}$ sample . . . . .	110
5.5.2	Selection of $K_{\mu 2}$ sample . . . . .	120

5.5.3	CHANTI fake veto for $K_{2\pi}$ and $K_{\mu 2}$ . . . . .	123
	<b>Conclusions</b>	<b>129</b>
	<b>Bibliography</b>	<b>131</b>

# Introduction

In 1947 Rochester and Butler [1] recorded two photographs (see figure 1) from a cloud chamber that opened new frontiers in particle physics: they observed, for the first time, neutral and charged kaons. Mesons K showed a strange behaviour

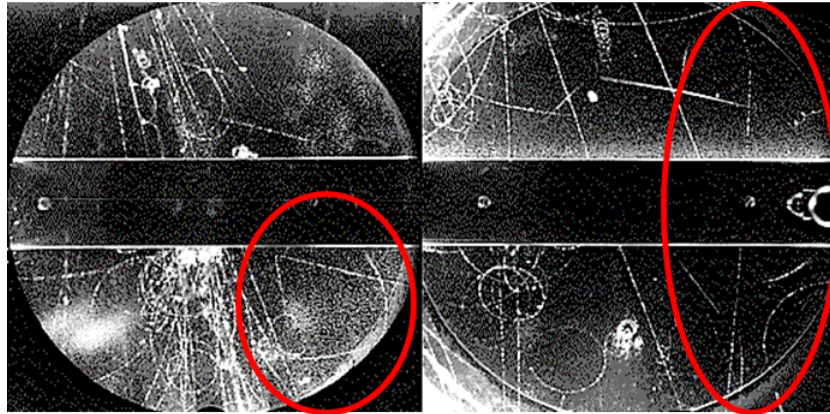


Figure 1: The two photos recorded by Rochester and Butler in 1947 with a cloud chamber. In the red circle it is possible to recognize the decay of a neutral kaon (on the left) and the one of a charged kaon (on the right).

never observed until then, or with Rochester's and Butler's words

*containing forked tracks of a very striking character.*

Indeed these particles were produced in strong interactions but their decays were due to weak interactions. Thus a new generation of particles and a new quantum number called strangeness were introduced. Kaon discovery marked the beginning of a very exciting epoch in particle physics that led to the observation of the oscillating  $K^0 - \bar{K}^0$  system and of the CP violation. Seventy years later, kaons have not revealed all their secrets yet. Today ultra-rare kaon decays represent one

of the main door towards the physics beyond the Standard Model, the current theoretical framework that describes in detail particle physics. Among the rare decays,  $K^+ \rightarrow \pi^+ \nu \bar{\nu}$  process is one of the most promising and it will be studied by the NA62 experiment. NA62 is performed at CERN North Area and it will use a 75 GeV/c unseparated beam with a 6% kaon component. The apparatus is designed to collect the kaon decays in flight within a 60 m long evacuated fiducial volume. To suppress backgrounds which are up to  $10^{10}$  times higher than the signal, kinematic rejection, by means of an accurate measurement of the kaon and pion momentum, particle identification and veto systems have been implemented. This work has been performed in the frame of the NA62 experiment and it was focused on the veto subsystem named CHANTI. The latter is a detector placed just after the last station of the kaon tracking system (called Giga Tracker or GTK). GTK is made of three silicon stations hit by the 750 MHz incoming beam of hadrons. Particles crossing the GTK can undergo inelastic collision in which the incoming hadron strongly interacts with nuclei of the GTK station producing many particles, among them pions: a signal  $K^+ \rightarrow \pi^+ \nu \bar{\nu}$  event could be mimicked if only a pion is detected. The Naples group proposed CHANTI in 2009 to veto these events detecting particles produced together with a pion. It is made by a series of guard rings made by X and Y scintillating bars. Bars have a triangular shape, thus are naturally staggered. Each bar is read through a Wave Length Shifter fiber coupled to a Silicon PhotoMultiplier. The role of this detector in NA62 and its design, simulation, construction and performance evaluation are the main subjects of the present work. The plan of the thesis is as follows.

- First two chapters introduce the motivation for the NA62 experiment, give an almost detailed description of the apparatus and present the measurement strategy.
- The third chapter describes the construction procedure of CHANTI, together with a simulation that helped to refine the design of the detector and to obtain information about the rate.
- The full front-end electronics is presented in the fourth chapter: a calibration procedure of the boards was implemented and it was very useful in order to help the design of the boards itself and to provide a high accuracy in the control of the working point of the detector.

- Finally the performance of CHANTI are reported in the last chapter. Efficiency, time/spatial resolution and fake veto are evaluated with the data collected in the first physics run of NA62.

The arguments concerning CHANTI treated in this thesis have also been partially reported in [2].

# Chapter 1

## The $K \rightarrow \pi\nu\bar{\nu}$ decay

The flavor physics program allows exploring the possible extensions of the Standard Model (SM) with an approach complementary to the one adopted in direct searches i.e. at the Large Hadron Collider (LHC). It is based on the idea that new physics contributions at high energy scales can manifest itself also in low energy phenomena provided that the observables are carefully chosen, precisely measured and compared to accurate predictions. In order to provide a stringent test of the SM predictions or lead to a discovery of deviations from the SM which turns into evidence of new physics, one of the most promising process that can be studied for this purpose is the ultra rare decay  $K^+ \rightarrow \pi^+\nu\bar{\nu}$ .

Among the many rare flavour changing neutral current (FCNC)  $K$  and  $B$  decays, the ultra rare decays  $K \rightarrow \pi\nu\bar{\nu}$  play a key role in the search for new physics through underlying mechanisms of flavour mixing. The branching ratio (BR) of this process can be theoretically computed to an exceptionally high degree of precision: the prediction for the  $K^+ \rightarrow \pi^+\nu\bar{\nu}$  channel is  $(9.11 \pm 0.72) \times 10^{-11}$  [3]. This decay is one of the best probes for new physics effects complementary to direct searches, especially within non Minimal Flavour Violation models [4][5]. Within the SM, the BR value provides a measurement of  $|V_{td}V_{td}^*|$  free from hadronic uncertainties and independent from that obtained from  $B$  meson decays.

The decay  $K^+ \rightarrow \pi^+\nu\bar{\nu}$  has been observed by the dedicated experiments E787 and E949 at the Brookhaven National Laboratory (see section 1.4) and the result is  $\text{BR}(K^+ \rightarrow \pi^+\nu\bar{\nu}) = (1.73_{-10.5}^{+1.15}) \times 10^{-10}$  [6]. However only a measurement of the BR with at least 10% accuracy can be a significant test of new physics.

## 1.1 CKM matrix and unitary triangle

The Cabibbo  $2 \times 2$  matrix describes the quark  $u, d, s$  and  $c$  flavour-mixing in weak decays within the SM. The unitary  $3 \times 3$  quark-mixing Cabibbo-Kobayashi-Maskawa (CKM) matrix generalizes the Cabibbo one by including the third generation of quark states  $(t, b)$  [7]:

$$\begin{pmatrix} d' \\ s' \\ b' \end{pmatrix} = \begin{pmatrix} V_{ud} & V_{us} & V_{ub} \\ V_{cd} & V_{cs} & V_{cb} \\ V_{td} & V_{ts} & V_{tb} \end{pmatrix} \begin{pmatrix} d \\ s \\ b \end{pmatrix} \quad (1.1)$$

The matrix can be expressed in the Wolfenstein parametrization [8]:

$$\begin{pmatrix} 1 - \lambda^2/2 & \lambda & A\lambda^3(\rho - i\eta) \\ -\lambda & 1 - \lambda^2/2 & A\lambda^2 \\ A\lambda^3(1 - \rho - i\eta) & -A\lambda^2 & 1 \end{pmatrix} + O(\lambda^4) \quad (1.2)$$

where  $\lambda$  is used as an expansion parameter.  $A$ ,  $\lambda$ ,  $\eta$  and  $\rho$  satisfy the relations:

$$\lambda = \sin\theta_{12} \quad A\lambda^2 = \sin\theta_{23} \quad A\lambda^3(\rho - i\eta) = \sin\theta_{13}e^{-i\phi} \quad (1.3)$$

where  $\theta_{ij}$  denote three real parameters (Cabibbo-like angles) and  $e^{-i\phi}$  is a phase factor encoding the  $CP$  violation. The CKM matrix unitarity gives nine conditions on the CKM matrix elements: three equations on the diagonal elements and six other vanishing combinations for the off-diagonal terms:

$$\sum_i V_{ij}V_{ik}^* = \delta_{jk} \quad \sum_i V_{ij}V_{kj}^* = \delta_{ik} \quad (1.4)$$

where  $i = u, c, t$  and  $j, k = d, s, b$  and  $\delta_{ij}$  is the Kronecker delta. The unitarity property of CKM matrix can be used to test the SM flavor sector: a way to do this is to measure the CKM matrix elements and monitor any significant deviation from unitarity. The three equations on the diagonal elements constrain the CKM elements magnitude and express the universality of the weak interaction, while the six vanishing combinations can be thought as triangles in a complex plane. Indeed one of these equations can be written as:

$$0 = V_{ud}V_{ub}^* + V_{cd}V_{cb}^* + V_{td}V_{tb}^* \Rightarrow 1 + \frac{V_{td}V_{tb}^*}{V_{cd}V_{cb}^*} + \frac{V_{ud}V_{ub}^*}{V_{cd}V_{cb}^*} = 0 \quad (1.5)$$

The expression can be seen as the sum of three vectors in a complex plane defined by the parameters

$$\bar{\rho} = \rho(1 - \lambda^2/2) \quad \bar{\eta} = \eta(1 - \lambda^2/2) \quad (1.6)$$

and represented with the triangle in figure 1.1.

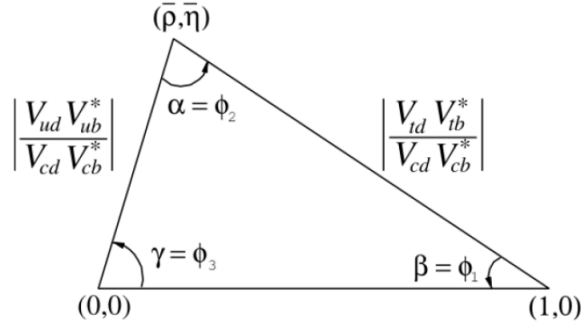


Figure 1.1: Unitary triangle for equation 1.5.

The vertexes of the triangle are  $(0, 0)$ ,  $(1, 0)$ ,  $(\bar{\rho}, \bar{\eta})$ , while the angles of the unitarity triangle in are:

$$\begin{aligned} \alpha = \phi_1 &= \arg \left( -\frac{V_{td}V_{tb}^*}{V_{ud}V_{ub}^*} \right) \\ \beta = \phi_2 &= \arg \left( -\frac{V_{cd}V_{cb}^*}{V_{td}V_{tb}^*} \right) \\ \gamma = \phi_3 &= \arg \left( -\frac{V_{ud}V_{ub}^*}{V_{cd}V_{cb}^*} \right) \end{aligned} \quad (1.7)$$

The current experimental status of the magnitude of CKM elements is summarized in the following [9]:

$$\begin{pmatrix} |V_{ud}| = 0.97425 \pm 0.00022 & |V_{us}| = 0.2252 \pm 0.0009 & |V_{ub}| = (4.15 \pm 0.49) \times 10^{-3} \\ |V_{cd}| = 0.230 \pm 0.011 & |V_{cs}| = 1.006 \pm 0.023 & |V_{cb}| = (40.9 \pm 1.1) \times 10^{-3} \\ |V_{td}| = (8.4 \pm 0.6) \times 10^{-3} & |V_{ts}| = (42.9 \pm 2.6) \times 10^{-3} & |V_{tb}| = 0.89 \pm 0.07 \end{pmatrix} \quad (1.8)$$

It is worth noticing that the diagonal elements are the dominant ones, reflecting the transitions  $u \rightarrow d, c \rightarrow s$  and  $t \rightarrow b$  which are the most allowed. The off-diagonal elements represent transitions suppressed at a certain level, depending

on their amplitude.

In particular the determination of  $|V_{td}|$  and  $|V_{ts}|$  is based on the measurements of the mass difference of two neutral  $B^0$  meson mass eigenstates performed by the CDF [10] and LHCb [11] experiments. A theoretically clean and independent measurement of  $|V_{td}V_{ts}^*|$  is possible from the  $K^+ \rightarrow \pi^+ \nu \bar{\nu}$  decay.

## 1.2 Branching ratio of the $K^+ \rightarrow \pi^+ \nu \bar{\nu}$

The transitions  $K^+ \rightarrow \pi^+ \nu \bar{\nu}$  and  $K_L \rightarrow \pi^0 \nu \bar{\nu}$  are very interesting in SM because the measurement of their decay rates provides important information about some of the less well-known fundamental physics parameters of the model. In fact, for these transitions the branching ratios are theoretically predicted in the SM and the purely theoretical (i.e. not related to experimentally measured quantities) relative uncertainties are well known, both for  $\text{BR}(K^+ \rightarrow \pi^+ \nu \bar{\nu})$  and for  $\text{BR}(K_L \rightarrow \pi^0 \nu \bar{\nu})$  [3]. The calculations show the sensitivity of these decay rates to the magnitude of the  $V_{td}$  element of CKM matrix, which can be determined with few percent accuracy without relying on unitarity constraints. Moreover simultaneous BR measurements of  $K^+ \rightarrow \pi^+ \nu \bar{\nu}$  and  $K_L \rightarrow \pi^0 \nu \bar{\nu}$  decays provide determinations of CKM parameters and the unitarity triangle in a complementary and independent way with respect to the study of  $B$  decays.

In the SM the quark level process that contribute to the  $K^+ \rightarrow \pi^+ \nu \bar{\nu}$  decay is the flavour changing quark transition  $s \rightarrow d \nu \bar{\nu}$  described, at first non-null order, by the one-loop diagram shown in figure 1.2: penguin diagrams with  $Z$  exchange and box diagrams with  $W$  exchange. In fact neutral flavour-changing transitions such as  $s \rightarrow d$  are forbidden at tree-level. The  $u$ ,  $c$ , and  $t$  quarks, that appear as internal lines, contribute to the amplitude with terms which are positive power of  $x_q = m_q^2/M_W^2$  (where  $m_q$  is the quark mass and  $M_W$  is the  $W$  boson mass. Because of its mass, the top-quark contribution becomes the dominant term and the transition  $s \rightarrow d$  is described by short-distance quark dynamics. In this scenarios the effective Hamiltonian relevant for  $K^+ \rightarrow \pi^+ \nu \bar{\nu}$  decay can be written in the SM as follows [12]:

$$H_{eff}^{SM} = \frac{G_F}{\sqrt{2}} \frac{\alpha}{2\pi \sin^2 \theta_W} \sum_{l=e,\mu,\tau} (V_{cs}^* V_{cd} X^l + V_{ts}^* V_{td} X(x_t)) (\bar{s}d)_{V-A} (\bar{\nu}_l \nu_l)_{V-A} \quad (1.9)$$

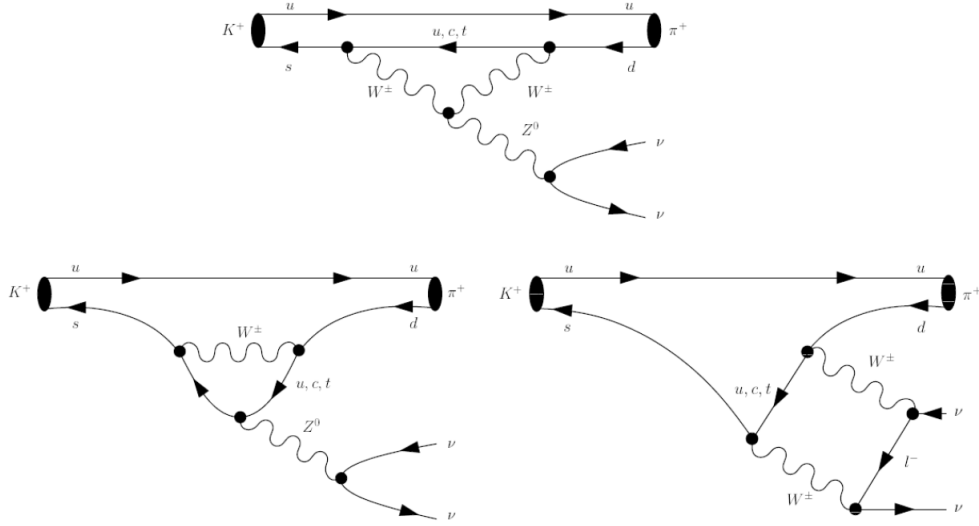


Figure 1.2: The penguin and box diagrams contributing to  $K^+ \rightarrow \pi^+ \nu \bar{\nu}$ . For  $K_L \rightarrow \pi^0 \nu \bar{\nu}$  the spectator quark is changed from  $u$  to  $d$ .

where

- $G_F$  is the Fermi coupling constant
- $\alpha$  is the fine-structure constant
- $\theta_W$  is the Weinberg angle (weak mixing angle)
- $s, d, \nu$  are the Dirac spinors for the respective particles, while  $(\bar{s}d)_{V-A}$   $(\bar{\nu}_l \nu_l)_{V-A}$  are the quark and lepton neutral weak currents with vector-axial (V - A) structure,
- $X_l$  with  $l = e, \mu, \tau$  are three functions describing the charm-quark contribution in the loop
- $X(x_t)$  is a function encoding the dominant top-quark loop contribution to the  $K^+ \rightarrow \pi^+ \nu \bar{\nu}$  decay.

Summing over three neutrino flavours, the BR of  $K^+ \rightarrow \pi^+ \nu \bar{\nu}$  can be written as follows [12][16]:

$$\text{BR}(K^+ \rightarrow \pi^+ \nu \bar{\nu}) = \kappa_+ (1 + \Delta_{EM}) \cdot \left[ \left( \frac{\text{Im} \lambda_t}{\lambda^5} X(x_t) \right)^2 + \left( \frac{\text{Re} \lambda_c}{\lambda} P_c(X) + \frac{\text{Re} \lambda_t^5}{\lambda} X(x_t) \right)^2 \right] \quad (1.10)$$

Here  $\lambda = |V_{us}|$ ,  $\lambda_i = V_{is}^* V_{id}$ ,  $\Delta_{EM} = -0.003$  (it describes the electromagnetic radiative correction from photon exchanges) and  $\kappa_+$  contains the hadronic matrix element along with electroweak corrections. The hadronic matrix element can be extracted from the well measured semi-leptonic decays  $K^+ \rightarrow \pi^0 e^+ \nu_e$  [16]:

$$\kappa_+ = r_{K^+} \frac{3\alpha^2 \text{BR}(K^+ \rightarrow \pi^0 e^+ \nu_e)}{2\pi^2 \sin^4 \theta_W} \lambda^8 \quad (1.11)$$

taking into account isospin breaking corrections, given by  $r_{K^+} = 0.901$  [22]. The result is

$$\kappa_+ = (5.173 \pm 0.025) \times 10^{-11} \left[ \frac{\lambda}{0.225} \right]^8 \quad (1.12)$$

The short distance function  $X(x_t)$  relevant for the top quark contribution, including NLO QCD corrections [12][17][18] and two-loop electroweak contributions [19], is

$$X(x_t) = 1.481 \pm 0.005_{th} \pm 0.008_{exp} \quad (1.13)$$

The first error comes from the remaining renormalisation scale and scheme uncertainties, while the second one corresponds to the combined experimental error on the top and W masses entering the ratio  $x_t$ , and on the strong coupling  $\alpha_s(M_Z)$ . The central value and errors in 1.13 have been obtained using full NNLO precision [20]; the NLO EW correction has been included, using the result presented in [19]. The parameter  $P_c(X)$  summarises the charm contribution and is defined through

$$P_c(X) = P_c^{SD}(X) + \delta P_{c,u} \quad \delta P_{c,u} = 0.04 \pm 0.02 \quad (1.14)$$

with the long-distance contributions  $\delta P_{c,u}$  calculated in [21]. The short-distance part is given by

$$P_c^{SD}(X) = \frac{1}{\lambda^4} \left[ \frac{2}{3} X_{NNL}^e + \frac{1}{3} X_{NNL}^T \right] \quad (1.15)$$

where the functions  $X_{NNL}^l$  (the index  $l$  distinguishes between the charged lepton flavours in the box diagrams) result from QCD NLO [12][23] and NNLO calculations [24][25]. They also include complete two-loop electroweak contributions [26]. This distinction is irrelevant in the top contribution due to  $m_t \gg m_l$  but is relevant in the charm contribution as  $m_\tau > m_c$ . Using this formula for the most recent input parameters [27] [71]

$$\lambda = 0.2252(9) \quad m_c = 1.279(13) \text{ GeV} \quad \alpha_s(M_Z) = 0.1185(6) \quad (1.16)$$

we find

$$P_c(X) = 0.404 \pm 0.024 \quad (1.17)$$

In order to evaluate the  $\text{BR}(K^+ \rightarrow \pi^+\nu\bar{\nu})$ , two strategies for the determination of the contribution of the SM dynamics can be considered [3].

- In the first strategy the CKM matrix elements are determined using tree-level measurements of  $|V_{us}|$ ,  $|V_{cb}|$ ,  $|V_{ub}|$  and  $\gamma$ . Since up to now new physics seems to be well separated from the electroweak scale, inserting these inputs into the known expression of  $\text{BR}(K^+ \rightarrow \pi^+\nu\bar{\nu})$  allows a determination of the SM value for this quantity, independently of whether new physics is present at short distance scales or not. The discrepancy of these predictions from future data would therefore allow us to discover whether new physics contributes to these decays independently of whether it contributes to other decays or not. This information is clearly important for the selection of successful extensions of the SM through flavour-violating processes. Unfortunately, this strategy cannot be executed in a satisfactory manner at present due to the discrepancies on  $|V_{cb}|$ ,  $|V_{ub}|$  from tree-level decays. Moreover, the precision on  $\gamma$  from tree-level decays is still unsatisfactory for this purpose.
- In the second strategy it is possible to assume that the SM is the whole story and all available information from FCNC processes is used to determine the CKM matrix. This strategy ignores tree-level determinations of  $|V_{ub}|$ ,  $|V_{cb}|$  and  $\gamma$ ; then the observables to be used for the determination of the CKM parameters  $\beta$ ,  $|V_{cb}|$ ,  $|V_{ub}|$ ,  $|V_{td}|$  and  $|V_{ts}|$  will be:
  - $\epsilon_K$ , the value of the indirect CP violation in the neutral kaon system
  - $\Delta M_s$ , the mass difference measured in the  $B_s^0 - \bar{B}_s^0$

- $\Delta M_d$ , the mass difference measured in the  $B_d^0 - \bar{B}_d^0$
- $S_{\Psi K_S}$ , the amplitude of the  $B \rightarrow \Psi K_S$  channel
- $|V_{us}|$ , the  $\lambda$  parameter of the CKM matrix

In this manner also  $|V_{cb}|$ ,  $|V_{ub}|$  and  $\gamma$  can be determined. This is basically what the UTfit [29] and CKMfitter [30] collaborations do, except that the tree-level determinations of  $|V_{cb}|$ ,  $|V_{ub}|$  are ignored.

Clearly the absence of new physics effects in all the loop observables listed in the second strategy requires the SM to be valid up to a reasonably high energy scale, which is a stronger assumption with respect to the one of the first strategy, where only tree-level determinations of CKM parameters were assumed to be free of new physics effects. It should be emphasised that while the first strategy is ultimately the one to use to study extensions of the SM, the virtue of the second one at present is the greater accuracy of the SM predictions for the observables that we consider, so we will refer to the latter one. Once the input parameters have been fixed, it is possible to perform a simultaneous fit to all the four observables  $\Delta M_s$ ,  $\Delta M_d$ ,  $S_{\Psi K_S}$  and  $\epsilon_K$ . Having determined the full CKM matrix in this manner, predictions for rare decays branching ratios can be made. In particular we have [3]:

$$\text{BR}(K^+ \rightarrow \pi^+\nu\bar{\nu}) = (9.11 \pm 0.72) \times 10^{-11} \quad (1.18)$$

### 1.3 Impact of $\text{BR}(K \rightarrow \pi\nu\bar{\nu})$ measurement on SM

Measured values of BR for the process  $K^+ \rightarrow \pi^+\nu\bar{\nu}$  and  $K_L \rightarrow \pi^0\nu\bar{\nu}$  can be put back into the SM in order to help to constrain the CKM matrix and unitarity triangle. In a similar fashion as in the  $K^+ \rightarrow \pi^+\nu\bar{\nu}$  decay, the  $\text{BR}(K_L \rightarrow \pi^0\nu\bar{\nu})$  can be evaluated [13][14]:

$$\text{BR}(K_L \rightarrow \pi^0\nu\bar{\nu}) = \kappa_L \cdot \left( \frac{\text{Im}\lambda_t}{\lambda^5} X(x_t) \right)^2 \quad (1.19)$$

with [16]

$$\kappa_L = r_{K_L} \frac{3\alpha^2 \text{BR}(K_L \rightarrow \pi^\pm e^\mp \nu)}{2\pi^2 \sin^4 \theta_W} \lambda^8 = (2.231 \pm 0.013) \times 10^{-10} \left[ \frac{\lambda}{0.225} \right]^8 \quad (1.20)$$

The main difference with the  $K^+ \rightarrow \pi^+ \nu \bar{\nu}$  decay is that the  $K_L \rightarrow \pi^0 \nu \bar{\nu}$  one is CP violating (it depends just from the imaginary part of the  $\lambda_t$  parameter) and there is no contribution from  $c$  quark.

In the Wolfenstein parametrization, the charged decay mode branching ratio can be expressed as:

$$\text{BR}(K^+ \rightarrow \pi^+ \nu \bar{\nu}) = \bar{\kappa}_+ |V_{cb}|^4 X^2(x_t) \frac{1}{\sigma} [(\sigma \bar{\eta})^2 + (\rho_c - \bar{\rho})^2] \quad (1.21)$$

where

$$\bar{\kappa} = \frac{\kappa}{\lambda^8} \quad \sigma = \left( \frac{1}{1 - (\lambda^2/2)} \right)^2 \quad \rho_c = 1 + \frac{\lambda^4 P_c^{SD}}{|V_{cb}|^2 X(x_t)} \quad (1.22)$$

This means that a measured value of  $B(K^+ \rightarrow \pi^+ \nu \bar{\nu})$  determines an ellipse in the  $(\bar{\rho}, \bar{\eta})$  plane, centred at  $(\rho_c, 0)$ . The fact that  $\rho_c \neq 1$  is due to the charm contribution to the decay. Finally, a combination of measurements of the two modes can lead to a measurement of  $\sin 2\beta$ , in which many of the parametric uncertainties cancel. Defining the reduced branching ratios

$$B_1 = \frac{\text{BR}(K^+ \rightarrow \pi^+ \nu \bar{\nu})}{\kappa_+} \quad B_2 = \frac{\text{BR}(K_L \rightarrow \pi^0 \nu \bar{\nu})}{\kappa_L} \quad (1.23)$$

it can be shown that

$$\cot \beta = \sqrt{\sigma} \frac{\sqrt{\sigma(B_1 - B_2)} - P_c^{SD}(X)}{\sqrt{B_2}} \quad (1.24)$$

which depends only on the two measurable branching ratios and the parameter  $P_c$ , so it is free from the hadronic uncertainties in  $X(x_t)$ . A measurement of  $\sin 2\beta$ , independent of the measurements from  $B$  physics, provides a strong test of the SM and Minimal Flavour Violation (MFV) models, in which the structure of CP-violating transitions is still governed by the CKM matrix [15].

The current generation of rare kaon decay experiments is expected to measure the branching ratios of  $K^+ \rightarrow \pi^+ \nu \bar{\nu}$  and  $K_L \rightarrow \pi^0 \nu \bar{\nu}$  with uncertainty comparable with the theoretical one. NA62 expects to measure  $\text{BR}(K^+ \rightarrow \pi^+ \nu \bar{\nu})$  with 10% precision, while KOTO aims to measure  $\text{BR}(K_L \rightarrow \pi^0 \nu \bar{\nu})$  to within a few percent [31]. Figure 1.3 shows how the  $(\bar{\rho}, \bar{\eta})$  plane will be constrained if each of these experiments measures the expected SM value with 10% precision [39].

Each theoretical new physics model affects the basic electroweak FCNC differently and it can be shown that measuring both  $\text{BR}(K^+ \rightarrow \pi^+ \nu \bar{\nu})$  and  $\text{BR}(K_L \rightarrow \pi^0 \nu \bar{\nu})$

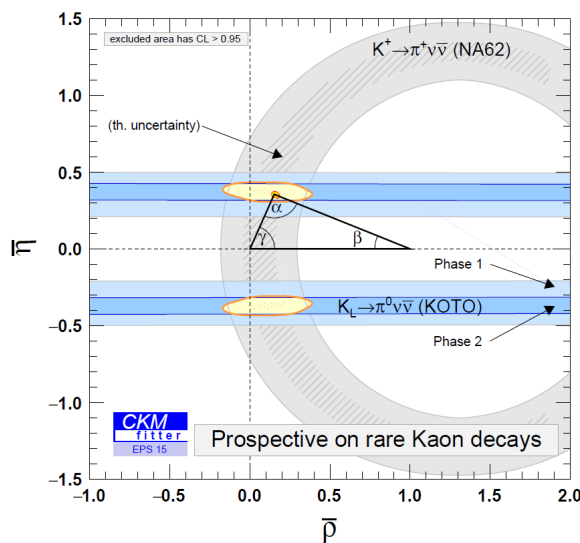


Figure 1.3: The expected constraints on the  $(\bar{\rho}, \bar{\eta})$  plane from the NA62 and KOTO experiments.

will allow to distinguish between these models. In these models it is assumed that new physics contributions can be absorbed into the function  $X$  of the equation 1.10 and 1.19, that in this case describes pure short distance contributions from not only the top quark, but also from new physics. In this general approach, contributions to  $X$  from left-handed and right-handed currents are present (while in the SM theory only the left-handed part is non-vanishing) and, according to the particular model chosen, different value of  $X$  (e.g. of the  $\text{BR}(K^+ \rightarrow \pi^+ \nu \bar{\nu})$  and  $\text{BR}(K_L \rightarrow \pi^0 \nu \bar{\nu})$ ) are possible. In general one can distinguish between three classes of models [32].

- Models with a CKM-like structure of flavour interactions; they include MFV and  $U(2)^3$  models [33]. In this case the only allowed values of both branching ratios are on the green branches in figure 1.4.
- Models with new flavour and CP-violating interactions in which either left-handed currents or right-handed currents fully dominate. In this case constraint implies the blue branch structure shown in figure 1.4, which is characteristic for the LHT model [34], or  $Z$  or  $Z'$  FCNC scenarios [35] [36].
- Finally models like Randall-Sundrum models with custodial protection (RSc)

[37] shows a lack of correlation between the two BR (see red region in 1.4)

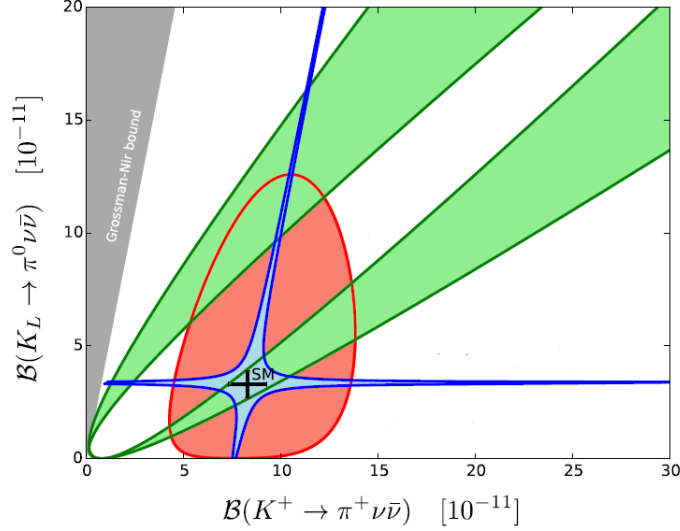


Figure 1.4: Illustrations of common correlations in the  $\text{BR}(K^+ \rightarrow \pi^+ \nu \bar{\nu})$  versus  $\text{BR}(K_L \rightarrow \pi^0 \nu \bar{\nu})$  plane for different new physics model [38].

## 1.4 $K^+ \rightarrow \pi^+ \nu \bar{\nu}$ experimental status

The first observation of the  $K^+ \rightarrow \pi^+ \nu \bar{\nu}$  decay and the best measurement currently available of its BR have been performed in two experiments at Brookhaven National Laboratory (BNL), E787 and its upgrade E949, which obtained first results at the end of 1990s. The adopted technique was to study  $K^+ \rightarrow \pi^+ \nu \bar{\nu}$  decay from kaons at rest. The signature for the decay is a pion of momentum  $P < 227\text{MeV}/c$  and no other particles. The observation of this signal requires suppression of all backgrounds with a reliable estimate of residual events. Figure 1.5 shows the two regions in the spectrum of the  $K^+ \rightarrow \pi^+ \nu \bar{\nu}$  decay together with the spectra of main kaon decay channels (not normalised to the BR which is indicated in parentheses). In E787 kaons are produced at momenta between  $710\text{MeV}/c$  and  $790\text{MeV}/c$  (in different runs) at a rate of  $7 \times 10^6$  per 1.6 s-spill of the Alternating Gradient Synchrotron (AGS), identified by Cherenkov, tracking and energy loss counters. 20% of the kaons reach a stopping target of plastic scintillating fibres. Measurements of the momentum ( $P$ ), range ( $R$ ) and kinetic energy ( $E$ ) of charged decay

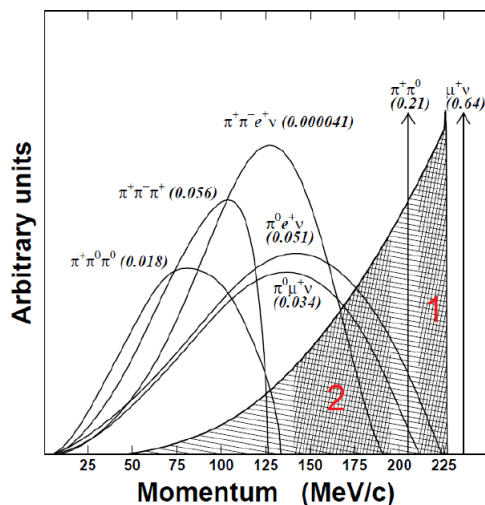


Figure 1.5: Momentum spectra of charged particles from  $K^+$  decays in the rest frame. The values in parentheses represent the BR of the decay modes. The hatched area represents the  $\pi^+$  spectrum from  $K^+ \rightarrow \pi^+ \nu \bar{\nu}$  decays. The densely hatched regions are the signal region 1 and region 2 (E949).

products were made using the target, a central drift chamber, and a cylindrical range stack made of layers of plastic scintillator counters and double-layer straw chambers. Pions were distinguished from muons by kinematics and by observing the pion decay sequence into muon and electron in the range stack. Photons were detected in a hermetic calorimeter, including detectors in the extreme forward and backward regions. A magnetic field was used for momentum measurements.

The search was performed requiring an identified kaon stopping in the target followed by a single charged particle track unaccompanied by other decay products. This particle must have been identified as a  $\pi^+$  with  $P$ ,  $R$  and  $E$ ; in addition to the kinematics, the measurement of the  $\pi \rightarrow \mu \rightarrow e$  decay sequence provided a further rejection factor against  $K_{\mu 2}$  events.  $K_{\pi 2}$  events were efficiently eliminated by exploiting the full calorimeter coverage, with an inefficiency of  $10^{-6}$  for photon energies above 1MeV. A scattered beam pion could result from a mis-identification as a  $K^+$ . Charge exchange background survived if  $K_L$  were produced at low enough energy to remain in the target for the required time and if the charged lepton decay product went unobserved.

E949 is an upgrade of the E787 experiment: the expected sensitivity increased by

a factor 5. The improvements regarded an upgrade of the photon veto calorimeter, replacement of one third of the Range Stack for the tracking, improvement of the trigger system and data analysis, which enabled to achieve a comparable acceptance even with twice the rate of E787. Both experiments used a blind data analysis strategy, and the background sources were identified and estimated with data-driven techniques. The major results of the E787 and E949 experiments are shown in figure 1.6:

- Three observed events in region 1, with a pion momentum (see figure 1.5) between 211MeV/c and 229MeV/c (this two line corresponds to the two body background decays  $K_{\pi 2}$  and  $K_{\mu 2}$ ).
- Four candidate events in region 2, with a pion momentum (see figure 1.5) between 140MeV/c and 195MeV/c.

The combined final measurements of E787+E949 is  $\text{BR}(K^+ \rightarrow \pi^+\nu\bar{\nu}) = 1.73_{-1.05}^{+1.15} \times 10^{-10}$ , based on the 7 observed candidate events [40]. This result is consistent with the SM theoretical prediction reported in section 1.2. However a measurement of the Branching Ratio with at least 10% accuracy is needed for a significant test of new physics. A recap of all the experimental measurements of the BR of the  $K^+ \rightarrow \pi^+\nu\bar{\nu}$  decay is presented in figure 1.7, where the results are shown along a time line indicating the year of publication.

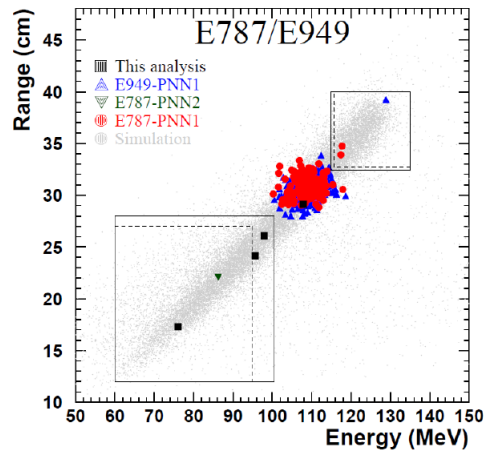


Figure 1.6: Range ( $R$ ) vs. Kinetic energy ( $E$ ) of all events passing analysis selection in E787 and E949 experiments. The squares represent the events observed by the E949 region II analysis. The circles and upward-pointing triangles represent the events observed by the E787 and E949 region I analyses, respectively. The downward-pointing triangle represent the events observed by the E787 region II analysis. The solid (dashed) lines represent the limits of the signal region I and region II for the E949 (E787) analyses. The points near  $E_\pi = 108\text{MeV}$  were  $K_{\pi 2}$  decays that survived the photon veto cuts and were predominantly from the region I analyses due to the higher sensitivity and the less stringent photon veto cuts. The light grey points are simulated  $K^+ \rightarrow \pi^+\nu\bar{\nu}$  events that passed the trigger conditions.

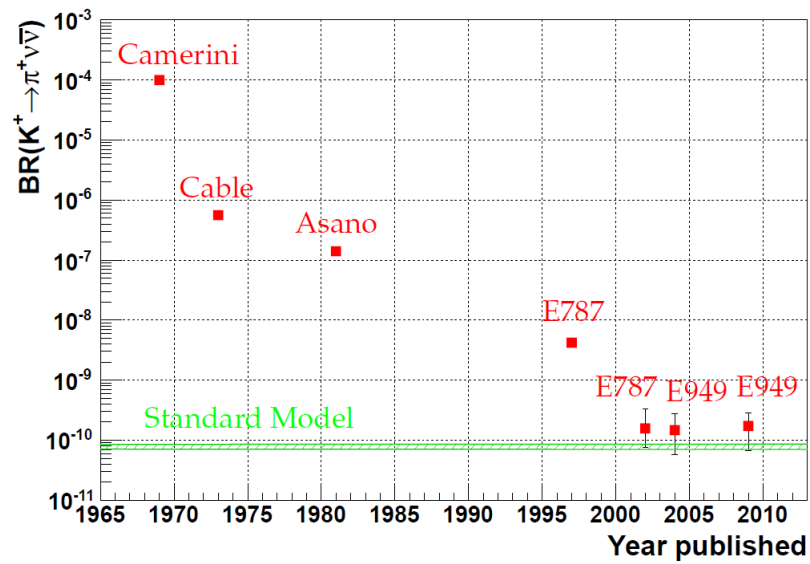


Figure 1.7: Experimental upper limits and measurements of the BR of the  $K^+ \rightarrow \pi^+ \nu \bar{\nu}$  shown along a time line indicating the year of publication. Squares with no errors are upper limits at 90% confidence level.

## Chapter 2

# The NA62 experiment

NA62 represents the current kaon physics program at CERN and offers a complementary approach, with respect to the LHC high energy frontier, to probe new physics at short distances, corresponding to energy scales up to  $\sim 100$  TeV. The NA62 experiment is housed in the CERN North Area High Intensity Facility and uses the SPS extraction line. A schematic view (not in scale) of the CERN accelerator complex is shown in figure 2.1.

The purpose of the experiment is to measure the BR of the kaon decay  $K^+ \rightarrow \pi^+ \nu \bar{\nu}$ , collecting  $\sim 100$  SM events of this process to get a 10% uncertainty. The SM prediction of this BR is very accurate:  $\text{BR}(K^+ \rightarrow \pi^+ \nu \bar{\nu}) = (9.11 \pm 0.72) \times 10^{-11}$  [3]. It is very interesting to measure this BR because this process represents a test for the SM and it is quite sensitive to the flavour structure of possible new degrees of freedom beyond the SM. The current measurement of this BR is  $1.73_{-1.05}^{+1.15} \times 10^{-10}$ , performed by E787/E949 collaboration at Brookhaven National Laboratory [40]. NA62 uses kaon decays in flight, differently from the kaon decay at rest approach which was at the basis of the E787/E949 experiments.

The experiment consists in generating a high intensity unseparated hadron beam and to detect both the decaying kaon and the final pion coming from a big fiducial volume ( $\sim 60$  m), and to exclude all the other channels. The hadron beam arises from a 400 GeV proton beam hitting on a beryllium target (CERN T10 line). The beam optics selects particles with an average momentum of 75 GeV/ $c$  producing a 750 MHz unseparated positive hadron beam with a 6% kaon component. The high momentum of the incoming beam improves the background rejection and sets

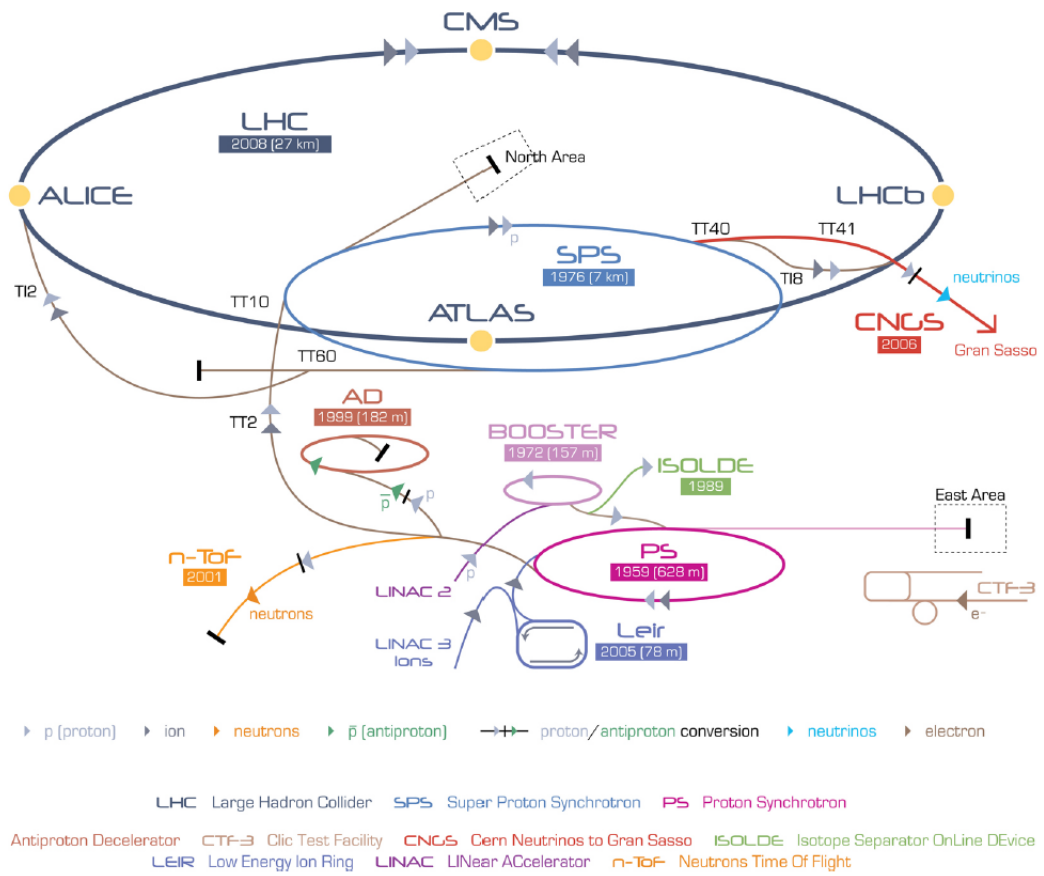


Figure 2.1: Schematic view of the CERN accelerator complex (not in scale). The NA62 experiment is located in the North Area SPS extraction line.

the longitudinal scale of the experiment (see figure 2.2). To achieve the required background suppression different principles have to be applied together:

- High intensity and good timing: a high intensity kaon beam is indispensable in order to reach sensitivity to a branching ratio of  $O(10^{-10})$ . The incoming secondary beam from the SPS provides a particle rate of 750 MHz: precise timing (level 100 - 150ps) of the  $K^+$  and the  $\pi^+$  allows precise matching of the particles in the decay and keep wrong associations below 1%.
- Tracking: the most discriminating variable to distinguish the signal from background is the squared missing mass:  $m_{miss}^2 = (p_K - p_\pi)^\alpha (p_K - p_\pi)_\alpha$ , where  $p_K^\alpha$  and  $p_\pi^\alpha$  denotes respectively the 4-momentum of the parent particle assumed to be a kaon and the one of the decay particle assumed to be a pion. In order to exploit this variable, track position and momenta (for the  $K^+$  and the  $\pi^+$ ) have to be measured with high accuracy.
- Hermetic vetoing for photons and muons: the kinematic rejection must be accompanied by direct vetoing for photons (in particular for the  $K^+ \rightarrow \pi^+\pi^0$  background) and muons (in particular for  $K_{\mu 2}$  background)
- Particle ID: several detectors complement the event information with direct evidence on the particle species.

In this chapter the experimental strategy and the detectors are described.

## 2.1 NA62 experimental strategy

The signature of the signal is one  $\pi^+$  track in the final state matched with one  $K^+$  track in the beam. In figure 2.3 the kinematics of the decay  $K^+ \rightarrow \pi^+\nu\bar{\nu}$  is sketched. Only the momentum of the incoming kaon  $P_K$  and of the daughter pion  $P_\pi$  and the angle between them  $\theta_{K\pi}$  can be measured. Calling  $m_K$  and  $m_\pi$  the mass of the two particles, and  $p_K^\alpha$  and  $p_\pi^\alpha$  their four-momentum, we can define the

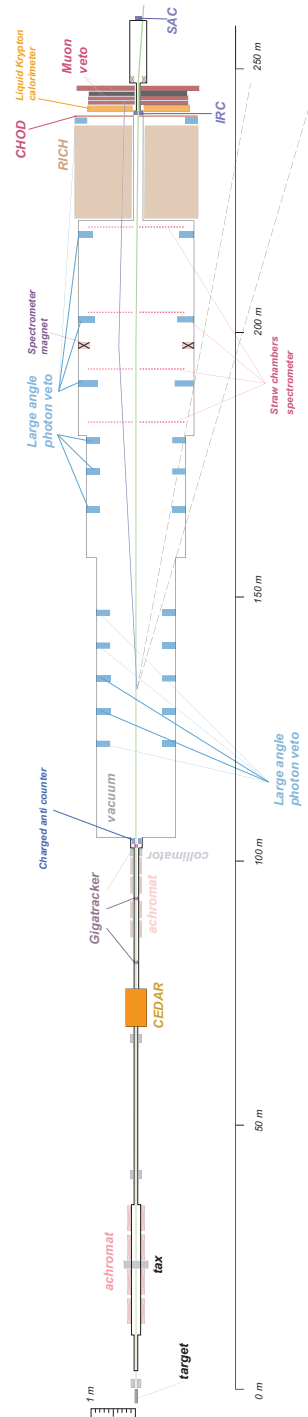
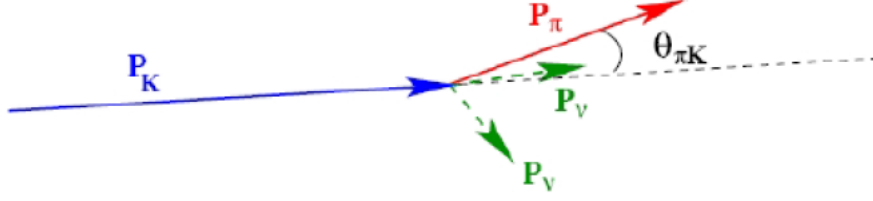


Figure 2.2: Layout of the NA62 experimental setup.


 Figure 2.3: Kinematics of the  $K^+ \rightarrow \pi^+ \nu \bar{\nu}$  decay.

kinematic variable  $m_{miss}^2$  as

$$\begin{aligned}
 m_{miss}^2 &= (p_K - p_\pi)^\alpha (p_K - p_\pi)_\alpha = \\
 &= m_K^2 + m_\pi^2 + 2 |\vec{P}_K| |\vec{P}_\pi| \theta_{K\pi} - 2 |\vec{P}_K| |\vec{P}_\pi| \sqrt{\left(1 + \frac{m_K^2}{|\vec{P}_K|^2}\right) \left(1 + \frac{m_\pi^2}{|\vec{P}_\pi|^2}\right)} \quad (2.1)
 \end{aligned}$$

Since particles are in a relativistic regime ( $mc^2 \ll pc$ ) and the angles are small (order of mrad), a good approximation for the missing mass is:

$$m_{miss}^2 = m_K^2 \left(1 + \frac{|\vec{P}_\pi|^2}{|\vec{P}_K|^2}\right) + m_\pi^2 \left(1 + \frac{|\vec{P}_K|^2}{|\vec{P}_\pi|^2}\right) - |\vec{P}_K| |\vec{P}_\pi| \theta_{K\pi}^2 \quad (2.2)$$

The absolute values of the kaon and pion momenta, together with their relative directions, are measured by a beam spectrometer (named GTK, see section 2.4.2) and a spectrometer placed downstream of the decay region (named STRAW, see section 2.5.1). The distribution of  $m_{miss}^2$  (with the hypothesis that the charged decay product is a pion) allows a separation of the signal from the main  $K^+$  decay modes by defining two signal regions where a limited background coming from the kinematically constrained decays is expected (figure 2.4):

- region I:  $0 < m_{miss}^2 < m_{\pi^0}^2 - (\Delta m)^2$
- region II:  $m_{\pi^0}^2 + (\Delta m)^2 < m_{miss}^2 < \min[m_{miss}^2(K^+ \rightarrow \pi^+ \pi^- \pi^+)] - (\Delta m)^2$

where  $m_{\pi^0}$  is the mass of neutral pion and  $(\Delta m)^2$  represents the resolution on the squared missing mass.

Nevertheless, the total background in region I and II is still several order of mag-

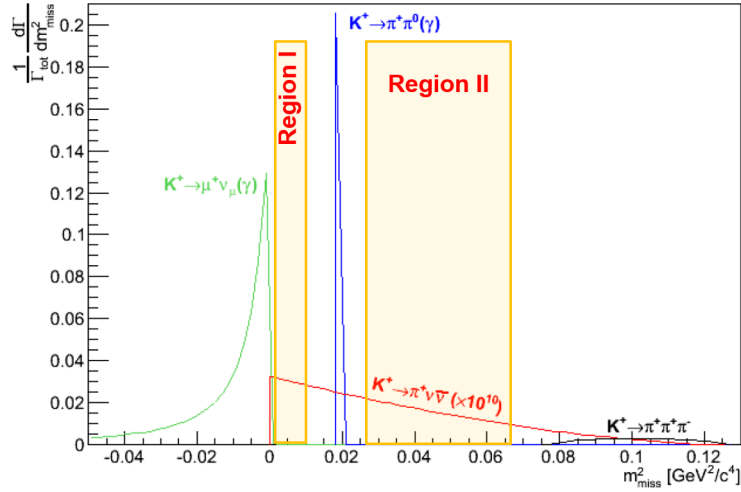


Figure 2.4: Distributions of the  $m_{miss}^2$  variable under the hypothesis that the detected charged particle in the final state is a pion, for the signal and the kaon kinematically constrained decays. The latter represents 92% of the total backgrounds for the  $K^+ \rightarrow \pi^+ \nu \bar{\nu}$  process. The  $K^+ \rightarrow \pi^+ \pi^0$  background forces the analysis region to be split into two regions.

nitude larger than the signal, as a consequence of the main decay modes leaking there via resolution effects and radiative tails, semi-leptonic decays and even rare decays whose kinematics cannot be constrained by the  $m_{miss}^2$  variable (see figure 2.5). So information from other detectors have to be collected in order to reduce background in the two signal regions.

A signal in the Cherenkov counter on the beam line (named KTAG, section 2.4.1) ensures the presence of a kaon in time with the tracks in beam spectrometer and in the downstream spectrometer. The KTAG signal also allows the suppression of most of the accidental tracks coming from the interactions of the pions in the beam with the material along the beam line. The presence of one track reconstructed in the downstream spectrometer matched in space and time with one track reconstructed in the beam spectrometer is the second requirement for a signal selection. A set of criteria for pion identification allows the suppression of the decay modes with muons and positrons, by means of a RICH (section 2.5.2) and hadronic calorimeters MUV1-2 (section 2.5.3). The same requirements are also effective for controlling the backgrounds with more than one charged track in the

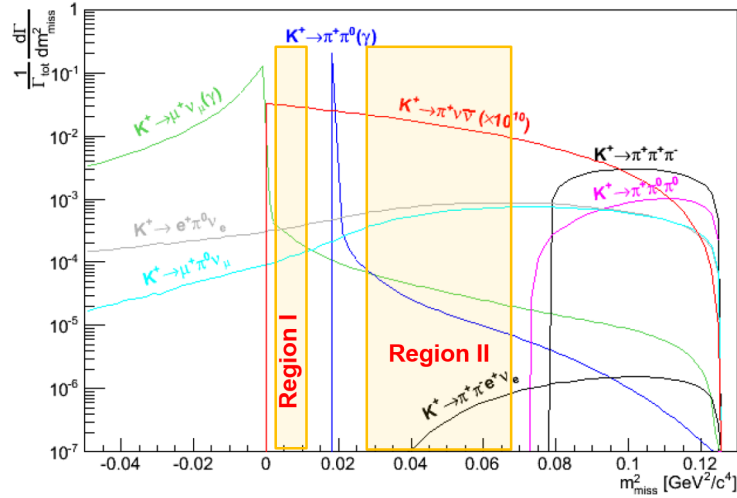


Figure 2.5: Distributions of the  $m_{miss}^2$  variable under the hypothesis that the detected charged particle in the final state is a pion, for the signal and the kaon not kinematically constrained decays. The two analysis regions are named I and II.

final state. A hermetic photon veto system (section 2.6.2) is also important to suppress decay modes with photons in the final state, by vetoing events compatible with the presence of photons. However, the interaction of the beam with the GTK is itself a possible source of background. In particular, kaon inelastic scattering events can mimic the signal if a produced pion falls into the RICH and STRAW acceptance, if it is badly reconstructed inside the fiducial volume, and if no other tracks are detected. The charged anti counter (CHANTI) is a detector placed in vacuum just after the GTK (27 mm) to help the rejection of this background, by covering hermetically the region between 49 mrad and 1.2 rad wrt the third (last) GTK station. Finally two global requirements are applied in the analysis:

- the kaon decay has to take place in the first 60m of the decay volume (fiducial volume)
- the measured momentum of the downstream  $\pi$  must be between 15 GeV/c and 35 GeV/c in order to achieve the desired background rejection (see section 2.2)

## 2.2 Main background rejection

Table 2.1 lists the dominant  $K^+$  decay modes, together with the techniques that will be used to reject them. The  $K^+ \rightarrow \pi^+\pi^0$  is primarily rejected by select-

Decay	BR	Rejection mode
$K^+ \rightarrow \mu^+\nu_\mu$	63%	$\mu$ -ID + kinematics
$K^+ \rightarrow \pi^+\pi^0$	21%	$\gamma$ -veto + kinematics
$K^+ \rightarrow \pi^+\pi^-\pi^+$	6%	multi-track + $\pi^-$ -ID + kinematics
$K^+ \rightarrow \pi^0e^+\nu_e$	5%	$e$ -ID + $\gamma$ -veto
$K^+ \rightarrow \pi^0\mu^+\nu_\mu$	3%	$\mu$ -ID + $\gamma$ -veto
$K^+ \rightarrow \pi^0\pi^0\pi^+$	2%	$\gamma$ -veto + kinematics

Table 2.1: Main kaon decays, their BR and corresponding rejection methods.

ing the two signal regions defined in section 2.1. The tracking system allows a  $10^{-3}\text{GeV}^2/c^4$  resolution on  $m_{miss}^2$ . The rejection factor from kinematics is about  $5 \times 10^3$ . The non Gaussian tails due to multiple scattering and pileup in the beam spectrometer are the main limiting factors to the kinematic rejection power. For what concerns the pileup, the precise timing between the upstream and downstream track is the key ingredient to reduce the mismatch probability below the percent level, which corresponds to about one half of the total kinematic rejection inefficiency. The photon rejection must guarantee a  $\pi^0$  suppression by 8 orders of magnitude. Nevertheless the  $\pi^0$  has at least an energy of 40 GeV, after requiring that the  $\pi^+$  momentum should not exceed 35 GeV/c. The system of electromagnetic calorimeters and photon vetoes of NA62 ensures a geometrical coverage for photons with polar angles up to 50 mrad and with an energy down to 100MeV. About 0.2% of the  $K^+ \rightarrow \pi^+\pi^0$  decays have one photon outside the detection region, but the other photon has always an energy of the order of 10 GeV or even more and travels in the forward direction.

Because of the pion track hypothesis, the  $m_{miss}^2$  spectrum of the  $K^+ \rightarrow \mu^+\nu_\mu$  is negative and momentum dependent, approaching zero at increasing pion momenta. As a consequence, the cuts on  $m_{miss}^2$  defining the signal regions allow a strong suppression of this background. Also, the cut at 35 GeV/c on the maximum track momentum enhances the kinematic rejection factor. The situation is similar to that of  $K^+ \rightarrow \pi^+\pi^0$ , with the difference that the  $K^+ \rightarrow \mu^+\nu_\mu$  background affects

mainly region I and the muon does not suffer from hadronic elastic scattering. The overall rejection factor is  $1.5 \times 10^4$  with the limiting factors coming from multiple scattering non Gaussian tails and pileup. The muon suppression comes from the pion identification which uses electromagnetic calorimetric and Cherenkov information. These inputs are combined with those from the hadronic calorimeter and muon veto subdetectors. The ultimate inefficiency of the muon-pion separation is  $10^{-5}$  and comes from the absorption of muons due to the energy loss via Bremsstrahlung.

The requirement of having only one track in the downstream spectrometer rejects about 99% of the  $K^+ \rightarrow \pi^+\pi^-\pi^+$ . The  $m_{miss}^2$  spectrum is crucial to strongly suppress the contribution from those  $K^+ \rightarrow \pi^+\pi^-\pi^+$  with one  $\pi^+$  and the  $\pi^-$  not reconstructed in the spectrometer. Also the cut at 15 GeV/c on the minimum track momentum is effective to this goal. The overall rejection factor from kinematics is  $1.5 \times 10^6$ . The residual background comes from events entering in region II, because of the tails of the reconstructed  $m_{miss}^2$  due to the non Gaussian multiple scattering. The largest part of the remaining events have one good  $\pi^+$  reconstructed and the other two charged pions pointing to the central beam hole which allows the passage of undecayed beam particles throughout the downstream detectors. Nevertheless, the strength of the magnetic field of the spectrometer magnet and the distance between this magnet and the detectors downstream ensure a full geometrical coverage downstream of the magnet for the detection of  $\pi^-$  up to 65 GeV/c. The rejection factor is of the order of  $10^6$ .

## 2.3 Beam line

The beam feeding the NA62 experiment is a secondary hadron beam produced from primary protons extracted from the SPS with a momentum of 400 GeV/c and impinging on a beryllium target located at the beginning of the NA62 experimental hall. The target is followed by a 950 mm long, water-cooled, copper collimator, offering a choice of bores of different apertures. The first active elements of the high-intensity beam are a triplet of radiation-hard, smallaperture, quadrupole magnets, which collect a large solid angle acceptance ( $\pm 2.7$  mrad horizontally and  $\pm 1.5$  mrad vertically) at 75 GeV/c central momentum. Shortly downstream follows a front-end achromat to select the beam momentum of 75 GeV/c ( $\pm 1\% \delta p/p$ ).

In between, the beam passes through a set of graduated holes in the blocks of TAX 1 and TAX 2 to make the momentum selection and to absorb unwanted particles. This is followed by set of magnets and collimators to tune the beam parallel with small intrinsic divergence.

The high energy protons are used in order to exploit the trend of the kaon production cross-section which increases with the proton energy; this helps also to reduce the non-kaon related activity in the detector reducing the number of protons needed.

The measured particle production data [41] established that the number of  $K^+$  ( $K^-$ ) decays in a given fiducial volume is maximum for  $p_K \sim 0.23 \times p_0$  ( $p_K \sim 0.15 \times p_0$ ), where  $p_K$  and  $p_0$  are the kaon and proton beam momenta respectively; however the highest  $K$  momentum achievable by the various stages of the beam optic is 75 GeV/c. Ultimately, we chose to use a positive rather a negative beam because the cross section is higher ( $K^+/K^- \sim 2.1$ ) for 400 GeV/c primary protons and the ratio  $\frac{K^+/\pi^+}{K^-/\pi^-} \sim 1.2$ . The choice of a central momentum of 75 GeV/c is driven by several factors, and is the result of a compromise between particle flux at production and fraction of kaons decaying within the 60 m long fiducial region. In addition, this value fits well with the characteristics of the detectors for particle identification: the useful range of momenta for a  $\pi^+$  decay product to be distinguished from a background  $\mu^+$  is between 15 GeV/c and 35 GeV/c, and this means that other particles associated with an accepted pion must carry an energy above 40 GeV, for which the veto system has an adequate efficiency. Finally, it is the maximum momentum for which the required stages of the beam optics can fit in the available length of about 102m from the production target to the beginning of the decay fiducial region. The principal disadvantage of performing the experiment at high momentum is that kaons cannot be efficiently separated from other charged hadrons (protons and pions). The consequence is that upstream detectors, placed along the beam line, are exposed to a particle flux much larger than the kaon component. The total rates of the secondary beam is 750 MHz while its components are: protons at 173 MHz (23%),  $K^+$  at 45 MHz (6%),  $\pi^+$  at 525 MHz (70%) and  $\mu^+$  at 5 MHz (0.7%). The beam is able to produce about  $4.5 \times 10^{12}$  kaon decays per year at nominal intensity [42] in the fiducial region, which is 60 m long and starts at 105 m from the beryllium target. Table 2.2 summarises the most relevant NA62 beam properties.

SPS proton rate on target		$1.0 \times 10^{12}$ Hz
Inst. K12 Beam Rate	proton	173 MHz (23%)
	$K^+$	45 MHz (6%)
	$\pi^+$	525 MHz (70%)
	$\mu^+$	5 MHz (0.7%)
	$e^+$	0.3 MHz (<0.1%)
	Total	750 MHz
Mean $K^+$ momentum		75 GeV/c
Momentum band r.m.s	$\Delta p/p$	1%
Beam size at the GTK r.m.s.	$x$	$\pm 26.4$ mm
	$y$	$\pm 12.0$ mm
Decay fiducial length		60 m
$K^+$ lifetime ( $\beta\gamma c\tau$ )		564 m
Decay Fraction		0.101
$K^+$ decays in fiducial length per year		$4.5 \times 10^{12}$

Table 2.2: Main beam parameters of the high intensity K12 beam.

## 2.4 Kaon identification and tracking system

This section describes the detectors placed along the beam line for kaon identification and tracking.

### 2.4.1 KTAG

The kaon component in the beam is about 6% out of the total 750 MHz rate. A critical aspect is therefore to positively identify the minority particles of interest, kaons, in a high rate environment. This is achieved by placing in the incoming beam a differential Cherenkov counter, the KTAG. This detector is an upgrade of the CEDAR built for the SPS secondary beams. The CEDAR was designed to work as a particle mass selector: for a given momentum the Cherenkov angle of the light emitted by a particle traversing a gas of a given pressure is a unique function of the particle mass and emitted light wavelength.

The CEDAR (see figure 2.6) consists of a pressure vessel filled with  $1.1 \text{ m}^3$  of  $\text{N}_2$  at 1.74 bar or  $\text{H}_2$  at 3 bar. At the end of the vessel, the Cherenkov light is re-

flected by a spherical mirror into a ring-shaped diaphragm of 100mm radius with adjustable aperture width, located at the beginning of the vessel. A chromatic corrector lens, designed to match the dispersion curve of the gas and positioned in between the mirror and the diaphragm, ensures that the light of all wavelengths arrives at the same radius on the diaphragm plane. The advantage of this design is that light from unwanted particles hits the diaphragm plane at a different radius, it therefore does not pass through the aperture and does not contribute to the rate. This only works if all rings are concentric, which requires all beam particles to be parallel to each other and consequently imposes constraints on the beam optics. The KTAG upgrade of NA62 acts in the Cherenkov light detection phase: to cope with the expected 45 MHz kaon rate, 384 photomultipliers (PMTs) divided in 8 light boxes called octants (48 PMTs per octant), and replacing the original 8 PMTs, are placed behind the 8 annular slits. As a consequence, an average rate of about 4 MHz is foreseen on a single PMT.

The performance of KTAG was evaluated during the 2015 data taking. The de-

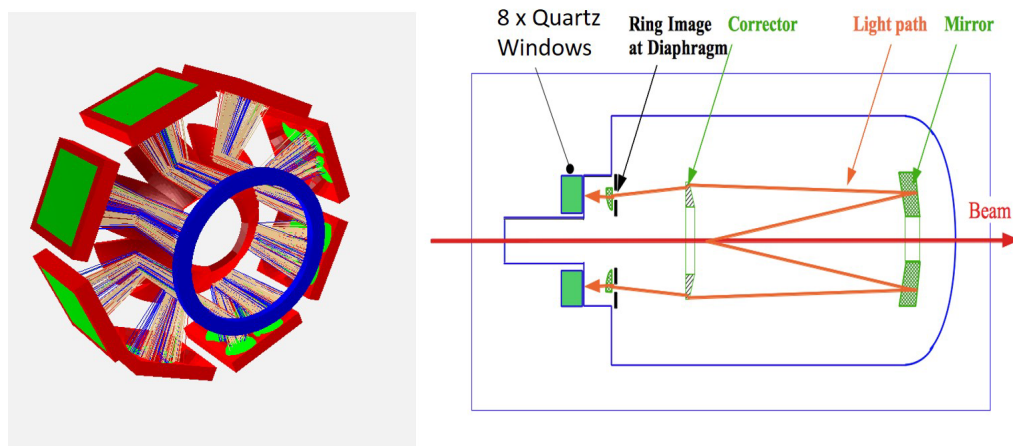


Figure 2.6: Left: CEDAR optics; Cherenkov light is reflected on the mirror at the rear CEDAR end; an adjustable diaphragm allows to select sharply the peak region of the cherenkov angle. Right: KTAG optics; the Cherenkov light exiting from the 8 quartz windows is deflected radially out; each sector is equipped with 32 PMTs.

tection efficiency of KTAG was measured using identified  $K^+$  decays to  $\pi^+\pi^0$  and found to exceed 95% when requiring Cherenkov light in coincidence from at least 4 octants. The pion misidentification rate was estimated to be of the order of  $10^{-4}$ .



common to the 3 GTK stations. The  $C_6F_{14}$  liquid is cooled by an externally controlled chiller and the circulation is forced with a pressure close to 3 bar. The temperature at the chiller output can be controlled over the range between  $-25^\circ\text{C}$  and  $0^\circ\text{C}$ . In case of vacuum failures or overheating adequate interlocks protect the system from damages.

## 2.5 Pion tracking, identification and timing system

In this section the spectrometer tracking system for the decay products is described, together with detectors needed to achieve the required timing and the essential pion identification to provide the additional background suppression factor.

### 2.5.1 STRAW

A downstream magnetic spectrometer (STRAW) is used to measure the momentum and direction of secondary charged particles originating from the decay region. The kinematic rejection of the backgrounds requires a  $\sigma(P_K)/P_K < 1\%$  and a resolution on  $\theta_{K\pi}$  less than  $60\mu\text{rad}$ . The STRAW, as shown in figure 2.8, is composed of a high aperture dipole magnet, providing a vertical B-field of 0.36 T, and four tracking chambers, working in vacuum in order to minimize the multiple scattering effects. Each chamber is equipped with 1792 straw tubes, a technology needed to

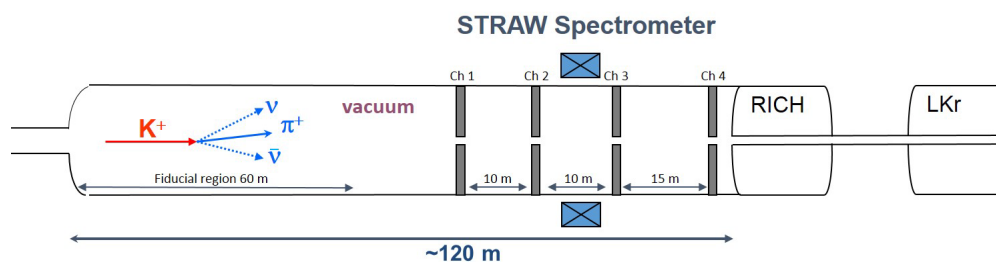


Figure 2.8: Schematic drawing of the NA62 spectrometer. Four Straw Chambers are installed inside the vacuum tank interleaved by a dipole magnet in the middle.

cover large areas and operate in vacuum. Each chamber has 4 views, as shown in figure 2.9, providing measurements of two couple of orthogonal coordinates ( $x,y$  and  $u,v$ ) rotated by  $45^\circ$ : this is necessary to eliminate the ambiguity in the track assignment in case of multiple hits. The tubes are manufactured from  $36\mu\text{m}$  thin PET (PolyEthylene Terephthalate) foils, coated (on the inside of the tube) with two thin metal layers ( $0.05\ \mu\text{m}$  of Cu and  $0.02\ \mu\text{m}$  of Au) to provide electrical conductance on the cathode. The anode wire (diameter  $30\ \mu\text{m}$ ) is gold-plated tungsten. In the central part of the chamber there is room for the beam pipe that allows the beam to pass through. There are 112 straws in each layer and the distance between the straws in one layer is  $17.6\ \text{mm}$ , thus at least two hits per view are always present.

Further experimental requirements for the STRAW are:

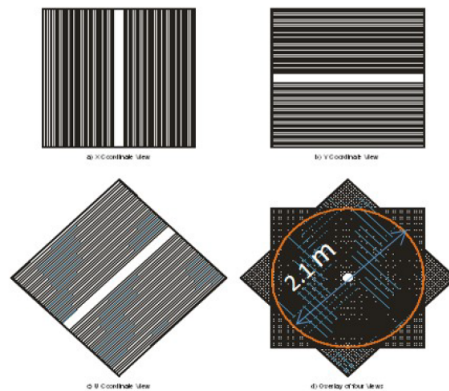


Figure 2.9: One Straw Chamber measures 4 coordinates (called views). Near the middle of each view a few straws are left out forming a hole for the beam passage.

- use of minimum amount of material ( $\leq 0.5\%X_0$  for each chamber) along the particle trajectory to minimize multiple Coulomb scattering;
- a spatial resolution  $\leq 130\mu\text{m}$  per coordinate and  $\leq 80\mu\text{m}$  on the final reconstructed point;
- operation with an average particle rate of  $40\ \text{kHz}$  and up to  $500\ \text{kHz}$  per straw;
- capability to veto events with multiple charged particles.

## 2.5.2 RICH

The Ring Imaging CHerenkov (RICH) is the main particle identification detector in NA62. Its principal purpose is a further rejection of the muon background component by means of identification and separation of  $\pi^+$  and  $\mu^+$  particles. At the lowest trigger level it will be one of the reference detectors, tagging the passage of a charged particle and partially vetoing multi-track events.

The particle identification exploits the formation of light cones due to the Cherenkov effect. The light cone is reflected by the mirrors and the photon detectors are placed on the mirror focal plane: here the cone image is a ring of radius  $r = f \tan \theta_c \sim f \theta_c$  ( $\theta_c$  is the Cherenkov angle) where  $f$  is the focal length of the mirror. (17 m) The radius depends only on the particle velocity and this means that for a given value of the momentum of a particle, the ring radius depends only on its mass. The NA62 RICH is required to provide a pion-muon separation in the momentum range between 15 GeV/c and 35 GeV/c with a rejection factor for muons of at least 100. The NA62 RICH is placed right after the fourth straw chamber. It is composed of a 17 m long cylindrical tank, with a diameter of 2.8 m, filled with Neon at atmospheric pressure, which corresponds to 5.6% of a radiation length. A beam pipe with three sections respectively of external diameter 20 cm, 22 cm and 24 cm allows the beam to pass through; it has an inclination of 2.4 mrad with respect to the axis of neutral particles not deviated by the magnetic field. A schematic view of the detector is shown in figure 2.10.

The Cherenkov light is reflected by a system of hexagonal spherical mirrors placed

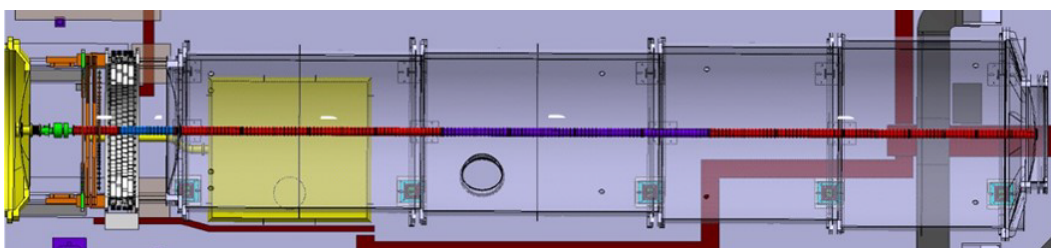


Figure 2.10: Top view of the RICH vessel with the aluminium beam pipe in its centre (beam direction from the right). The assembly is made of four cylindrical vessel of decreasing diameter and two light-weight aluminium windows at both extremities. The front conical cup (right side) accomodates at 3 and 9 o'clock the photo-detectors.

at the downstream end of the tank, and is conveyed towards the upstream part of

the detector. In order to avoid absorption of reflected light on the beam pipe the mirrors are divided into two spherical surfaces, one with the center of curvature to the left and one to the right of the beam pipe. Two flanges equipped each one with 960 photomultipliers are located in the upstream end of the detector. The centre of each flange is at a distance of 1.2 m from the beam pipe axis. The design of the mirror system and an image of one of the PMT flanges can be seen in figure 2.11. The active area of each PMT has a diameter of 8 mm, and a Winston cone is used to collect the light from a pixel of 18mm of diameter.

In 2009 a test beam was performed with a RICH prototype equipped with 414

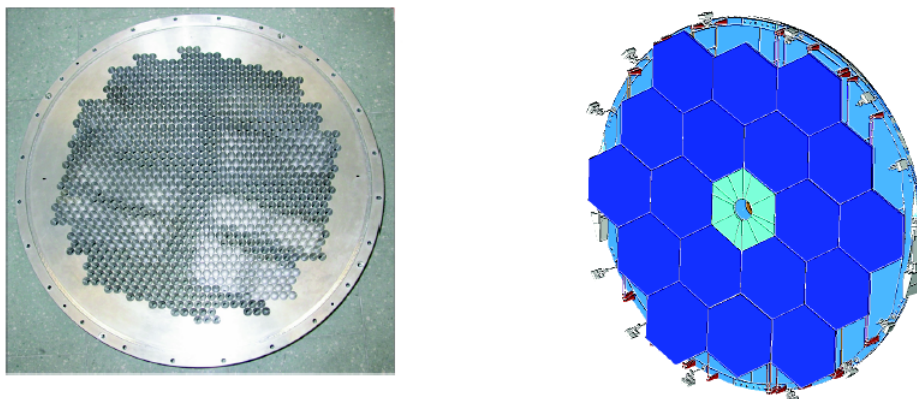


Figure 2.11: PMT flange (left) and design of the hexagonal mirror system of the RICH detector.

Hamamatsu R7400U-03 PMTs. A time resolution of 65 ps was measured and the  $\pi^+/\mu^+$  separation was scanned from 15 to 35 GeV/c. The  $\mu$  suppression factor was estimated to be  $10^{-2}$  integrated in the momentum range of interest [47].

### 2.5.3 MUV 1-2

A further reduction of the background coming from the  $K_{\mu 2}$  decay is achieved by means of the MUV1 and MUV2 detectors. They are hadronic calorimeters located after the LKr (see section electromagnetic calorimeter 2.6.2), used for the measurement of deposited energies and shower shapes of incident particles. Together with the MUV3 (see section 2.6.3), they constitute the muon veto system of the NA62 apparatus.

Events in which  $\mu^+$  from kaon decays deposit a major fraction of their energy in the

MUV1 and MUV2 calorimeters (these events are called catastrophic Bremsstrahlung) must be identified and vetoed, to ensure the S/B ratio required by the experiment. To reject these events, electromagnetic muon showers must be distinguished from hadronic pion showers by measurements of the shower shape. The two modules are shown in figure 2.12. Both modules are classic iron-scintillator sandwich calorime-

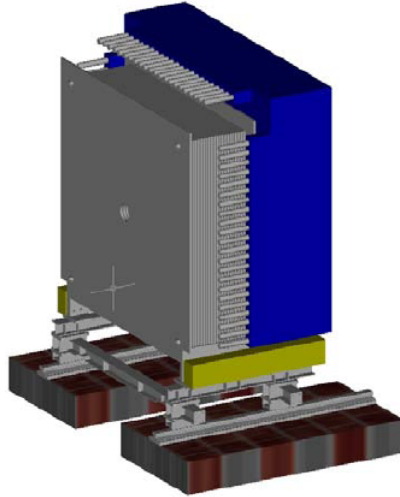


Figure 2.12: View of the MUV1 (grey) and MUV2 (blue) modules.

ters with 24 (MUV1) and 22 (MUV2) layers of scintillator strips, which are alternately oriented in the horizontal and vertical directions in both detectors. In the MUV1, the steel layers have a dimension of  $2700 \times 2600 \times 25 \text{ mm}^3$  with 12 mm spacing between plates, and a central hole of 212 mm diameter to allow the passage of beam particles. In the MUV2, the steel layers have a similar dimension of  $2600 \times 2600 \times 25 \text{ mm}^3$  with the same 12 mm spacing for the scintillator and the same 212 mm diameter central hole. For what concerns the scintillators, the MUV1 layers contain each one a total of 48 strips of about 6 cm width, for a total of  $48 \times 24 = 1152$  strips. The choice of the width is the result of a compromise between the need of high granularity and the number of PMTs and readout channels. The readout is made by two wavelength-shifting fibres per scintillator strip. The fibres of one longitudinal row of scintillators are bundled together to direct the light to one single PMT, therefore no longitudinal segmentation exists. The MUV2 scintillator planes consist of 44 strips of about 11 cm width, each one spanning only half of the transverse size of the detector, so that each plane is made

of two halfplanes. Consecutive strips with an identical x/y position and alignment are coupled to the same photomultiplier using Plexiglas light-guides.

### 2.5.4 CHOD and NEW CHOD

The Charged HODoscope (CHOD) is placed right after the RICH (section 2.5.2) tank and before the LKr calorimeter (section 2.6.2), with the main purpose of providing the timing of charged decay products. It is composed of two planes made of BC408 plastic scintillators, one with vertical and one with horizontal slabs. A layout of the CHOD detector is shown in figure 2.13. Each plane consists of 64

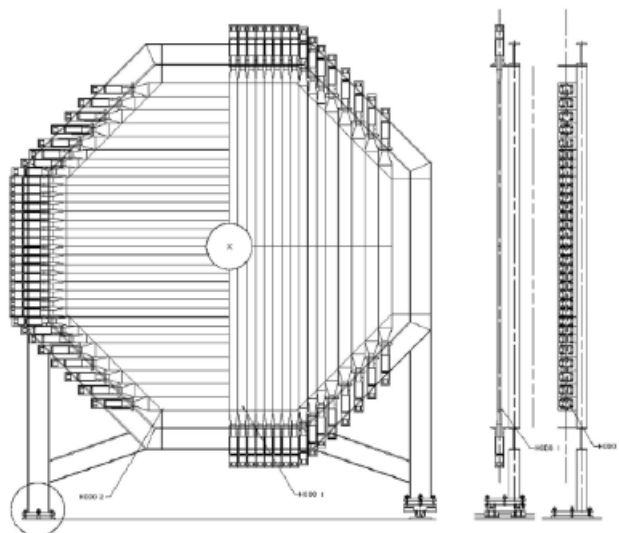


Figure 2.13: Sketch of the horizontal and vertical planes of the CHOD.

scintillator slabs of different length and width, divided in 4 quadrants containing 16 counters. The length varies from 60 cm to 121 cm and the width from 6.5 cm (in the region close to the beam pipe) to 9.9 cm. The thickness is the same for each slab and is equal to 2 cm, corresponding to 0.05 radiation lengths. The central hole, in which the beam pipe passes through, has a radius of 10.8 cm. The scintillation light produced at the passage of a charged particle is collected at the edge of a counter from a Plexiglas fishtail shaped light guide connected to a photomultiplier. The particle is identified through a time matching between hits in slabs of corresponding quadrants of the two planes. CHOD has a resolution better than 200 ps [45]. In

order to achieve this resolution, an impact point correction must be applied to avoid the effect due to the propagation time of the light inside the scintillator slabs towards the PMT. The timing capability of the CHOD is useful to complement the RICH detector in the lowest level trigger selecting charged tracks. The distance between the two planes is  $\sim 30$  cm. The different timing related to this distance will be used to tag fake coincidences due to the back-splash coming from the calorimeter surface, i.e. particles of the electromagnetic shower going back to the hodoscope.

Another goal of CHOD is to detect possible photo-nuclear reactions in the RICH mirror plane. The RICH mirror system amounts to about 20% of radiation length and photons from  $\pi^0$  decays can undergo photonuclear interactions producing low energy hadrons. This effect can weaken the photon veto function of the LKr. In order to re-establish the veto sensitivity to the required level a detector for low momentum charged track after the RICH is needed.

A new charged hodoscope is being developed and will be used in the second phase of the experiment. The main reason for replacing the old detector is the high hit rate at which the meter long slabs are exposed. The intrinsic dead time and the light transit time inside the scintillator are not compatible with the expected overall rate on the detector above 10 MHz. The transverse size will be reduced to 107 cm of inner radius. The detector will be made of a single plane of scintillator tiles of 30 mm thickness, 107 mm height and 265 mm width. The light will be collected by wavelength-shifting fibres linked to silicon photomultipliers (SiPM). A total number of 152 tiles and 304 SiPM are foreseen. With this design the expected maximum rate over a single tile close to the beam pipe is of the order of 500 kHz.

## 2.6 Veto system

This last section covers the detectors mainly used as vetoes in order to reject background events coming from kaon decays and kaon interactions before the decay region.

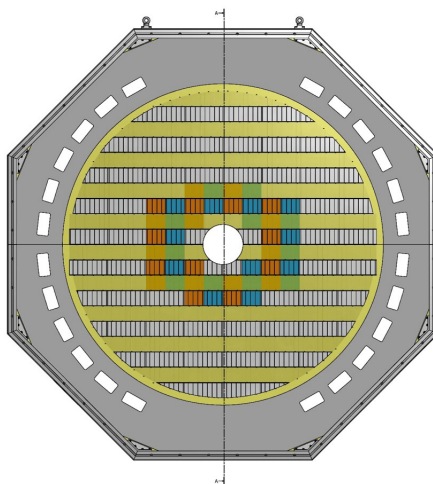


Figure 2.14: The new CHOD detector layout. It is mounted on the front face of LAV12.

### 2.6.1 CHANTI

The CHarged ANTI counter (CHANTI) aims to detect and reject inelastic interactions between the beam and the last GTK station: these are the most harmful because can mimic the signal signature if a secondary pion is emitted in the STRAW acceptance and, for effect of STRAW resolution tails, is badly reconstructed as coming from the decay region. It has been proposed, designed and constructed by the Naples group of NA62 and is the main subject of this work. See chapter 3, 4 and 5 for more details.

### 2.6.2 Photon Veto detectors

This section covers the detectors mainly used to reject kaon decays containing photons coming from  $\pi^0$  decay. In particular the kaon decay channel  $K^+ \rightarrow \pi^+\pi^0$  can contaminate the signal region if the two photons from the  $\pi^0 \rightarrow \gamma\gamma$  decay are not detected. The cut on the charged pion momentum between 15 GeV/ $c$  and 35 GeV/ $c$  provides a kinematic rejection factor on  $K^+ \rightarrow \pi^+\pi^0$  events of order of  $10^{-4}$ . To ensure the signal over background ratio ( $S/B \sim 10/1$ ) required by the NA62 measurement strategy and to control the  $K^+ \rightarrow \pi^+\pi^0$  background, it is essential to keep the average inefficiency on the rejection of the  $\pi^0$  down to a level of  $10^{-8}$ . To this end, an hermetic photon veto system has been proposed to detect photons produced in the fiducial decay region. The geometry of the experiment

suggests a partition of the veto system into three different angular regions, each one instrumented with three different detector technologies that will be presented in the following paragraphs.

## LAV

The Large Angle Veto (LAV) system provides full coverage for decay photons with polar angles from 8.5 mrad to 50 mrad. Together with the electromagnetic calorimeter it will participate in the lowest level trigger chain to further suppress  $K_{\pi 2}$  events with one (or both) photons from  $\pi^0$  at large angle.

The NA62 LAV detectors make creative reuse of lead glass blocks recycled from the OPAL electromagnetic barrel calorimeter [43]. Other solutions considered included a lead/scintillating tile design and a lead/scintillating-fibre design, based on the electromagnetic calorimeter for the KLOE experiment. Prototypes based on each of the three technologies were built, and tested with the electron beam at the Frascati Beam-Test Facility (BTF). These tests demonstrated that all three technologies are suitable for use in NA62. In particular, the inefficiency for the detection of single, tagged electrons with the OPAL lead glass modules was measured to be  $1.2^{+0.9}_{-0.8} \times 10^{-4}$  at 203 MeV and  $1.1^{+1.9}_{-0.7} \times 10^{-5}$  at 483 MeV. Basing the construction of the LAV system on the OPAL lead glass modules provides significant economic advantages.

The modules from the central part of the OPAL electromagnetic barrel calorimeter consist of blocks of lead glass. This material is about 75% lead oxide by weight and has a density  $\rho = 5.5 \text{ g cm}^{-3}$  and a radiation length  $X_0=1.50 \text{ cm}$ ; its index of refraction is  $n \approx 1.85$  at  $\lambda=550\text{nm}$  and  $n \approx 1.91$  at  $\lambda=400 \text{ nm}$ .

The front and rear faces of the blocks measure about  $10 \times 10 \text{ cm}^2$  and  $11 \times 11 \text{ cm}^2$ , respectively; the blocks are 37 cm in length. Each block is read out at the back side by a photomultiplier, which is optically coupled via a 4 cm long cylindrical light guide of the same diameter as the PMT (see figure 2.15).

A LAV station is made by arranging these blocks around the inside of a segment of vacuum tank, with the blocks aligned radially to form an inward-facing ring. Multiple rings are used in each station in order to provide the desired depth for incident particles. The blocks in successive rings are staggered in azimuth; the rings are spaced longitudinally by about 1 cm. Figure 2.15 shows the completed

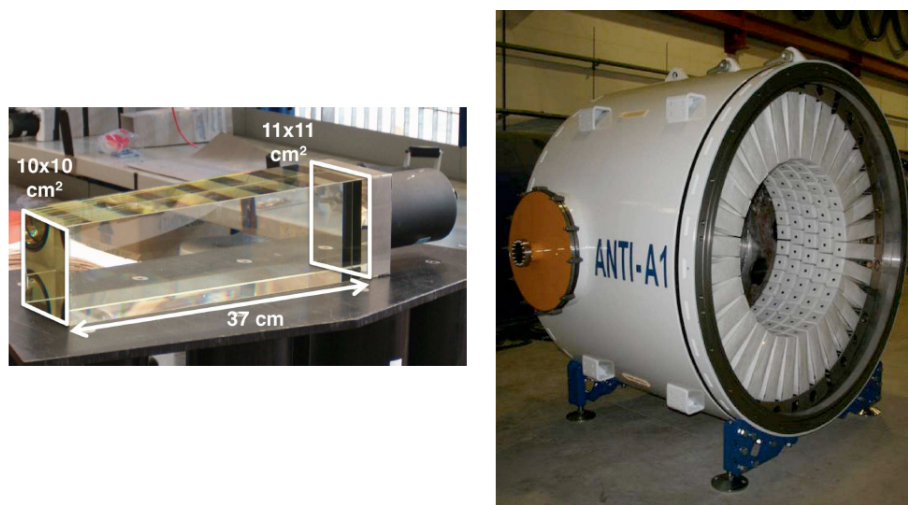


Figure 2.15: A module from the OPAL calorimeter (left). The 1st LAV station with  $32 \times 5$  wrapped OPAL lead glass calorimeter elements (right).

first station of the LAV system. The LAV system consists of a total of 12 stations, the diameter of which increases with distance from the target. As a result of the staggering scheme, particles incident on any station are intercepted by blocks in at least three rings, for a total minimum effective depth of 21 radiation lengths. The vast majority of incident particles are intercepted by four or more blocks ( $27 X_0$ ). The stations with five layers (A1-A8) are 1.55 m in length, while those with four layers (A9-12) are 1.43 m in length.

Results from a test beam performed at CERN in 2010 on LAV stations showed a single block time and energy resolutions of [44]:

$$\sigma_t = \frac{220ps}{\sqrt{E(\text{GeV})}} \oplus 140ps \quad \frac{\sigma(E)}{E} = \frac{9.2\%}{\sqrt{E(\text{GeV})}} \oplus \frac{5\%}{E(\text{GeV})} \oplus 2.5\% \quad (2.3)$$

### LKr

The Liquid Krypton calorimeter (LKr) has to detect  $\gamma$  coming from the decay volume with angles from 1 mrad to 8.5 mrad wrt the beam axis. It is also part of the lowest level trigger. The choice of a liquefied noble gas is due to the good resolution and linearity response in energy, the absence of ageing problems and the relative short radiation length which allows a compact design without the need of heavy passive parts, typical of sampling calorimeters. The homogeneity ensures a

good energy resolution, the granularity improves the spatial resolution and allows to separate showers close to each other. Radioactivity of the Krypton is negligible with respect to electronic noise and has therefore no effect on the resolution, but, due to the low boiling temperature of Krypton at 120 K, the whole detector has to be kept inside a cryostat: only temperature variations of few per mille are allowed, since the drift velocity of the electrons depends strongly on the temperature. Working at cryogenic temperature greatly increases the stability of the detector response and accuracy of its calibration.

The LKr is octagonal, containing a circle of 128 cm radius, 127 cm thick, corresponding to about 27 radiation lengths, and has a hole at the centre of 9 cm radius for the beam pipe. The total active volume of about 7 m<sup>3</sup> liquid Krypton is divided into 13248 cells (towers) by 18 mm wide, 40 μm thick copper-beryllium ribbons at a distance of 1 cm from each other and with no longitudinal segmentation. The ribbons are used as electrodes to collect the ionisation signal. A cell consists of a central anode, to which is applied a voltage of 3 kV, and two cathodes, one at each side, so that each cathode is in common between two cells. The separation between two cell layers is 2 mm. The cells define a projective geometry of the calorimeter pointing at about 90 m in front of it, inside the decay region. This particular geometry was chosen in order to achieve the best possible accuracy in the measurement of the angle between the flight path of photons and the beam direction. To avoid response variations depending on the lateral distance between the shower core and the anode, the cells are not straight along the flight path of the original particles but follow a zig-zag shape (see figure 2.16).

The excellent energy, space and time resolutions of the LKR calorimeter have been demonstrated by the NA48 collaboration [45]:

$$\begin{aligned}
 \sigma_t &= \frac{2.5\text{ns}}{\sqrt{E(\text{GeV})}} \\
 \frac{\sigma(E)}{E} &= \frac{3.2\%}{\sqrt{E(\text{GeV})}} \oplus \frac{9\%}{E(\text{GeV})} \oplus 0.42\% \\
 \sigma_{X,Y} &= \left( \frac{0.42}{\sqrt{E(\text{GeV})}} \oplus 0.06 \right) \text{cm}
 \end{aligned} \tag{2.4}$$

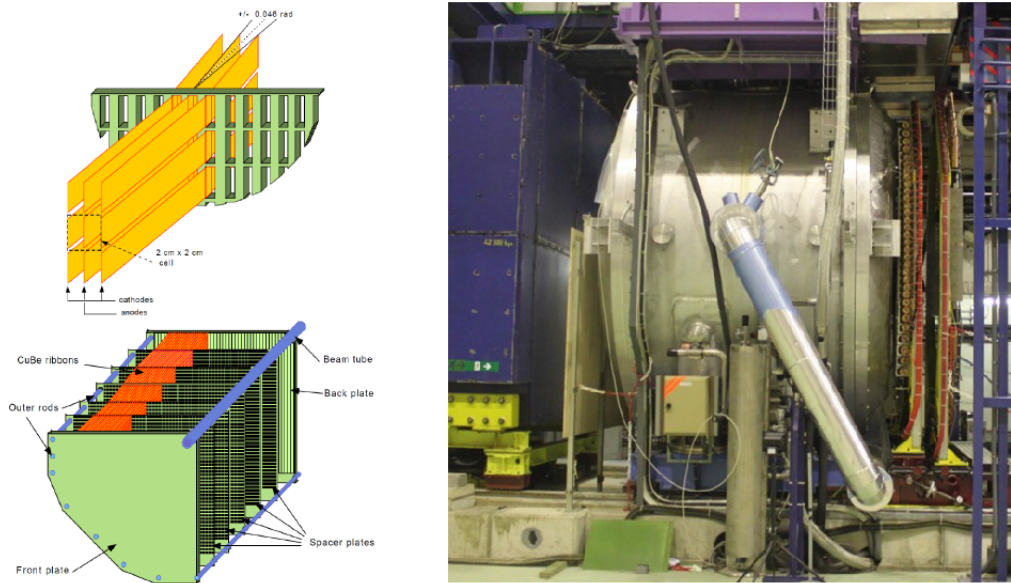


Figure 2.16: The LKr electrode structure and a detail of the LKr cell structure showing the accordion geometry structure of the ribbons (left). A picture of the LKr (right).

## IRC and SAC

The Inner Radius Calorimeter (IRC) and the Small Angle Calorimeter (SAC) are parts of the  $\gamma$  veto system for the decay products of the secondary  $\pi^0$ . The SAC has to detect  $\gamma$  coming from the decay volume with angles from 0 mrad to 1 mrad wrt the beam axis, while the IRC will cover a dead region at radii between 7 and 14 cm in front of the LKr. The IRC is placed in the front of the LKr, close to the beam pipe, while the SAC at end of the experimental setup, so the only geometric requirement is not being hit by the detected undecayed beam. These two small detectors have a single-photon detection efficiency better than  $10^{-5}$  for photon energies higher than 5 GeV.

Both the detectors use Shashlik technology, shown in figure 2.17 which is based on alternate layers of lead and plastic scintillator read by wavelength shifting fibers [46]. The fiber are read in bundle by classic photomultiplier tubes, as shown in figure 2.17.

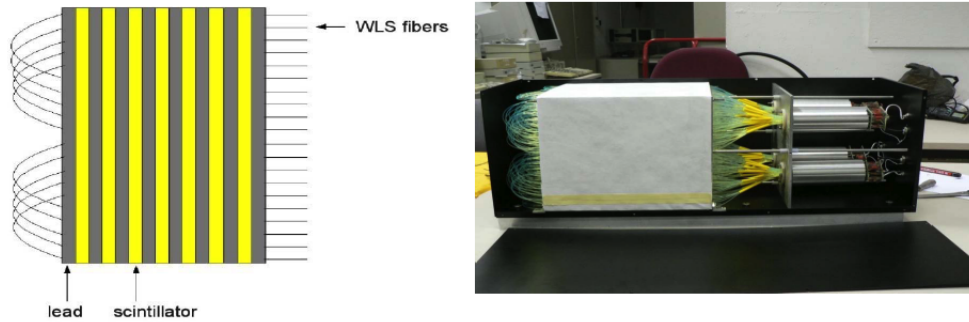


Figure 2.17: Sashlik technology with lead and scintillator plates (left). The SAC prototype (right).

### 2.6.3 MUV3

The third station of the muon veto system is located after the first two stations and is an additional muon filter, an iron wall of 80 cm depth, in order to detect non-showering muons; it also acts as muon veto detector at the lowest trigger level to suppress the high rate of  $K_{\mu 2}$  decays. The detector consists of a  $12 \times 12$  array of 5 cm thick scintillator tiles, with a transverse area of  $22 \times 22 \text{cm}^2$ . The light produced by traversing charged particles is collected by photomultipliers positioned about 20 cm downstream. Due to this geometry the maximum time jitter between photons from particles hitting different parts of the scintillator tiles is less than 250 ps, thus preserving the required time resolution of this detector. The time resolution may be spoiled by Cherenkov photons that are produced by particles traversing the PMT windows. These Cherenkov photons arrive earlier than photons produced in the scintillators, whose typical decay time is about 2 ns. To overcome this problem, each scintillator tile is read out by two PMTs. The output time of the coincidence of the two PMT signals corresponds to the time defined by the PMT which is unaffected by the Cherenkov photons. Figure 2.18 shows the layout of the MUV3 module and a detail of a single tile counter from a side view. As can be seen from the left, in the central region near the beam pipe, 8 smaller tiles around the hole replace 4 standard tiles, in order to better cope with the expected high rate of that region.

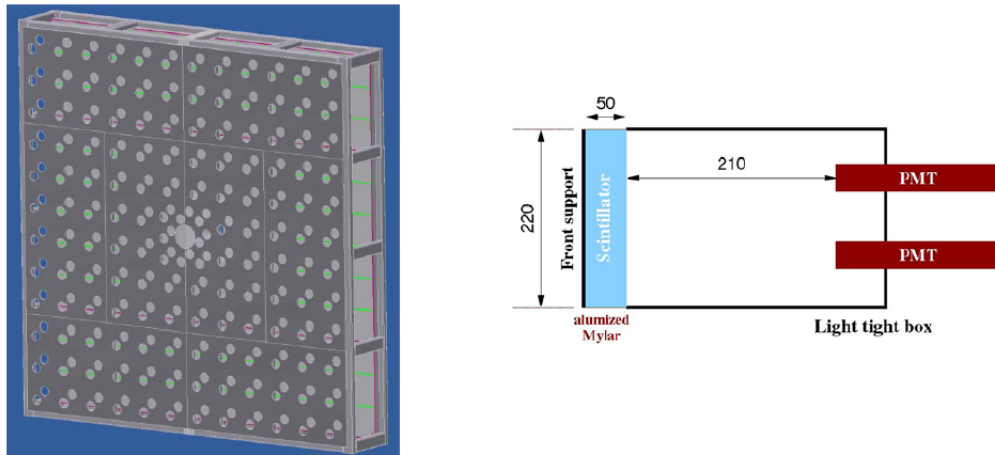


Figure 2.18: Layout of the MUV3 module (left). Detail of a single tile counter from a side view (right), with particles coming from left; the dimensions are expressed in mm.

## 2.7 Trigger and data acquisition

Rare decay experiments need intense flux so the performance and the dead time of the Trigger and Data Acquisition system (TDAQ) is a crucial factor. The NA62 solution [48] uses a common clock, with a frequency of  $\sim 40$  MHz, optically distributed to all systems by means of a Timing, Trigger and Control (TTC) electronic module designed for LHC experiments [49].

The data acquisition and the elaboration of the trigger primitives relies for most of the detector on a Time to Digital Converter (TDC) based system, the TEL62. The whole system, sketched in figure 2.19, is designed to work with time data, indeed the first stage of acquisition is made of fast (TDC) that accept signals in the LVDS standard, so all the detectors are supposed to provide this kind of signals. The TDC are arranged in boards containing 128 channels, and each group of 4 TDC board are connected to one TEL62 powered by 5 Altera FPGA. We chose a technology based upon FPGA so that each detector, with small firmware changes, can make some online data elaboration in order to modify the data before sending it to the farm (ex. calibration) or to produce some online data (ex. data for low level trigger). However the main task of four of the FPGA on the TEL62 (PP FPGA) is to manage the communication with the TDC boards (one PP for each TDC board) and to store them temporary in a 1 Gb of external RAM (for each

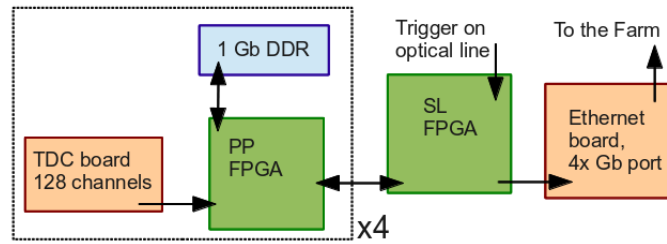


Figure 2.19: Schematic view of the TEL62 and TDC board.

PP). The fifth FPGA (SL FPGA) has to wait and decodes trigger signals from an optical line and propagates the trigger to the PP, then it has to search in the RAM the corresponding data and sends it back to the SL. The final task of the SL is to pack this data and to send them to the PC farm through four gigabit Ethernet boards. On the TEL62 is also present a credit card PC (CCPC), a fully featured PC running Linux, that is able to flash the FPGA firmware and to communicate with them by an ECS bus.

NA62 operates a 3-level trigger, with a hardware L0 trigger and software L1 and L2 triggers (see figure 2.20). The L0 trigger is designed to reduce the event rate

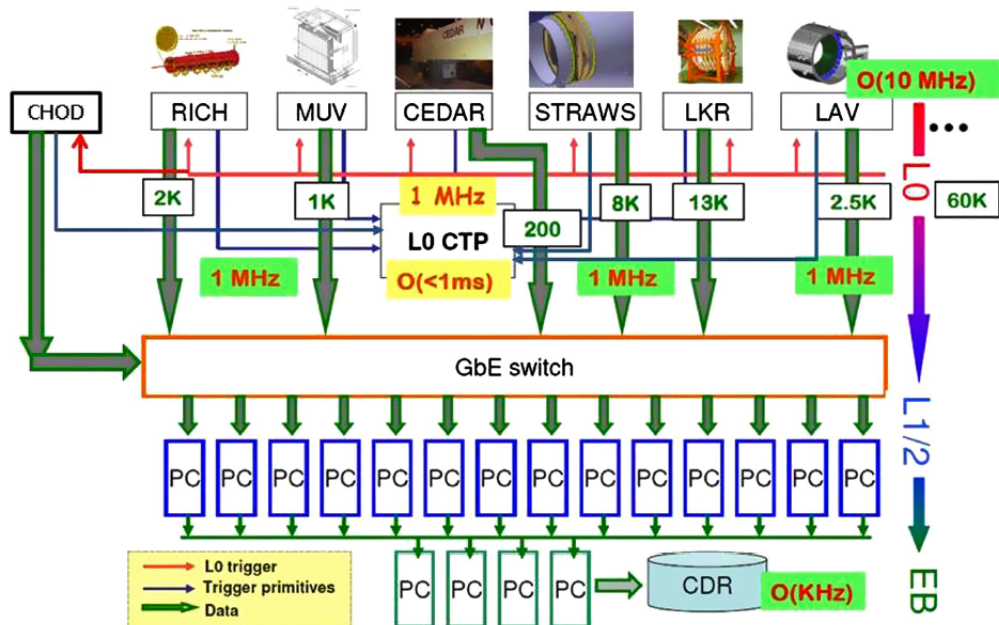


Figure 2.20: The trigger system system for NA62.

from  $O(10\text{MHz})$  to  $O(1\text{MHz})$ , based on trigger primitives, encoding a particular set of conditions that have been matched, from a subset of the sub-detectors. The maximum trigger latency at L0 is 1 ms, determined by the size of the buffers where sub-detector data is stored before the trigger decision is available. The L0 trigger processor is implemented on FPGAs, which have firmware implementations of the trigger algorithms. A PC based alternative for the L0TP is also under consideration [50].

In response to a L0 trigger signal, data from sub-detectors are sent to the read-out PC farm, where the L1 and L2 trigger decisions are made. The L1 trigger makes decisions based on conditions met by individual sub-detectors, such as the number of tracks seen in the STRAW detector. If the L1 trigger conditions are met, then the event is reconstructed at L2, combining information from all sub-detectors, to produce the final trigger decision. Events which satisfy the L2 trigger are written to tape.

## Chapter 3

# The detector CHANTI: design and construction

A particularly insidious source of background for the measurement of  $\text{BR}(\text{K}^+ \rightarrow \pi^+ \nu \bar{\nu})$  in the NA62 experiment is given by events produced by the inelastic interactions of the beam with the three measurement stations - in particular the third - of the beam spectrometer (GTK). The spectrometer, which consists of thin silicon pixels detectors, is installed in vacuum immediately upstream of the decay vacuum tube in which is located the fiducial region. A positive pion can mimic a signal event if it produced by the beam impacting GTK and detected by the apparatus of NA62 so that its origin is erroneously reconstructed in the fiducial region. To reduce this type of background to an acceptable level, a detector of veto charged particles was designed and built (CHarged ANTI-Counter, CHANTI). It is made of scintillation counters and is placed in vacuum immediately after GTK3 without interfering with the beam. CHANTI exploits the fact that the events to be rejected are normally inelastic events characterized by a high multiplicity of particles. To ensure a high efficiency of rejection it has just to be able to intercept charged particles produced at angles, with respect to the beam direction, ranging from 49 mrad up to 1.34 rad; the region up to 49 mrad is covered by the photon veto system. A study performed in [62] showed that geometrical inefficiency of the detector is  $\text{O}(0.1\%)$ .

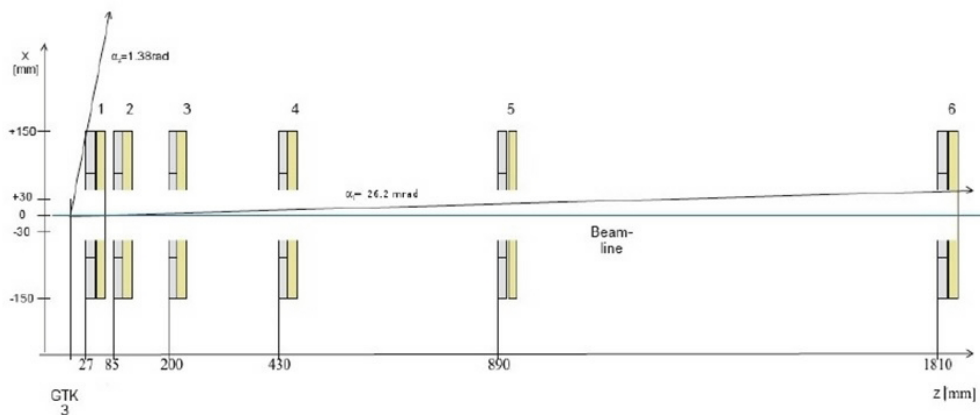


Figure 3.1: CHANTI stations layout with respect to GTK3 position.

### 3.1 Detector requirements

First of all CHANTI must be able to detect the inelastic interactions of the beam with very high efficiency. Considering that it will be impacted not only by secondary products of such interactions but also by the beam halo, CHANTI has to be able to sustain a high hit rate of charged particles, with a maximum rate per unit surface of the order of tens of kHz/cm<sup>2</sup> in the hottest region, and must have a radiation hardness up to a few Gy/year. A time resolution of  $\sim 1$  ns is also required in order to have a "random veto" not exceeding few percent. Finally, since it will be positioned in vacuum, the detector must have a small out-gassing rate and must consume a relatively low power. In principle a specific tracking capability is not required, however it is welcome in order to distinguish interactions due to the halo from those due to the beam, both to monitor the halo itself in the vicinity of the beam and to improve the time resolution without necessarily increasing the granularity.

CHANTI is made of six square counter hodoscopes (stations) of 30 cm side arranged in vacuum along the beam direction at distances of 27, 85, 200, 430, 890 and 1810 mm from GTK3 (see figure 3.1). In order not to hinder the beam, the stations have a central hole of  $65 \times 95$  mm<sup>2</sup> rectangular shape, with the longer dimension in the horizontal direction (x-axis) and the shorter in the vertical direction (y-axis). The geometry of the system is such that the CHANTI can intercept

secondary particles, generated by beam interactions at the center of GTK3, which propagate in an angular region from 26.2 mrad to 1.38 rad with respect to the beam axis and has full acceptance for those running between 49 mrad and 1.34 rad.

## 3.2 Basic elements of the detector

Each CHANTI station is made of scintillating bars in the shape of prisms with triangular base. Inside each bar there is a wavelength shifting fiber (WLS) collecting the scintillation light, and mirrored from one side. On the other side a Silicon-PhotoMultiplier (SiPM) readout is coupled to the fiber by means of a dedicated mechanical housing and its signals are readout through a dedicated coaxial cable connector. In this section all the basic elements of the detector are described.

### 3.2.1 Scintillators

The plastic scintillator bars are made of extruded polystyrene (Dow Styron 663 W) doped with 1% PPO and 0.03% POPOP (by weight). It is an inexpensive scintillator with emission in the blue, with a good yield of light, a rather fast response ( $\tau \sim$  few ns) and a good radiation hardness (5% degradation after a dose of  $10^4$  Gy gamma irradiation). The bars, produced by FNAL-NICADD [51] (the same bars are used in the MINERVA and D0 collaboration [52][53]), have a cross section in the shape of an isosceles triangle with base 33 mm and height 17 mm (figure 3.2) and carry a co-extruded  $\text{TiO}_2$  coating 0.25 mm thick. The

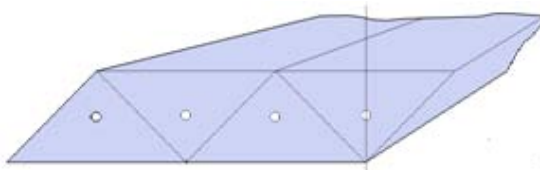


Figure 3.2: Bars arrangement.

bars, arranged next to each other in the way indicated in figure 3.2 allow to realize a plane counter 17 mm thick, essentially with no fractures for tracks that pass through it. Furthermore a track passes always in two bars emitting light

proportionally to the length traveled in each bar. Weighting the bars position with appropriate coefficients we can estimate the track hit position with a precision higher than the granularity of the detector. In fact, despite the center of the bars being 17 mm distant, we can reach a space resolution better than 3 mm (see chapter 5).

In figure 3.3 the transmittance and fluorescent spectra of the scintillator are shown [54]: there is a cut-off in the absorption at  $\sim 400$ nm and an emission peak at 420 nm (blue light). Each bar has longitudinally a central hole with a diameter of 1.7

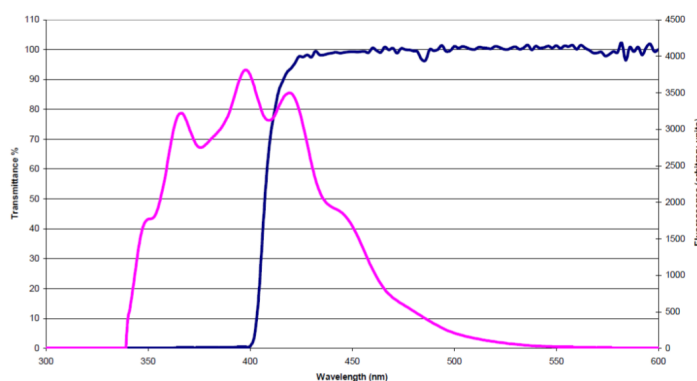


Figure 3.3: Transmittance (dark blue line) and fluorescent (light blue line) spectra for the CHANTI scintillator.

mm in which an optical WLS fiber is housed.

### 3.2.2 Optical fibers

The fiber is the fast multicladd blue to green shifter Saint-Gobain BCF-92 of 1 mm diameter. It is constituted by a polystyrene core and an acrylic coating ( $C_5H_8O_2$ , 3% of the radius). The core has a refractive index of 1.60 and a density of  $1.05 \text{ g/cm}^3$ , while the coating has a refractive index of 1.49 and a density of  $1.19 \text{ g/cm}^3$ . The fiber core is doped with a particular combination of compounds that let them absorb the light at one wavelength and re-emit it at a larger wavelength. In figure 3.4 [56] it is shown that the absorption has a maximum at 420 nm (blue light) while the emission have the maximum at 492 nm (green light). In this way the coupling between scintillator and fiber is optimized.

It has a decay time of 2.7 ns and an attenuation length of 3.5 m. The free space between the fiber and the scintillator is filled with an optical glue (SCIONIX<sup>®</sup>)

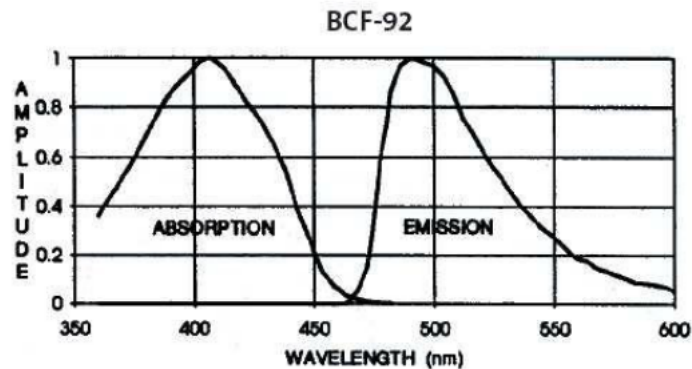


Figure 3.4: Absorption and emission spectra for the Saint-Gobain BCF-92 wavelength shifter fiber.

Silicon Rubber Compound RTV615). It provides excellent optical contact and has a very low outgassing rate [55].

The fiber is coupled at one end to a SiPM by means of a connector (figure 3.5 on the right) bonded to the scintillator with a high viscosity epoxy glue (Epoxy 3M DP490). To increase the portion of light collected, the other side of the fiber is mirrored by means of an aluminum deposition technique which was developed for the ALICE calorimeter (Al sputtering in vacuum [57]).

The connector is designed and constructed so as to ensure an optimal and stable coupling between the fiber and the SiPM. It is made of two parts: a base, in which the SiPM is housed, glued both to the scintillator and to the fiber, and a screw cap by which the SiPM is blocked so as to keep the optical coupling with the fiber itself. Both parts are made of aluminum and machined to a high precision.



Figure 3.5: Left: bar shape. Right: Fiber connector with SiPM.

### 3.2.3 Silicon photomultiplier

The SiPM is a ceramic package Hamamatsu S10362-13-050-C, which has a sensitive area of  $1.3 \times 1.3 \text{ mm}^2$ . It is a photodetector of the type MPPC (Multi-Pixel Photon Counter) consisting of a matrix of Avalanche Photo-Diodes (APD) that operate in Geiger regime (see figure 3.6).

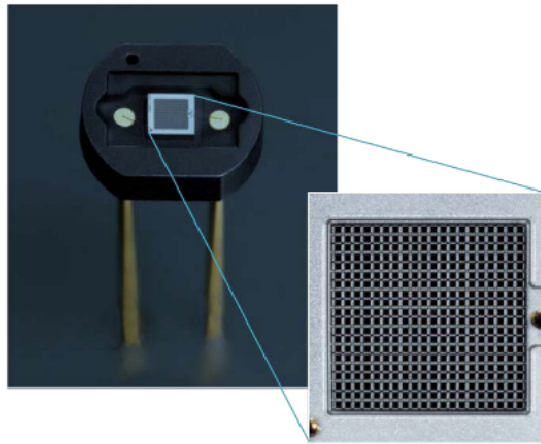


Figure 3.6: Photo of a Hamamatsu SiPM with a zoom on the active area showing the junction array .

The single cell has dimensions  $50 \times 50 \mu\text{m}^2$ ; the total number of cells is 667. The specifications provided by the manufacturer and referred to a temperature of operation of  $25^\circ\text{C}$  are:

- operation voltage typically about 70 V;
- photon detection efficiency (PDE), as quoted by manufacturer, slightly less than 50% for photons of 440 nm - peak of the spectral response - and higher than 40% between 370 and 520 nm;
- gain  $7.5 \times 10^5$ ;
- dark counting rate of the order of 800 kHz at a threshold of 0.5 photoelectron<sup>1</sup> (pe).

---

<sup>1</sup>For simplicity we use here and in the following the term photoelectron to indicate the primary electron (hole) generated by a photon hitting the SiPM.

The SiPM was chosen after testing samples of three different photodetectors from the Hamamatsu S10362 series, namely: 11-050C, 11-100C and 13-050C. The first two differ from 13-050-C as they have a sensitive area of  $1 \times 1 \text{ mm}^2$  with a cell  $50 \times 50 \text{ }\mu\text{m}^2$  the first and  $100 \times 100 \text{ }\mu\text{m}^2$  the second. We measured the responses of various devices coupled to the same bar of scintillator exposed to a collimated source of  $^{90}\text{Sr}$ . The measurements were carried out in a thermostatic chamber maintaining a fixed temperature of  $25^\circ\text{C}$  with an uncertainty better than  $0.1^\circ\text{C}$ . The SiPM signals, amplified  $\times 10$ , were fed into an oscilloscope Tektronix TDS5054 read out by using a GPIB connection and a LabView program. The 500 MHz bandwidth of the oscilloscope is more than sufficient to analyze signals with rise times of the order of a few ns. In order to select the SiPM we used as a figure of merit the signal amplitude normalized to the signal of single photoelectron, that was determined in advance by collecting dark noise signals [42]. The samples of the series 13-050C gave a number of photoelectrons between 20 and 25, systematically greater than that given by the SiPM from the other two series. SiPM, like all semiconductors, may be damaged when exposed to an intense neutron flux, however they remain substantially unaltered after irradiations not greater than about  $2\div 3 \times 10^9 \text{ neq/cm}^2$  ( $\text{neq} = 1\text{MeV}$  neutron equivalent) [58]. We checked by two different simulations, one made by FLUKA [59] and the other using GEANT4 [60], that this limit will not be exceeded in the two years of data taking foreseen for NA62. Indeed, the dose of neutrons integrated by the CHANTI SiPM is expected to be less than  $4 \times 10^8 \text{ neq/cm}^2/\text{y}$ [42].

### 3.3 Layout and assembly

CHANTI is made of six square counter hodoscopes (stations) of 30 cm side arranged in vacuum along the beam direction at distances of 27, 85, 200, 430, 890 and 1810 mm from GTK3 (figure 3.1). In order not to hinder the beam, the stations have a central hole of  $65 \times 95 \text{ mm}^2$  rectangular shape, with the longer dimension in the horizontal direction (x-axis) and the shorter in the vertical direction (y-axis). The geometry of the system is such that the CHANTI can intercept secondary particles, generated by beam interactions at the center of GTK3, which propagate in an angular region from 26.2 mrad to 1.38 rad with respect to the beam axis and has full acceptance for those running between 49 mrad and 1.34

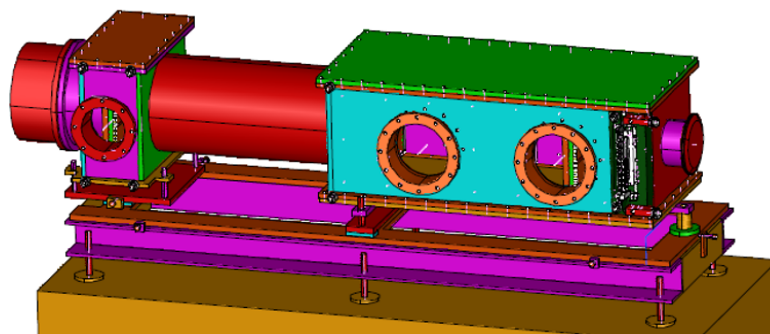


Figure 3.7: 3D Drawing of the vessel hosting GTK3 and the CHANTI stations.

rad.

A single vessel contains the first five CHANTI stations and the GTK3, while another one, connected to the previous one with a welded steel tube, contains the last CHANTI station (see figure 3.7). The biggest vessel is made by AISI 304L stainless steel plates welded together to form a rectangular box, with both top and bottom removable plates coupled via a suitable O-ring system to the rest of the box in order to keep the vessel vacuum tight and to provide at the same time easy access to the detector for maintenance, if needed. The vessel has two ISO-F 200 compliant holes closed by two flanges which host the signal feedthroughs (the smallest vessel has the same structure, but just one flange). These are SUB-D37 male-to-male T.I.G. welded connectors. Out of the 37 pins in one connector, one is unused, four are used to read Pt100 temperature probes (platinum resistance thermometers that are put inside the vessel to monitor temperature) and 32 are used to connect 16 channels. Each couple of pins is connected to coaxial cables on both sides of the flange and these lines are used both to polarize the SiPMs and to read the output signals.

Each station contains 46 bars of variable length, divided into two separate flat layers of scintillator, in contact with each other, formed by coupling and glueing the triangular bars in the manner specified earlier and shown in figure 3.2. One of the layers has the bars arranged in the horizontal direction (Y layer, 22 bars) and the other has the bars in the vertical direction (X layer, 24 bars). Because of the central hole we used bars of different lengths: long bars (300 mm), medium bars (117.5 mm) and short bars (102.5 mm). The X layer is composed of 10 long and 14 medium bars while the Y layer of 12 long and 10 short bars (figure 3.8).

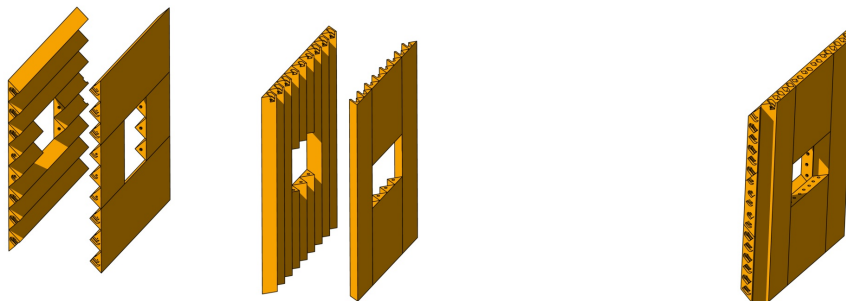


Figure 3.8: Left: Layer's structure. Right: CHANTI station.

The hit rate that each bar must support varies according to the position of the bar and along the bar itself. This rate has been carefully studied by means of a MonteCarlo (MC) simulation (see section 3.4). The two horizontal long bars (Y layer) closer to the hole for passage of the beam sustain the highest rate. In order to keep the maximum rate of each SiPM in the limit of  $\sim 1$  MHz, each of these bars has been divided into two halves, each one read by a separate SiPM. This causes the number of SiPM and, therefore, the number of readout channels of each station, to become 48. To minimize dead zones, the bars were divided with a cut transverse to their longitudinal axis and the two facing ends were painted with titanium dioxide in order not to have cross-talk. The realization of each station was done following four main steps:

1. SiPMs characterization
2. preparation of the bars with their fibers and connectors for SiPM,
3. quality test of the bars,
4. assembly of the station using only bars that passed the test.

### 3.3.1 SiPMs test

The SiPM gain depends linearly on the overvoltage  $V - V_{bd}$ , where  $V$  is the voltage applied to the SiPM (70V is a typical value) and  $V_{bd}$  is the breakdown voltage. So

we need to know and monitor  $V_{bd}$  which is a function of temperature (69.5 V is a typical value at 20 °C). We can do this using the Voltage-Current response of the SiPM. Near the breakdown region, this curve is approximated by  $I \propto (V - V_{bd})^2$  where  $I$  is the absorbed current. So we can measure  $V_{bd}$  by a fit to the V-I curve. We designed an automatic system to test 32 SiPM at the same time; it uses a power supply with a nano-amperometer (Keithley source-meter 2410 [61]) and an analog multiplexer, both controlled by a computer and LabView software. We performed the test in thermal chamber for a subset (25%) of the all SiPMs at 3 different temperatures: 20, 25 and 15 °C while the Hamamatsu specifies the SiPM properties only at 25°C. In this way, monitoring the temperature in the experimental area, we are able to change the voltage applied to the SiPM in order to keep the gain of the SiPM constant.

### 3.3.2 Preparation of the bars with their fibers and connectors for SiPM

Once SiPMs have been tested, the SiPM connector is bounded to each fiber, previously cut to the right length and mirrored by Al sputtering at the end opposite to SiPM. Once ready, the fiber is inserted into the hole of the bar, the connector is glued to the bar and the hole containing the fiber is filled with the optical glue, that was prepared in advance in the amount appropriate to the length of the bar. During the filling the bar was kept vertical and the glue was injected from the bottom. Both the preparation and the injection of the glue were carried out with great care to avoid the formation of air bubbles. Once completed with fibers and connectors, the bars were characterized by a quality test and accepted or not on the basis of the obtained results.

### 3.3.3 Test of the bars

The bars characterization is important because a bar that was used for the realization of a station can no longer be replaced (should it be faulty). In fact, since all elements which constitute a station are glued to each other, any apparatus malfunction can be remedied only by replacing the entire station.

The quality test of the bars and the characterization of each bar were made by

coupling the bar to a SiPM and studying its response to cosmic rays. The test was performed in two distinct ways: the first in self-trigger mode and the second using as trigger the signal of a telescope of two small scintillation counters (surface  $2.5 \times 2.5 \text{ cm}^2$ ) in coincidence. In both cases, the bar and the readout electronics were placed in a thermostatic chamber that allowed to maintain a constant temperature of  $25 \pm 0.1 \text{ }^\circ\text{C}$ . With the self-trigger test a comprehensive study was done of the response of the bar to cosmics going through in every part of the bar and in any direction. This allowed to have a sufficiently high rate of events, thus reducing considerably the measurement time. The signal of the SiPM, amplified by a trans-resistance amplifier, was collected by means of a fast digital oscilloscope Tektronix<sup>®</sup> TDS5054 connected to a PC. First of all the single photoelectron signal had been evaluated by studying the thermal noise produced by the SiPM not coupled to the bar. In this configuration the single photoelectron signal is of the order 10 mV. In order to get a rate of acquisition dominated by signals produced by cosmic rays, each signal was stored only if its amplitude exceeded 80 mV. Therefore the contribution from the thermal noise of SiPM was negligible. A fixed number of signals was acquired for each bar and the bar was characterized by calculating the ratio  $R (\leq 1)$  between the number of signals exceeding the threshold of 250 mV and the total. For the second type of test the trigger is given by the telescope of counters in order to select cosmic rays (muons) traveling approximately in the vertical direction. It was placed above the bar at the opposite side with respect to the SiPM. This way the bar responds to minimum ionizing particles crossing nearly perpendicularly to its longitudinal axis. To reduce the time required to test them all, the bars were tested two at a time, arranging one above the other below the trigger telescope. Again, the signals produced by the two SiPMs were amplified, digitized by the oscilloscope and acquired by a PC (as before), if they exceeded the threshold of 200 mV. Each signal was integrated with respect to time and a number of photoelectrons ( $n_{pe}$ ) produced by the event was calculated by comparison to the area of the signal of a single photoelectron. The bar was characterized using the average number of photoelectrons  $n_{pe}$ . After completing the measures, a two-dimensional plot (figure 3.9), in which each bar is represented by a point at coordinates  $(n_{pe}, R)$ , was built for each type of bar. Three ellipses were drawn on the plot, corresponding to variations of  $1\sigma$ ,  $2\sigma$  and  $3\sigma$  with respect to the average values  $(\bar{n}_{pe}, \bar{R})$ , obtained after a rotation done to find the

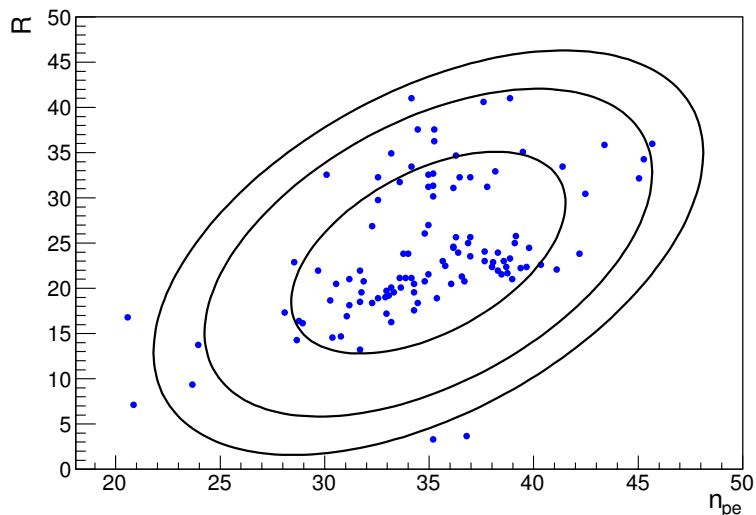


Figure 3.9: The result of tests of long bars.

two uncorrelated variables. About 6% of produced bars, the ones that fell outside the  $2\sigma$  contour and gave  $n_{pe} < \bar{n}_{pe}$  and  $R < \bar{R}$ , were discarded.

### 3.3.4 Assembly of the station

When all bars were ready, a station was assembled in two distinct stages, each of which took about one day.

During the first day the central half-X and half-Y layer were glued together in the following way. First of all the bars of the first half-layer were arranged, with the vertex at the bottom, on a special aluminum jig that guaranteed the correct positioning (figure 3.10). A series of glue droplets, each of about 0.1 ml of glue, were distributed using a mask on the plane formed by the base surfaces of the bars. Soon after that the bars of the second half-layer were positioned on that plane using a second template. The two half-layers were then loaded with a weight in order to exert an appropriate pressure to ensure a uniform distribution of the glue and a good bonding of the parts. The second day the complementary bars were glued with a similar procedure, thus completing the assembly. A total of about 20 ml of low out-gassing epoxy glue (3M DP490) was used for each station.



Figure 3.10: Steps of assembly. From left to right and top to bottom: half layer is arranged on the jig; teflon mask is aligned; glue spots are applied; mask is removed; bars of the other half layer are placed; second jig is applied on top to align last half layer and to distribute pressure; half module as it appears the day after gluing.

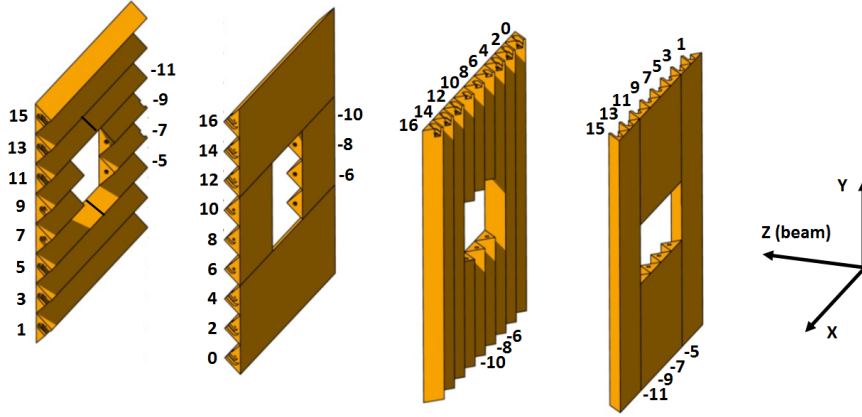


Figure 3.11: Channel identifier numbers for the two layers of one station.

### 3.4 Detector rate

A detailed MC simulation has been performed in order to study the expected rate of the detector. We developed a complete G4 simulation of the CHANTI materials and geometry, containing scintillating bars, fibers and aluminum frame, and it has been included in the official NA62 Monte Carlo which is used for this study. The digitization of the SiPM signal is still under development (see section 4.4). It includes the full signal shape simulation and profiting of the data collected during the 2015 run, it will be fine tuned to match with real data. For the aim of this study, however, we simply parametrized the bar response by means of a cut on the energy deposit: a CHANTI bar is considered "fired" if there is an energy deposit larger than  $1/3$  of the energy released, on average, by a Minimum Ionizing Particle (MIP) crossing orthogonally the bar.

In the NA62MC a CHANTI channel of each layer (X layer where the bars are arranged in the vertical direction and Y layer where the bars are arranged in the horizontal one) is identified by an integer number as shown in figure 3.11. The channel numbers in figure 3.11 are drawn on the SiPM side (while the other side of the fiber inside the bar is mirrored). The horizontal layer has the bars closest to the central hole (bars -5, 5, -11, 11) divided into two halves respect to the longest bars. The stations are named A (the closest to the GTK3), B, C, D, E, F.

Together with the CHANTI, also the KTAG, the GTK and the collimators are used in the simulation (NA62MC ver. 736). In the nominal configuration, that

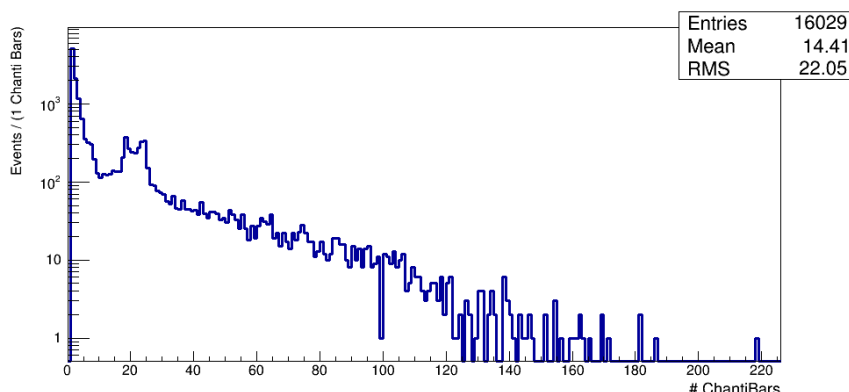


Figure 3.12: Distribution of the number of CHANTI bars fired for events where at least one bar is fired.

will be implemented in the final experimental apparatus, the thickness of the three GTK stations is  $\sim 100\mu\text{m}$ . Instead in these simulations the thickness of the GTK1 is  $450\mu\text{m}$ , for the GTK2 it is  $250\mu\text{m}$  and for the GTK3 it is  $100\mu\text{m}$ : this is the configuration used for the 2015 data taking. The following particles have been generated:

- 525000 positive pions
- 173000 protons
- 45000 positive kaons
- the muon halo surrounding the beam made up of 99143 (11791)  $\mu^+$  from  $\pi^+$  ( $K^+$ ) decay and 21374 (3034)  $\mu^-$  from  $\pi^-$  ( $K^-$ ) decay

The previous numbers of particles are what you expect in 1 ms of the beam. The number of bars fired in each simulated event in which there is at least a bar fired is shown in figure 3.12. The peak at about 20 bars is due to muons that cross all the CHANTI stations. The entries of the histogram provides the total rate (in KHz) of the event in which at least one bar is fired on the entire detector.

The rates of the bars in each CHANTI layer have been evaluated and they are shown in figure 3.13 (X layer in station A), 3.14 (Y layer in station A), 3.15 (X layer in station B), 3.16 (Y layer in station B), 3.17 (X layer in station C), 3.18 (Y layer in station C), 3.19 (X layer in station D), 3.20 (Y layer in station D), 3.21

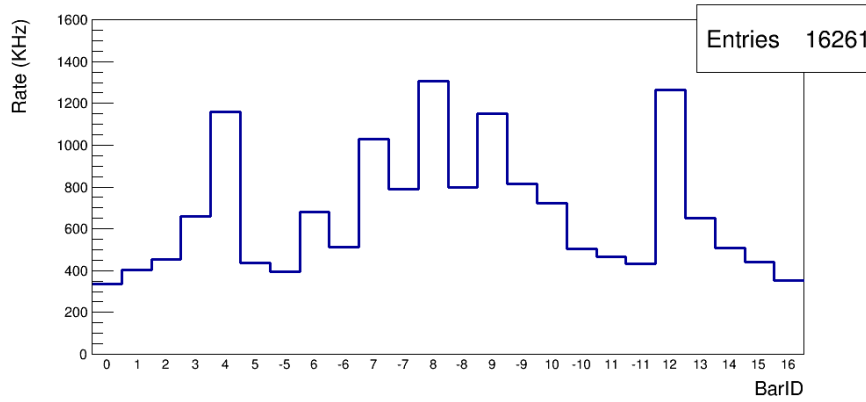


Figure 3.13: Rate of CHANTI bars in the X layer of station A.

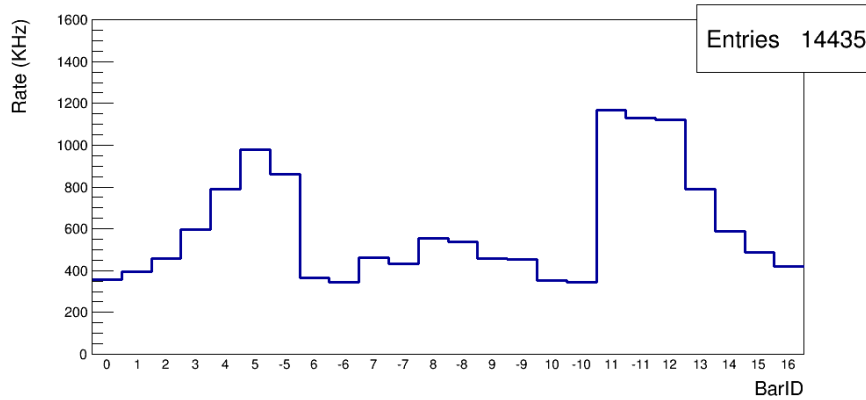


Figure 3.14: Rate of CHANTI bars in the Y layer of station A.

(X layer in station E), 3.22 (Y layer in station E), 3.23 (X layer in station F), 3.24 (Y layer in station F).

In the first design of the CHANTI detector there was just one long bar in place of the bars 5 and -5 (the same for the bars 11 and -11) in the Y layers. This bar was the hottest one with a rate higher than 2 MHz and, as a consequence, out of the capability rate of the the front-end electronics. So after this simulation the modification, consisting in cutting the hottest bars next to the central hole, has been proposed and realized. From the bars rate in the Y layer it is clear an asimmetry up-down that is due to the beam profile [42]. This can be seen also in the X layer if the medium bars with positive channel ID (in particular 6, 7, 8 and 9) are compared with the bars with opposite ID (in particular -6, -7, -8 and -9).

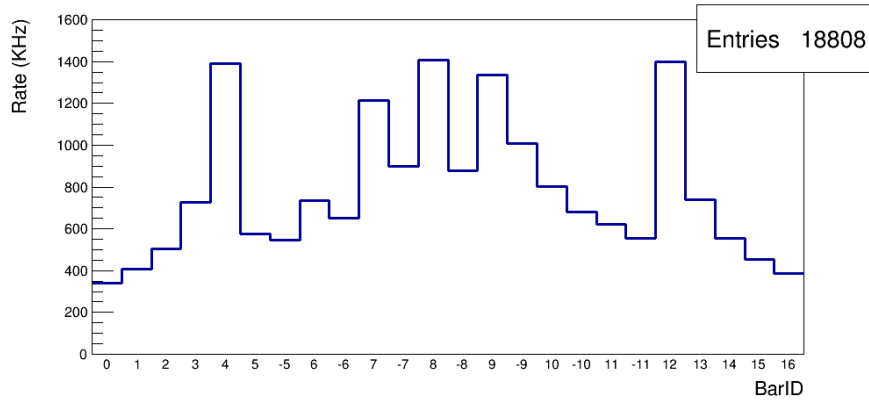


Figure 3.15: Rate of CHANTI bars in the X layer of station B.

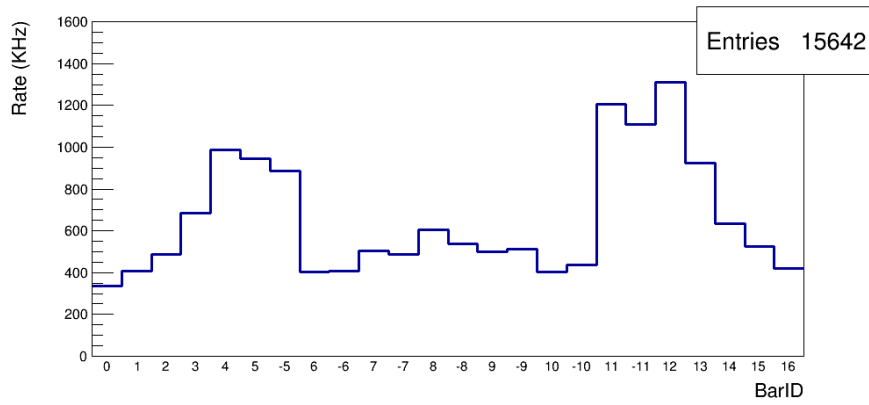


Figure 3.16: Rate of CHANTI bars in the Y layer of station B.

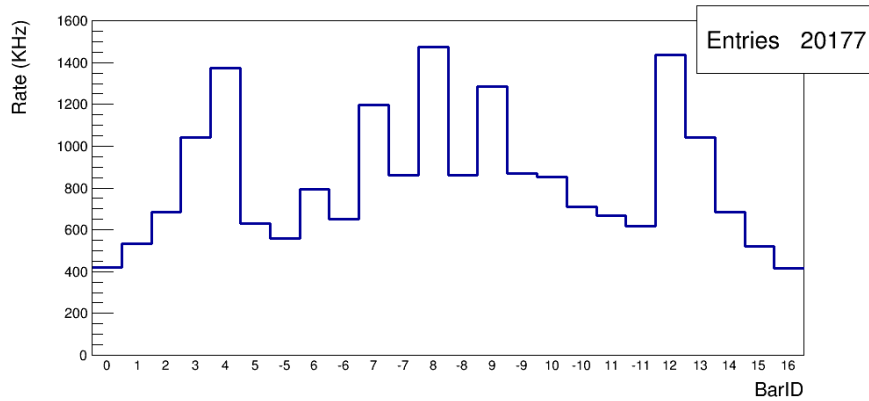


Figure 3.17: Rate of CHANTI bars in the X layer of station C.

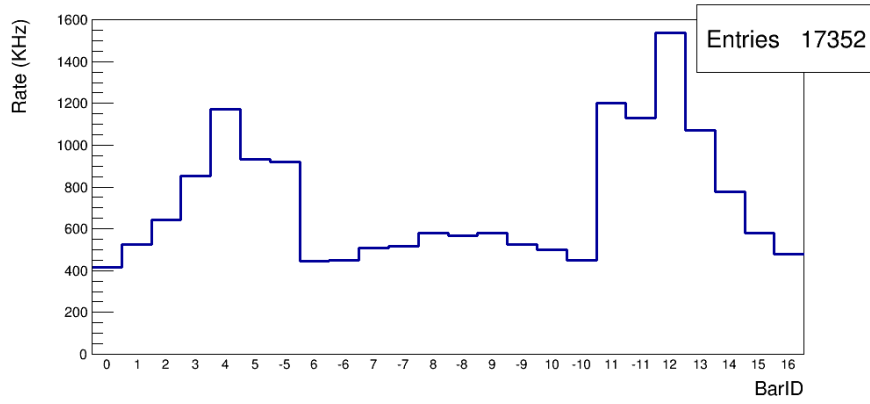


Figure 3.18: Rate of CHANTI bars in the Y layer of station C.

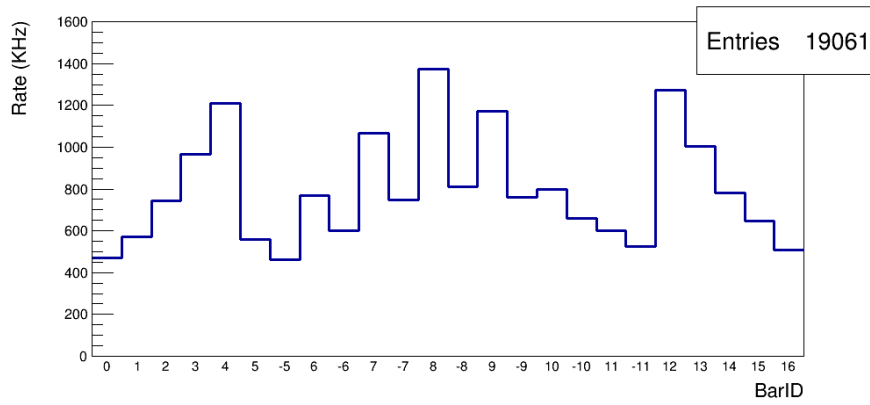


Figure 3.19: Rate of CHANTI bars in the X layer of station D.

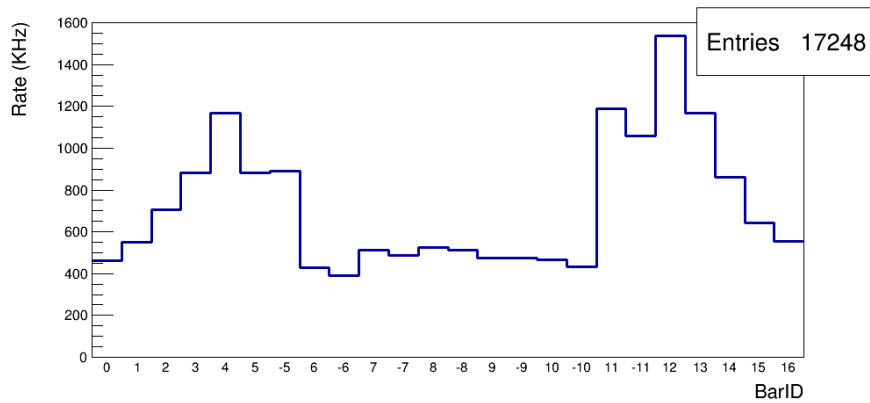


Figure 3.20: Rate of CHANTI bars in the Y layer of station D.

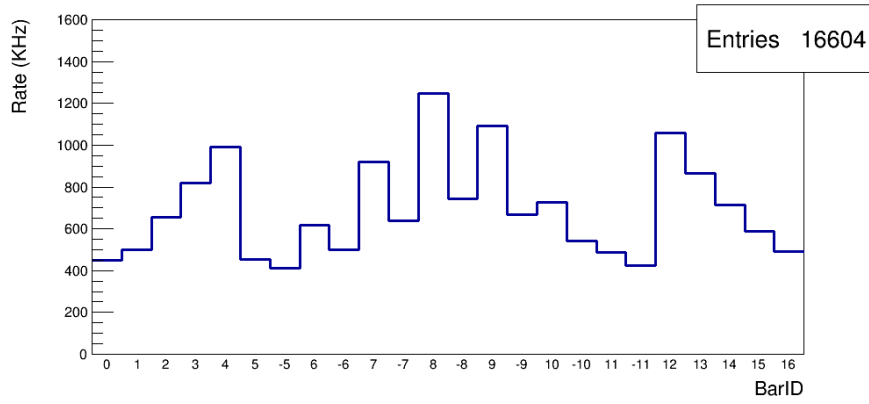


Figure 3.21: Rate of CHANTI bars in the X layer of station E.

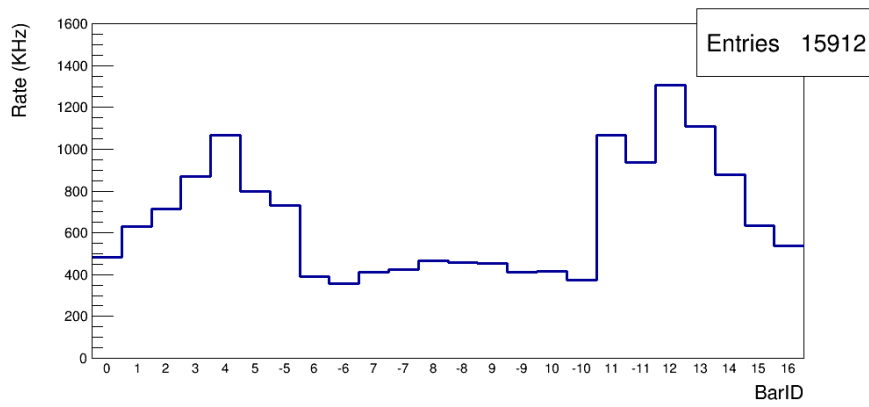


Figure 3.22: Rate of CHANTI bars in the Y layer of station E.

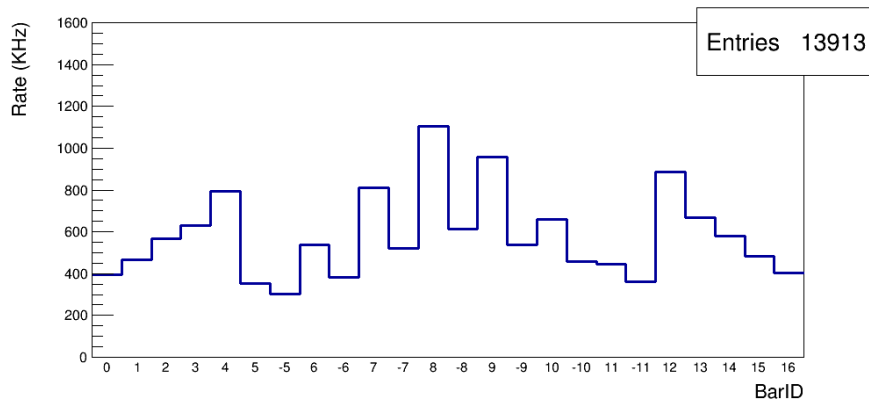


Figure 3.23: Rate of CHANTI bars in the X layer of station F.

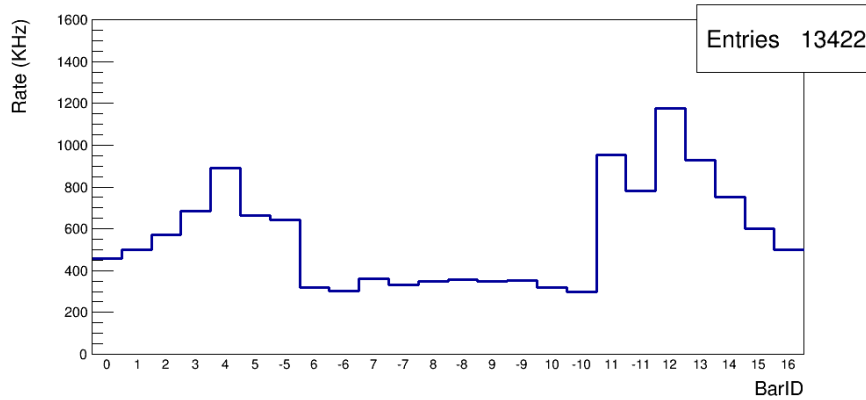


Figure 3.24: Rate of CHANTI bars in the Y layer of station F.

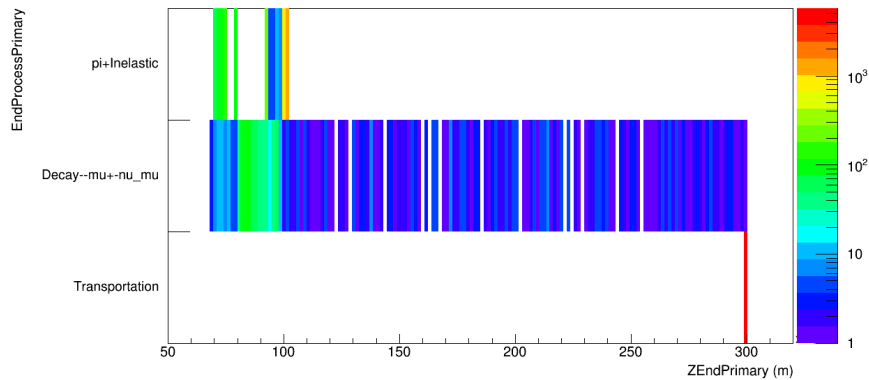


Figure 3.25: End process name of the beam pion simulated in which at least one CHANTI bar is fired as a function of the Z coordinate of the pion end.

Different processes, coming from the various particles generated in the simulation, contribute to the total CHANTI rate. Concerning the pion, it can decay, do some inelastic interaction or reach the bound of the simulated world (this process is called "transportation" event): figure 3.25 shows the process name of the pion end for the events in which at least one CHANTI bar is fired as a function of the Z coordinate of the pion end. The Z coordinate of the GTK3 is 102.4 m. In transportation and  $\pi^+ \rightarrow \mu^+ \nu_\mu$  events with Z vertex decay after the CHANTI position, particle hitting CHANTI comes from quasi-elastic interaction <sup>2</sup> of the pion

<sup>2</sup>Quasi-elastic interactions of pions are topologically characterized by an out-coming pion almost identical to the incoming one and the production of low energy electron (delta-ray) or

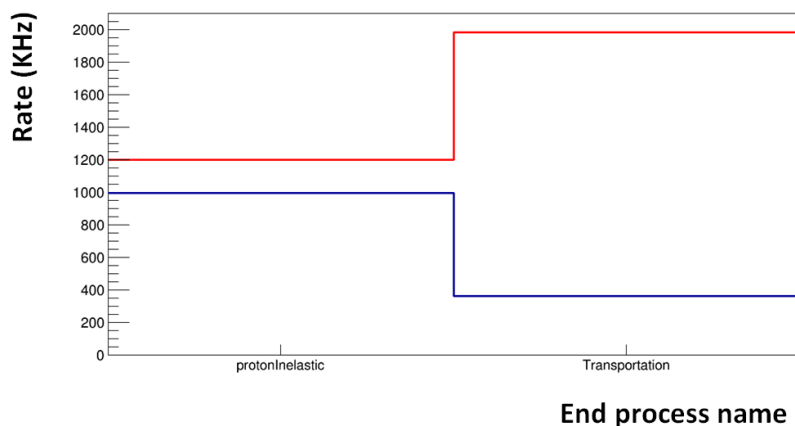


Figure 3.26: End process name of the beam proton simulated for events with at least one CHANTI bar fired (red curve) and with at least two CHANTI bars crossing in one station (blue curve).

with material upstream respect to the CHANTI position, in particular with the GTK3. While for the  $\pi^+ \rightarrow \mu^+ \nu_\mu$  decay before CHANTI, it is the muon itself that hits CHANTI.

The same kind of behaviour affects the other particles of the beam. The products of the quasi-elastic interaction (apart from the outgoing pion/kaon/proton) have low energy and the variation of the momentum of beam particle (e.g. kaon) due to the quasi-elastic events is compatible with the momentum resolution capability of the GTK system. So CHANTI should not introduce a fake veto (that will be discussed and measured on real data in section 5.5) on these kind of events since they can be used in the data analysis for the  $K^+ \rightarrow \pi^+ \nu \bar{\nu}$  research. In order to do this, two bars crossing in one station should be the minimal requirements to perform a veto with the CHANTI. Figure 3.26 and 3.27 show the end process name respectively of proton and kaon when at least one bar is fired (red curve) and when there are at least two bars crossing in one station (blue curve).

It is important to stress that 3 out of 105 kaon inelastic on the GTK3 event, detected with at least one CHANTI bar fired, are not detected when a cut with a crossing configuration is applied. However the detectors redundancy of the NA62 apparatus ensures that the rejection efficiency for kaon inelastic interaction on nucleon.

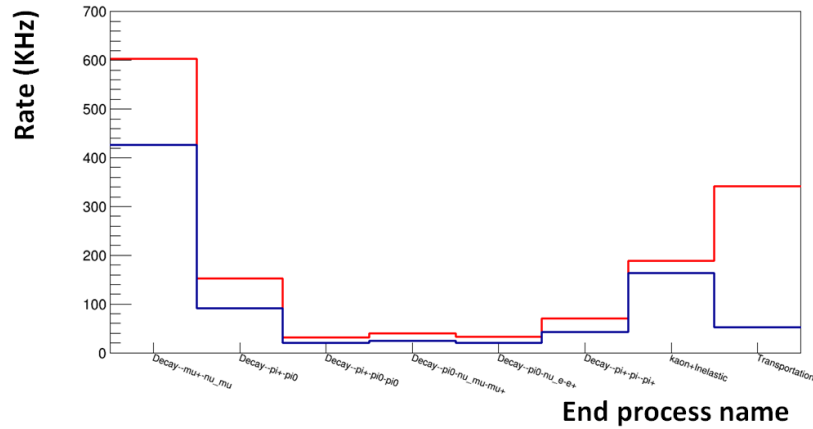


Figure 3.27: End process name of the beam kaon simulated for events with at least one CHANTI bar fired (red curve) and with at least two CHANTI bars crossing in one station (blue curve).

GTK3 is in perfect agreement with the experimental requests. It has already been studied in [62].

Concerning halo, the unique end process of muon is "transportation", since they contribute to CHANTI rate because they pass through the CHANTI station or they do quasi-elastic scattering with material before CHANTI.

The total event rate on CHANTI with the different contributions can be summarized as follows:

1. the rate of event in which at least one bar is fired is 16 MHz with
  - 9.7 MHz due to pions or its decay;
  - 3.2 MHz due to protons or its decay;
  - 1.4 MHz due to kaons or its decay;
  - 1.8 MHz due to muons or its decay;
2. the rate of event in which at least two crossing bars are fired is 7.2 MHz with
  - 3.8 MHz due to pions or its decay;
  - 1.4 MHz due to protons or its decay;
  - 0.8 MHz due to kaons or its decay;

- 1.2 MHz due to muons or its decay;

Because of these rates, while apparently the cut on the number of fired bars has a negligible impact on the signal [62], the main mechanism through which this cut will reduce the signal  $K^+ \rightarrow \pi^+ \nu \bar{\nu}$  efficiency is the accidental coincidences of the CHANTI activity in the time window around a given trigger. It is for this reason that the CHANTI time resolution plays a very important role in the detector design. The time resolution of the CHANTI on real collected data will be reported in section 5.2

## Chapter 4

# CHANTI front end electronics: calibration and signal simulation

The CHANTI system has a front end electronics (FEE) organized on a two level scheme. At first stage the CHANTI-FE boards provide the bias voltage to each SiPM and perform a fast amplification of the input signal. At second stage the analog signal generated by the CHANTI-FE is processed by a Time Over Threshold (ToT) board, that provides a low voltage differential signal (LVDS) whose state depends on the fact that the input signal stays above a programmable threshold [63]. Then the LVDS signals are sent to a standard TEL62+TDCB readout system (see section 2.7). A block diagram of the read-out electronics is shown in figure 4.1.

In this chapter the calibration procedure of the two electronic stages are described, together with a simulation of the signal produced by CHANTI front-end electronics based on Geant4 toolkit and C++ routines.

### 4.1 CHANTI-FE board

The SiPMs by Hamamatsu used in the CHANTI are characterized by a typical operative reverse voltage of about 70 V. They are not well suited to be used with typical commercial HV power supply, since their gain is quite sensitive to relatively small changes in the voltage bias which must be controlled at better than permille level to achieve a satisfactory operating stability. Moreover since

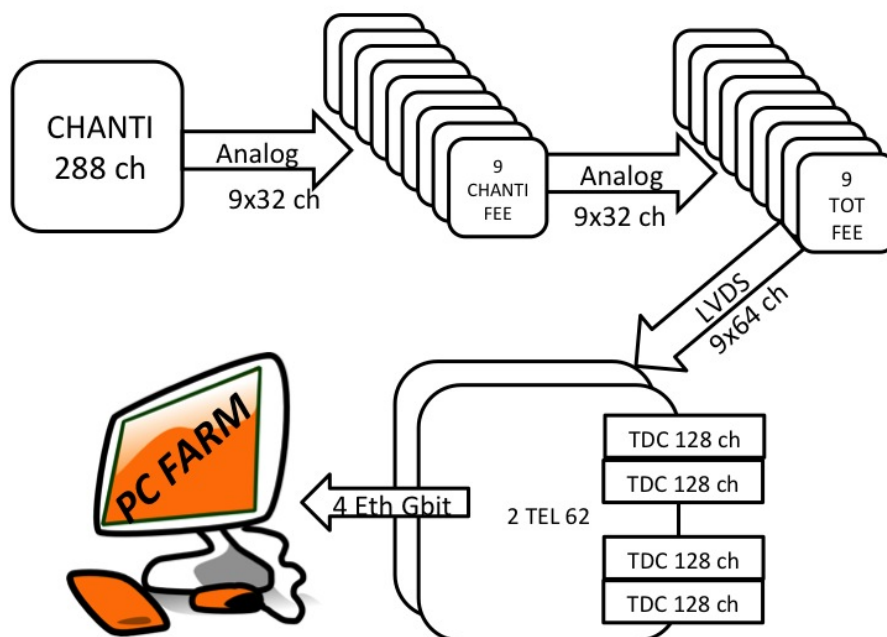


Figure 4.1: Block diagram of the CHANTI read out electronics.

the typical signal they produce is relatively small, it must be amplified before it can be discriminated and/or digitized. For the CHANTI we have thus designed, in collaboration with "Servizio Elettronica-Laboratori Nazionali di Frascati" of INFN, a custom all-in-one FEE board (CHANTI FE) .

### 4.1.1 CHANTI-FE description

The CHANTI-FE is a 9U VME standard board with three different functions:

1. provides for the SiPM V-bias and monitoring of SiPM current;
2. checks the temperature stability of CHANTI station reading Pt100 probes (platinum resistance thermometers), four of which are installed on each station;
3. receives signals from SiPM and transfers them to the next stage through trans-resistance amplifiers.

Each card has 32 channels (so 9 boards are needed to power all the CHANTI channels) that enter and leave through sub-DB (37 pin) connectors, and is able

to monitor 4 two-pin Pt100 probes. In order to achieve the necessary stability of the SiPM performance, each channel must have a stability of the bias voltage of order 10 mV for typical bias voltages of order 70 V. The dark currents, which at room temperature and in normal operating conditions are typically of order 100- 200 nA, are read with an accuracy of 1 nA. Analog to digital conversion to read the channel voltage and currents is made via AD7708 16 bit ADC for each channel, while the applied voltage is controlled and set individually for each SiPM via LTC2620 12 bit DAC. The reading of the Pt100 probes is used in the software control system of the detector to adjust the bias voltage of each SiPM in order to maintain it at a fixed working point. The fast amplifier, providing a factor 25 on signal amplitudes for 50 Ohm impedance, has a cutoff frequency of 80 MHz. It is chosen to reach a reasonable compromise between the need to follow the risetime of the signals and the necessity to keep to an acceptable level high radio-frequency noise.

The communications with the CHANTI-FE are operated with both a CANopen protocol through two RJ-45 connectors and serial communication protocol through USB-B connector.

### **4.1.2 CHANTI-FE calibration**

A careful calibration procedure for the CHANTI-FE boards has been setup in order to precisely control and readout the value of the bias voltage and to monitor the current of each channel. The procedure needs a nano-amperometer (Keithley source-meter 2410 [61]) and an analog multiplexer, both controlled by a computer and LabView software, and a calibrated high resistance (HRRS Series High Resistance Decade Box [64]). The HRRS Series High Resistance has a systematic uncertainty of the order of permille: this is necessary in order to reach the same level of uncertainty for the applied bias voltage, evaluated with this calibration procedure. All these devices are arranged as shown in figure 4.2.

The calibration of each channel is obtained by setting the voltage in DAC units and measuring the current-voltage (I-V) curve of the high impedance calibrated resistors by means of the Keithley. Also the voltage and current values measured by the ADC of the CHANTI-FE are saved in order to have the calibration of the ADC itself. The calibration was performed with two different resistive loads,  $1\text{G}\Omega$

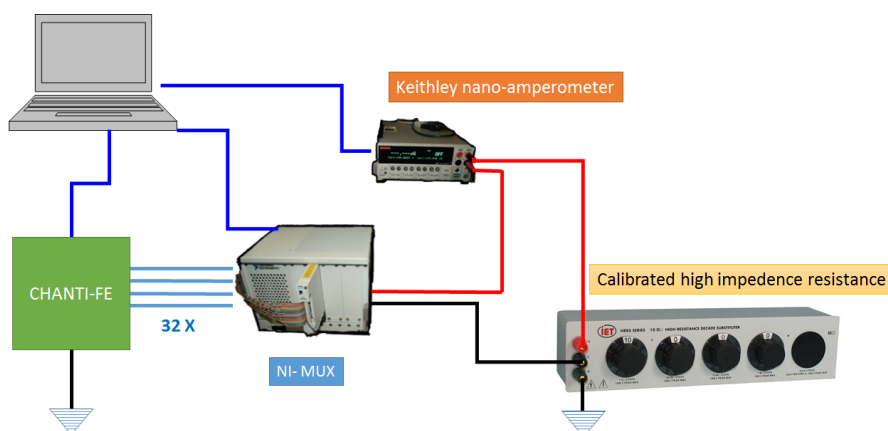


Figure 4.2: Setup for CHANTI-FE calibration. Each channel is connected by means a MUX to a series of a nano-amperometer and a high resistance.

and  $500\text{M}\Omega$ : these values have been chosen in order to have currents flowing in the circuit of the order of  $\sim 100\text{ nA}$  (the same order of magnitude of the dark current of the SiPM). The calibration parameters have been evaluated through the following linear fits

1. linear fit to the distribution of the current ( $I_m$ ) measured by the nano-amperometer VS the current ( $I_{ADC}$ ) measured by the ADC, (figure 4.3 shows this calibration for one single channel):

$$I_m = ISlope\_R \times I_{ADC} + IConst_R \quad (4.1)$$

2. linear fit to the distribution of the voltage ( $V_m$ ) evaluated by means of  $I_m$  and the value of the high resistance (taking into account the internal resistance of the nano-amperometer) VS the voltage ( $V_{DAC}$ ) set with the DAC (figure 4.4 shows this calibration for one single channel):

$$V_m = VSlope\_S \times V_{DAC} + VConst_S \quad (4.2)$$

3. linear fit to the distribution of the voltage  $V_m$  VS the voltage ( $V_{ADC}$ ) read with the ADC (figure 4.5 shows this calibration for one single channel):

$$V_m = VSlope\_R \times V_{ADC} + VConst_R \quad (4.3)$$

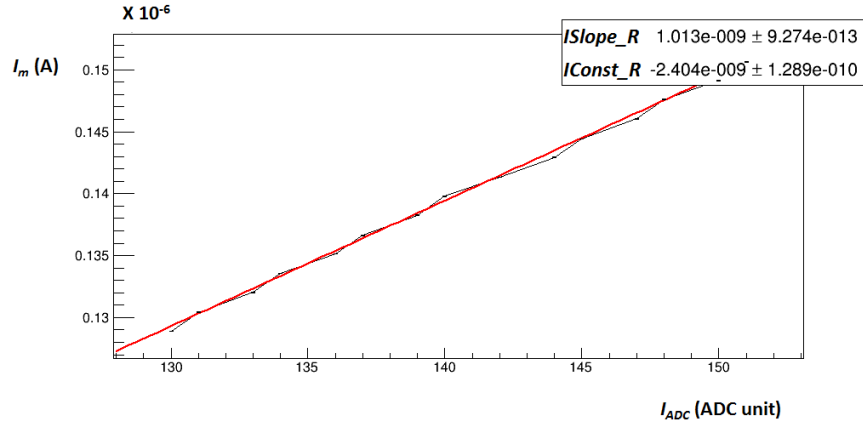


Figure 4.3: Linear fit to the distribution of the current ( $I_m$ ) measured by the nano-amperometer VS the current ( $I_{ADC}$ ) measured by the ADC for one channel of a CHANTI-FE board closed on 500 M $\Omega$  load.

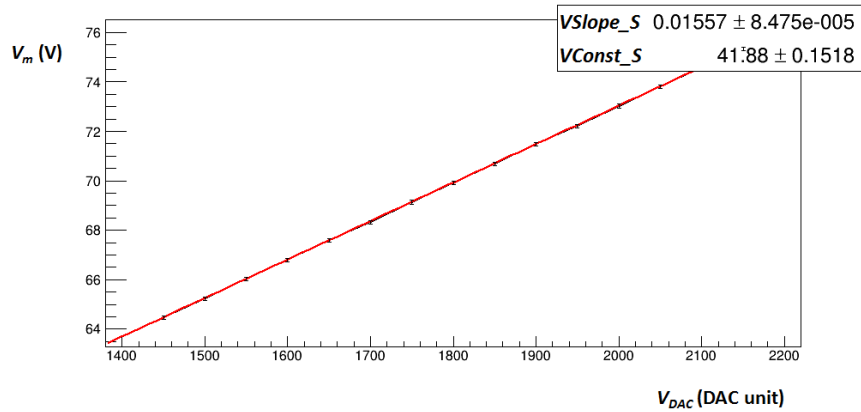


Figure 4.4: Linear fit to the distribution of the voltage ( $V_m$ ) evaluated by means of the nano-amperometer and the high resistance (500M $\Omega$ ) VS the voltage ( $V_{DAC}$ ) set with the DAC for one channel of a CHANTI-FE board.

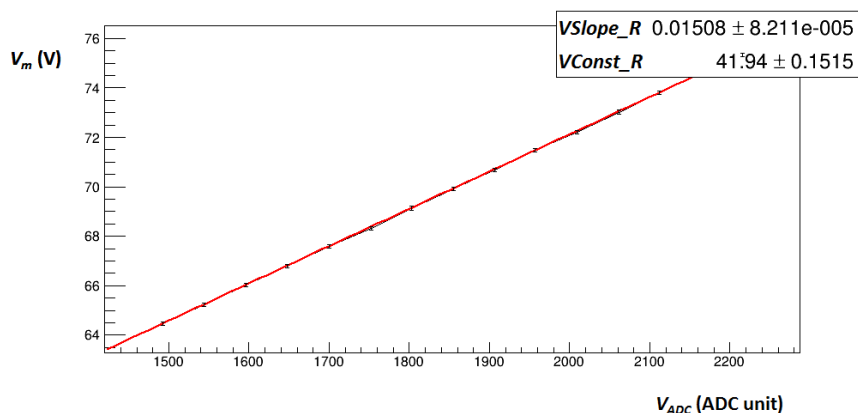


Figure 4.5: Linear fit to the distribution of the voltage ( $V_m$ ) evaluated by means of the nano-amperometer and the high resistance ( $500\text{M}\Omega$ ) VS the voltage ( $V_{ADC}$ ) read with the ADC for one channel of a CHANTI-FE board.

The distributions of the calibration parameters  $VSlope_S$ ,  $VConst_S$ ,  $VSlope_R$ ,  $VConst_R$ ,  $ISlope_R$  and  $IConst_R$  measured for all the channels of 11 CHANTI-FE boards (2 boards are spares) with the  $500\text{M}\Omega$  are shown respectively in figure 4.6, 4.7, 4.8, 4.9, 4.10 and 4.11.

A final overall scale factor of 0.1% is applied to bias voltage provided by the CHANTI-FE (a 0.07% systematic uncertainty on the resistors impedance is in fact quoted by the manufacturer). This factor was evaluated in order to obtain fully agreement of the absolute voltage/current settings and readout between the CHANTI-FE and the Keithley source-meter 2410. In figure 4.12 the I-V curve obtained for one typical SiPM channel is compared for the CHANTI-FE (in red) and the Keithley source-meter (in blue).

Also the calibration of the ADC channels dedicated to the temperature monitor was performed. The Pt100 thermometers have a predictable change in resistance as the temperature changes, so these channels have to detect variations of the load resistance. Then the calibration procedure was done connecting different values of resistance (from  $100\ \Omega$  to  $110\ \Omega$ ), in place of the Pt100, and monitoring the value of the ADC read.

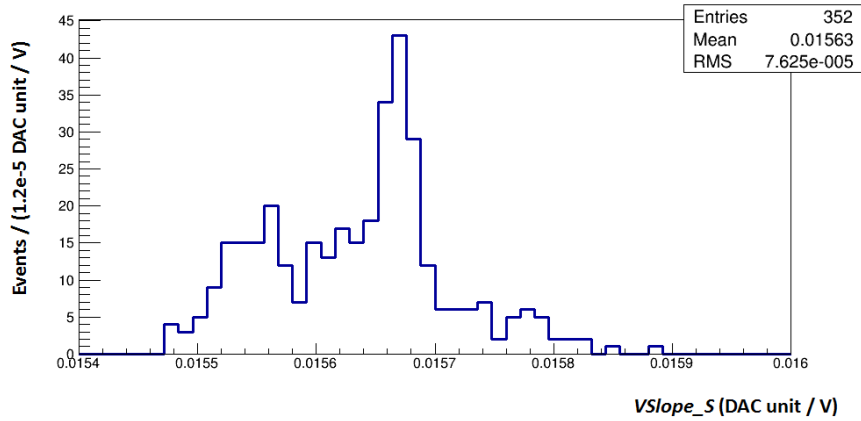


Figure 4.6: Distribution of the calibration parameter  $VSlope\_S$  (see eq. 4.2).

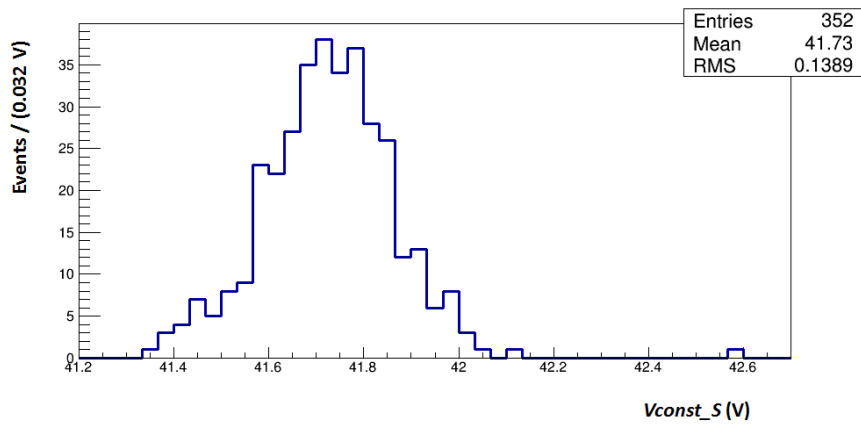


Figure 4.7: Distribution of the calibration parameter  $VConst\_S$  (see eq. 4.2).

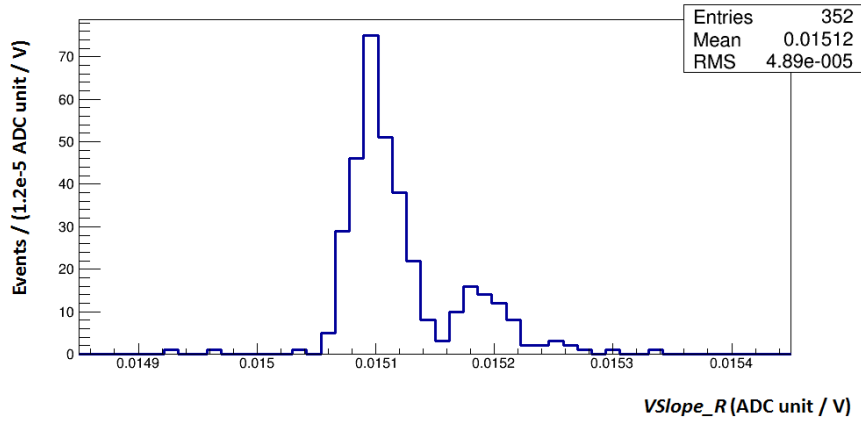


Figure 4.8: Distribution of the calibration parameter  $VSlope\_R$  (see eq. 4.3).

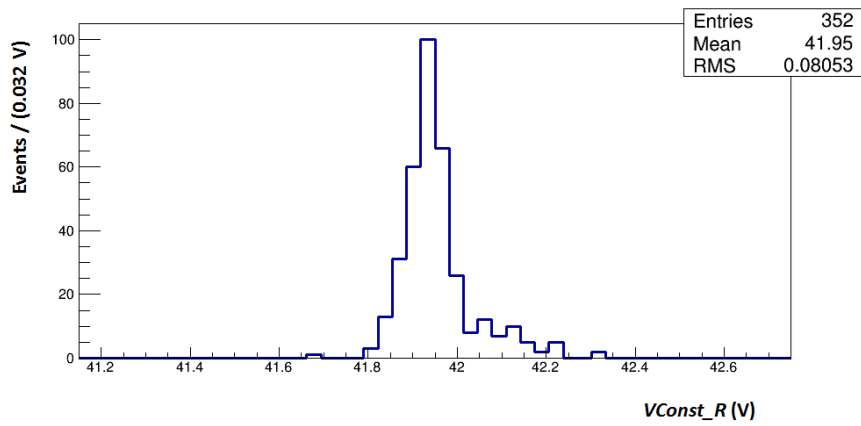


Figure 4.9: Distribution of the calibration parameter  $VConst\_R$  (see eq. 4.3).

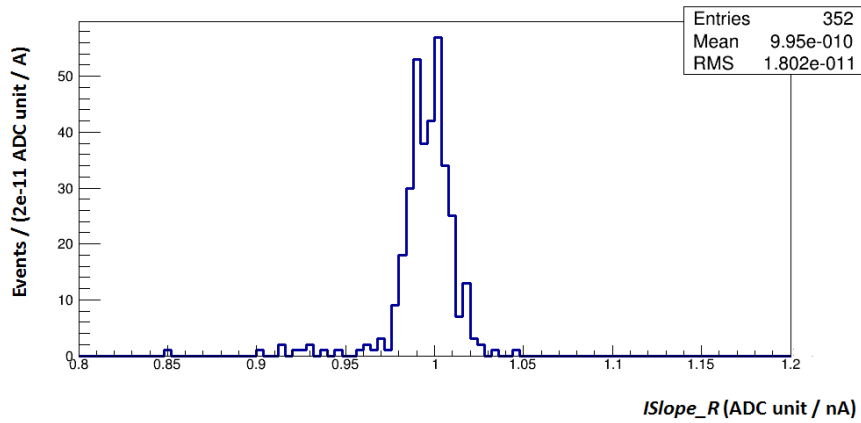


Figure 4.10: Distribution of the calibration parameter  $ISlope\_R$  (see eq. 4.1).

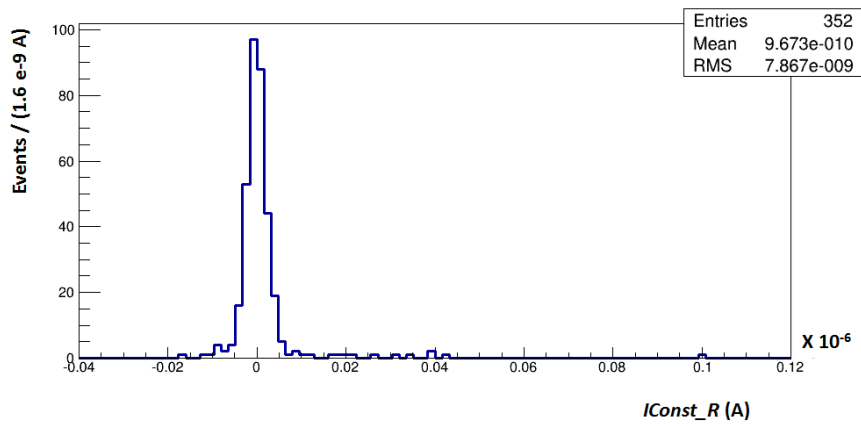


Figure 4.11: Distribution of the calibration parameter  $IConst\_R$  (see eq. 4.1).

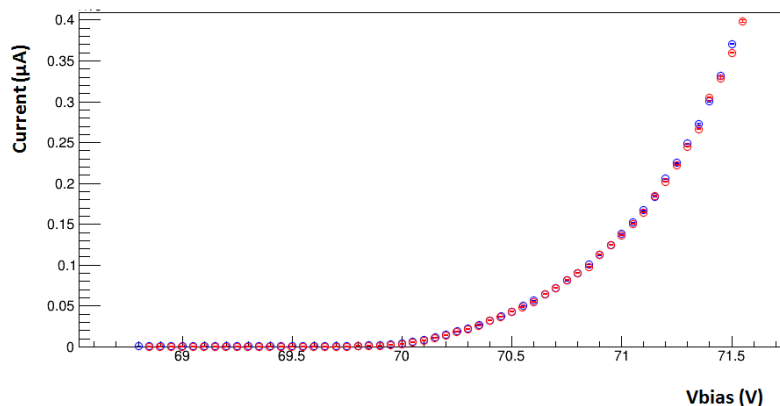


Figure 4.12: Comparison of the I-V curves of a SiPM measured with the Keithley source-meter (blue points) and the CHANTI-FE (red points) after the calibration procedure.

## 4.2 ToT board

After the CHANTI-FE, the analog signal is processed by a Time Over Threshold (ToT) board, that digitizes and sends it to a standard TEL62+TDCB readout system. In this section the description and calibration of the ToT board are reported.

### 4.2.1 ToT board description

The ToT board is implemented on a 9U VME standard layout and it is adapted from LAV (Large Angle Vetoes) read-out electronics of NA62 [63]. It has J1 power connector only at the top of the backplane side, while at the bottom the 32 analog inputs are connected to the board using two DB37 connectors. Each input analog signal is filtered by means of an amplifier/splitter that produces two identical copies of the signal and feeds them to two comparators. These devices compare the input with programmable thresholds that can be adjusted using a 12 bit resolution DAC. Each comparator converts the analog input into a LVDS output whose logic level depends on the fact that input signal is above the selected threshold. So the logic level of the LVDS signal changes when the leading edge and the trailing edge of the analog input crosses the threshold. Since two different comparators are used for each input, two thresholds can be defined for each analog signal (low threshold

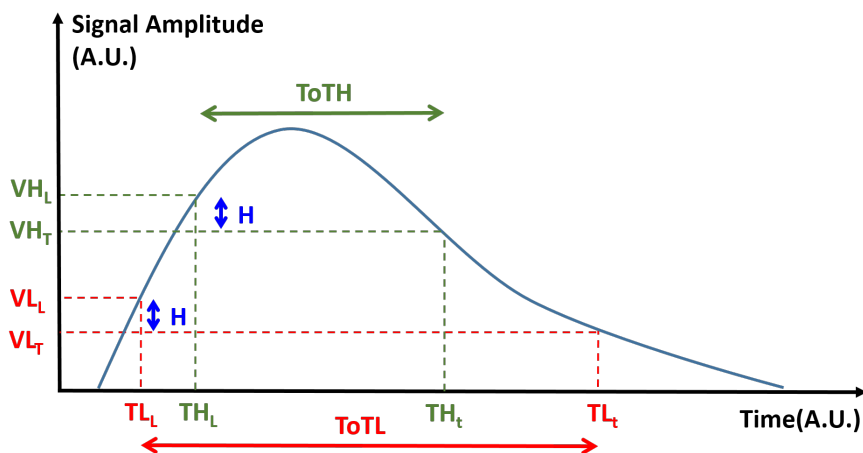


Figure 4.13: Each analog input signal is compared with two programmable voltage thresholds (High and Low). The low (high) threshold has two switching points:  $VL_L(VH_L)$  is for rising voltages and  $VL_T(VH_T)$  is for falling voltages; the voltage difference between the two switching points ( $H$ ) is called hysteresis. The time the input signal stays above the low (high) threshold,  $ToTL$  ( $ToTH$ ) equals the time the LVDS output for that threshold stays in a well defined logic level.

$VL_T$  and high threshold  $VH_T$ ). Then to each input analog signal correspond two LVDS output signals and this arrangement is useful for time-walk correction (see section 5.2).

Small voltage fluctuations due to noise, always present on the inputs, can cause undesirable rapid changes between the two output states when the input approaches one of the threshold level. To prevent this output oscillation, a small hysteresis of a few millivolts is integrated into each comparator. In place of one switching point, hysteresis introduces two: one for rising voltages and one for falling voltages. The voltage difference between the two switching points equals the hysteresis voltage (see figure 4.13). After the installation of the detector and the cabling of the CHANTI-FE boards, a noise level less than 5 mV peak-to-peak was measured in the experimental environment at the output of the CHANTI-FE; thus a value of 5 mV was chosen for the hysteresis.

The 64 LVDS signals produced are sent to TDCs contained in the TEL62 board using two SCS12 connectors placed on the front of the card. Then the TDCs generates a collection of leading and trailing times that corresponds to the switching points of the LVDS signal level. The analog input signals of the ToT board are

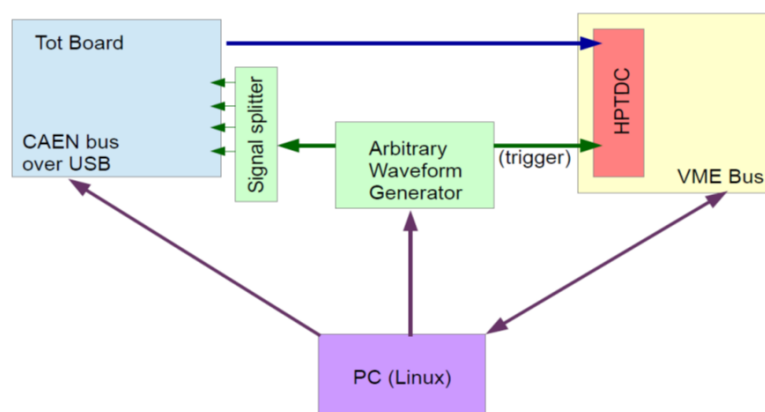


Figure 4.14: Experimental setup for ToT board calibration.

also added four by four and sixteen by sixteen; the result is available on  $8 + 2$  connectors LEMO00 for the purpose of monitoring. The setting of the thresholds and the communications with DAC card are operated with both a CANopen protocol through two RJ-45 connectors and serial communication protocol through USB-B connector.

## 4.2.2 ToT board calibration

The calibration procedure for the ToT board has been performed in order to precisely control the setting of the threshold. The experimental setup shown in figure 4.14 has been implemented. The Arbitrary Waveform Generator (AWG) Tektronix AFG3252 [65] provides an input signal (that mimics the SiPM signal) to all the channels of the ToT board through a custom resistive signal splitter designed by the "Servizio Elettronico e Rivelatori" (SER) of Naples. At the same time, the AWG generates the trigger for the Caen High Performance TDC (HPTDC) V1190B [66] that receives as input the LVDS signals from the ToT board. The HPTDC is installed inside a VME crate and its model is the same of the one mounted on the TEL62. Thus for each LVDS input signal, a collection of leading and trailing times are generated and the data are sent via VME bus to a computer. The latter controls also remotely the AWG and the ToT board for the threshold setting with a serial communication protocol.

Two kinds of input signal configurations were generated by the AWG (see figure 4.15). The input pulse in configuration "a" has a rise time of 10 ns, a constant

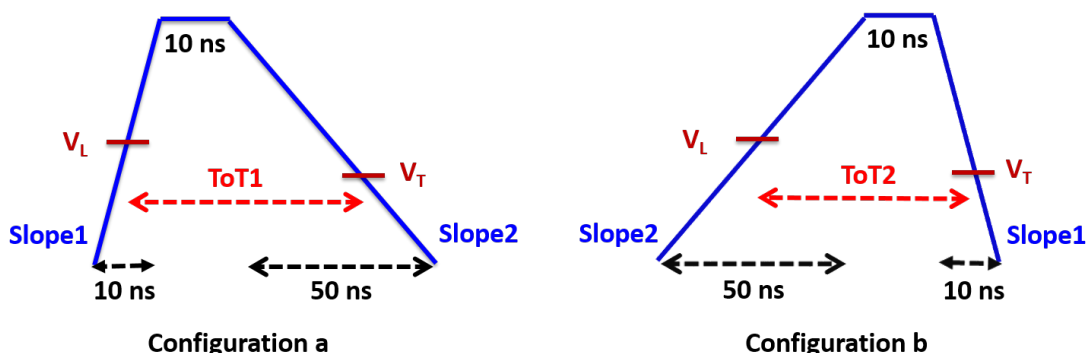


Figure 4.15: Signals generated by the AWG and used as input for the ToT board during its calibration procedure.

part of 10 ns and finally a fall time of 50 ns. The one in configuration "b" is just "mirrored". Setting the threshold  $V_L$  with the ToT board (in DAC unit), it is possible to evaluate the two time over threshold ( $ToT1$  and  $ToT2$ ) in the two configurations. Since the trailing threshold ( $V_T$ ) is different from the leading one because of hysteresis, the two measured ToT are different.

Indeed they satisfy the following equation ( $SignalLength$  is 70 ns in our configurations):

$$ToT1 = SignalLength - V_L/Slope1 - V_T/Slope2 \quad (4.4)$$

$$ToT2 = SignalLength - V_L/Slope2 - V_T/Slope1 \quad (4.5)$$

from which one can simply evaluate the value of  $V_L$  in volt unit and then compute the calibration parameters for the threshold setting of the DAC with the linear fit

$$V_L(mV) = Slope_{tot} \times V_L(ADC) + Const_{tot} \quad (4.6)$$

This method does not depend on the input signal amplitude of the AWG, that has just to be higher than the threshold level that one has to measure. The calibration parameters measured for all the ToT output channels are shown in figure 4.16 and 4.17

Since also  $V_T$  can be evaluated from 4.4 and 4.5, this method allows also for the measurement of the hysteresis (see figure 4.18):

$$hysteresis = V_L - V_T = \frac{ToT1 - ToT2}{(1/Slope1) - (1/Slope2)} \quad (4.7)$$

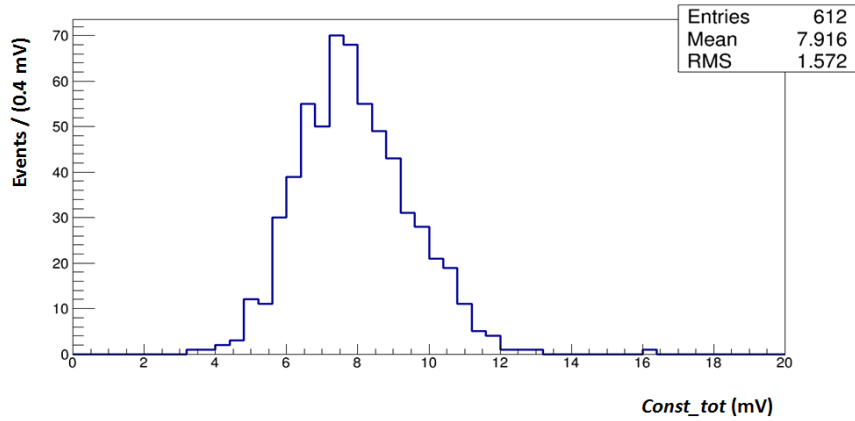


Figure 4.16: Distribution of  $Const\_tot$  parameter for the DAC calibration of the ToT board.

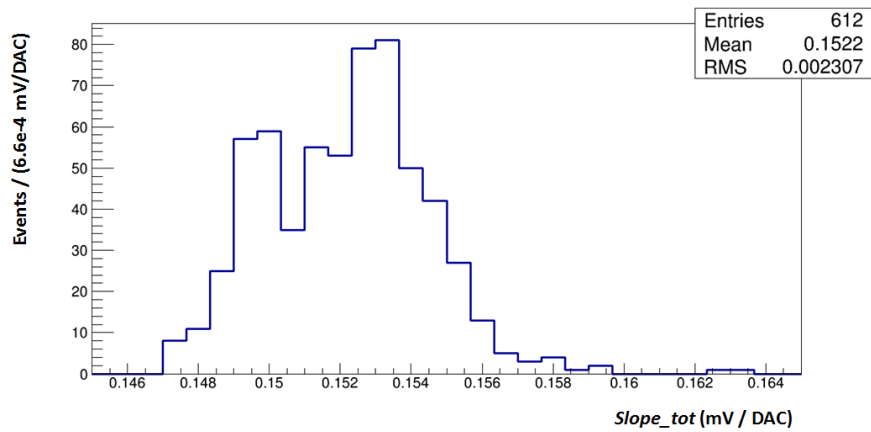


Figure 4.17: Distribution of  $Slope\_tot$  parameter for the DAC calibration of the ToT board.

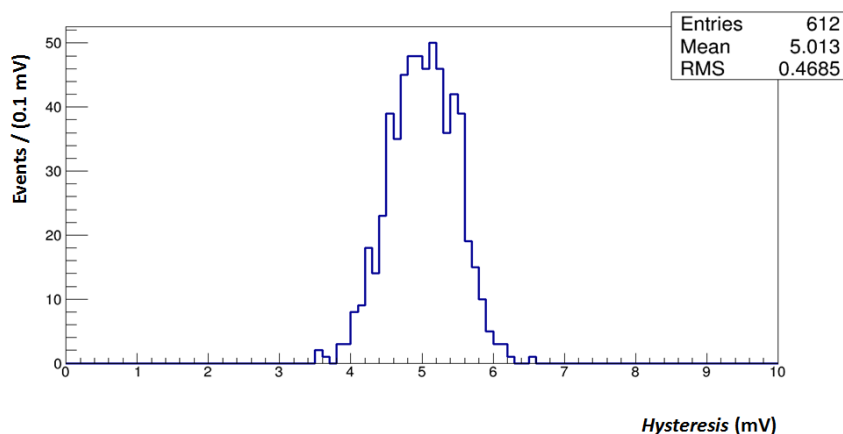


Figure 4.18: Distribution of hysteresis evaluated with eq. 4.7.

This hysteresis measurement procedure has been used by all the detectors that have the ToT boards in the front-end electronics (e.g. LAV). It has been very useful because it led to the discovery of a mistake in the design of the comparatore inside the board. The error caused the hysteresis to be negative (trailing threshold higher than leading one) and generated an oscillating and unstable LVDS output when the input signal was near the threshold. This anomalous behaviour has been demonstrated using a "square" signal (see figure 4.19) generated with the AWG. The signal "square" is made up of very fast rising and falling time and two flat parts whose amplitude difference was named  $D$ . The amplitude of the first one is called  $A$  ( $\sim 150$  mV in our setup). The widths of the constant parts ( $W \sim 14$  ns) are equal. The sinusoidal ambiental noise also has been evaluated: it comes on top of the signal. The peak-to-peak noise value is called  $N$  and is smaller than 5 mV, the nominal hysteresis value. Finally it is important to stress that the two threshold levels,  $V_L$  for leading and  $V_T$  for trailing, differ because of the hysteresis  $H$ . Once the ToT board has been calibrated, it is possible to set the  $V_L$  level equal to  $A - (N/2)$ . Measuring the ToT as a function of the  $D$  parameter, a discontinuity occurs when the  $D = H$ . Figure 4.20 shows this behaviour for a single channel with the correct hysteresis. Then it is possible to fix this value of  $D$  as working point for the input signal and perform a scan in the threshold variable. Figure 4.21 describes the ToT as a function of the threshold in this configuration for a channel with the corrected design of hysteresis and for another channel with the negative

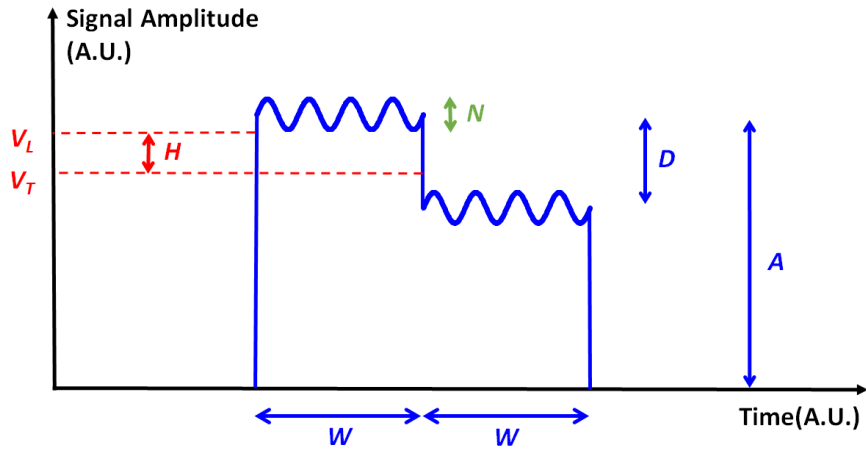


Figure 4.19: Signal generated with the AWG and used to test the behaviour of the channels of ToT board. The signal "square" is made up of very fast rising and falling time and two flat parts whose amplitude difference is  $D$ . The amplitude of the first one is  $A$  ( $\sim 150$  mV in our setup). The widths of the constant parts ( $W \sim 14$  ns) are equal. A sinusoidal noise comes on top of the signal with a peak-to-peak value equals  $N$ . The two levels threshold (leading  $V_L$  and trailing  $V_T$ ) differs because of the hysteresis ( $H$ ).

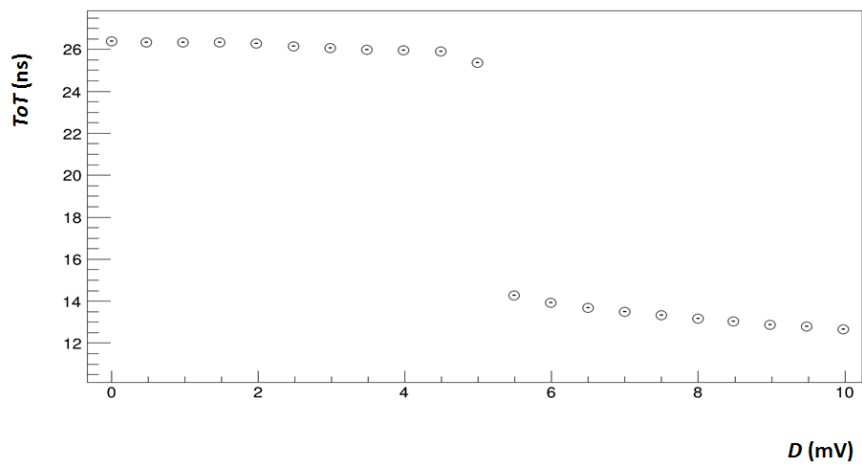


Figure 4.20: ToT as a function of the  $D$  parameter measured with the ToT board for the input signal shown in figure 4.19.

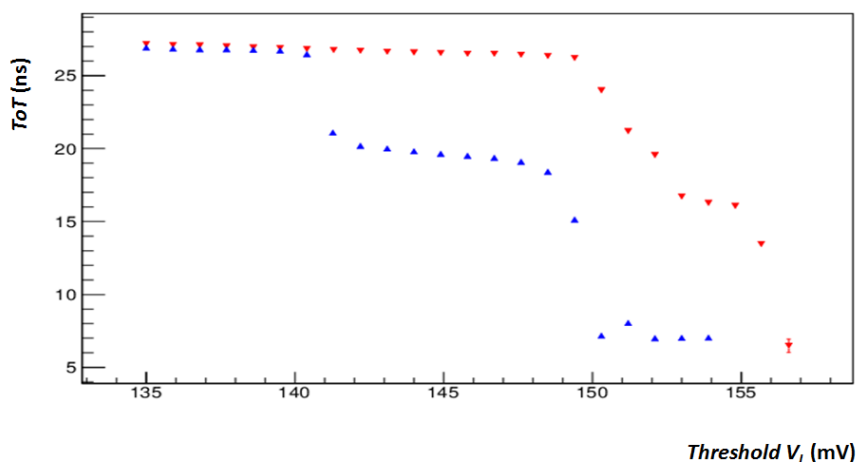


Figure 4.21: ToT as a function of the threshold for a channel with the corrected design of hysteresis (red curve) and for another channel with the negative hysteresis (blue curve).

hysteresis. In the correct design (red curve) the ToT starts to decrease when the threshold approaches the maximum signal amplitude (e.g.  $A$ ); the flat part in the decrease region corresponds to the points in which  $(A - D) < V_L < A$ . Concerning the wrong design (blue curve), the ToT starts to decrease before reaching the  $A$  value; this causes a bad estimation of the ToT and so a worse time resolution of the detector (see section 5.2). Thus after this study, all the comparators have been modified in order to satisfy the requests of each detector.

### 4.3 Validation of the calibration procedure

Once the detector with the complete front end electronics (CHANTI-FE + ToT + TEL62 boards) has been installed, a validation of the whole calibration procedure was performed by means of a threshold scan done for each SiPM of the CHANTI system. Measuring the temperature with the Pt-100 + CHANTI-FE system, the working point (e.g. the bias voltage applied with the CHANTI-FE) of all the SiPMs of the six stations was fixed in order to have the same gain of the measurement done in Naples laboratory to characterize the SiPM response at  $25^\circ$  (see section 3.3.1). Then, in absence of the beam, it was possible to count the dark rate at different values of the threshold set by the ToT board.

It was found that the SiPM dark rate scales down by roughly one order of mag-

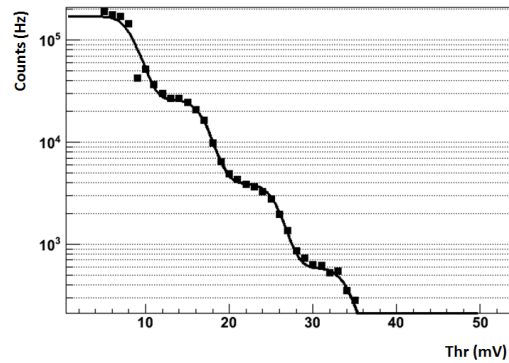


Figure 4.22: A typical threshold scan curve. The distance between two consecutive inflection points measures the single photoelectron amplitude. For this particular channel it is found to be about 9 mV.

amplitude as the threshold is raised of an amount equivalent to one photoelectron amplitude. Fitting the dark rate - threshold curve with a step function it is possible to determine the amplitude (in mV) of the single photoelectron peak for each channel (see figure 4.22). The distribution of the amplitude of the single photoelectron signal for all the channels is shown in figure 4.23. The value of  $\sim 9$  mV is in full agreement with what was observed previously in Naples laboratory.

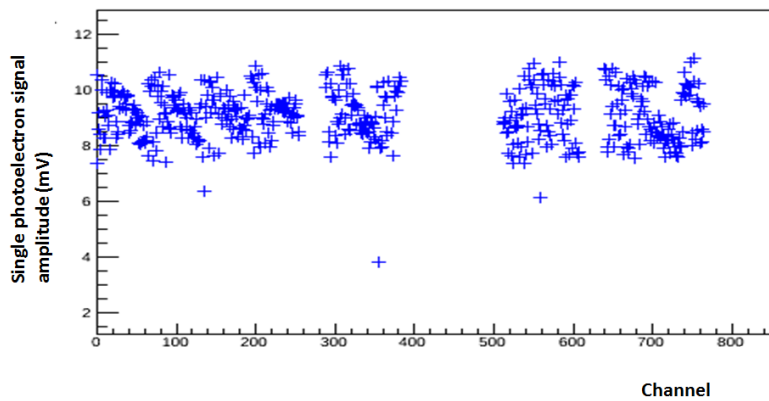


Figure 4.23: Amplitude of the single photoelectron signal obtained from the threshold scan of dark rate measurement for all the SiPM. The value of  $\sim 9$  mV is in full agreement with what was observed previously in Naples laboratory.

## 4.4 Simulation of SiPM signal

In order to reproduce the behaviour of the CHANTI signal a simulation tool has been developed. This digitization tool is still under development and it will use the data collected during the 2015 to tune the parameters in order to obtain a good agreement between data and MC; then it will be included in the official framework NA62MC, a software that simulates the full experimental apparatus based on Geant4 toolkit.

The whole simulation tool can be divided in the following steps.

- The first part consists in a complete simulation of a CHANTI scintillator bar using the Geant4 toolkit. When a particle hits the bar a certain number of photons, proportional to the energy release of the particle, are generated in the hitting points. Then Geant4 "tracks" them, in particular the ones that are captured by the WLS fiber and reach the SiPM surface located at one side of the fiber. A simulated event in which a muon hit the CHANTI bar is shown in figure 4.24 (left). The SiPM surface is simulated as a matrix of elementary microcells representing its Geiger-mode avalanche photodiodes (APDs) as shown in figure 4.24 (right).
- The output of the Geant4 consists in the evaluation of the number of photons  $N_{ph}$  that reach the SiPM, their arrival time  $T_i$  and the hit cells  $C_i$ .
- For each photon that hits the SiPM surface, a single photoelectron signal is simulated at time  $T_i$  including the afterpulse (AP) effect and the recovery time of each microcell.
- In the real device all the microcells are connected in parallel such that the output of the SiPM is the sum of the output of each cell hit by a photon. So also in the simulation the sum of photoelectron signals is computed, including the frequency bandwidth effect of the CHANTI-FE. Thus the output SiPM signal is simulated, from which one is able to evaluate ToT

Concerning Geant4 simulation, it includes all optical surfaces of the CHANTI bar like the  $\text{TiO}_2$  coating, the aluminium mirrored end of the fiber and the interfaces between the different materials (e.g. optical glue and scintillator, the fiber clad and core). The simulation has been tested checking the correct behaviour of the

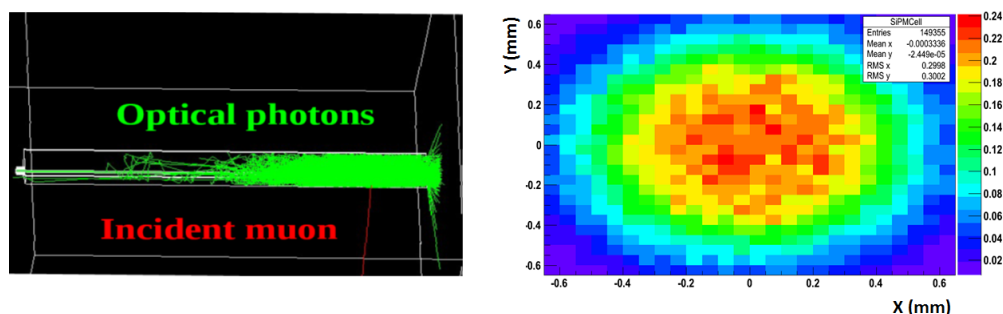


Figure 4.24: Left: Geant4 simulated event in which a muon (red) hits the scintillator bar; some photons (green) are captured by the fiber and reach the SiPM located on the left side of the fiber. Right: SiPM cell occupancy for 2000 events in which a muon hits the scintillator bar; the histogram is normalized to the number of events analyzed.

optical surfaces [67]. The effect of PDE (as quoted by the manufacturer), as a function of the photon wavelength, has been included in order to select the only photons that contribute to the final SiPM signal.

In order to simulate a single photoelectron signal, its characterization from real data is needed. In particular we analyzed the waveform at the output signal of the SiPM put inside a dark chamber at a fixed temperature ( $25^\circ$ ) (e.g. dark-noise signals). The front-end readout was made up of a prototype of the final CHANTI-FE and an oscilloscope. The waveform was acquired only if its amplitude exceeded 3.5 mV. The main parameters needed are the signal amplitude and the characteristic time of the exponential decay that describes the falling part of the signal. Concerning the amplitude, its distribution has a peak structure due to the different number of photoelectron that can generate the signal (see figure 4.25). So the amplitude of the single photoelectron signal can be evaluated from distribution in figure 4.25, considering a gaussian fit performed on the first peak of the distribution.

Then, in order to select signal due to single photoelectron, a cut on the signal amplitude (between 5 mV and 15 mV) has been applied. On this sample of waveforms an exponential fit has been performed (see figure 4.26):

$$Amplitude = AmplSPE \cdot \exp^{-(time - TimeOffset)/\tau} + Const \quad (4.8)$$

The distribution of the  $\tau$  parameter obtained from this fit is shown in figure 4.27. A simulated single photoelectron signal can be defined with the following structure

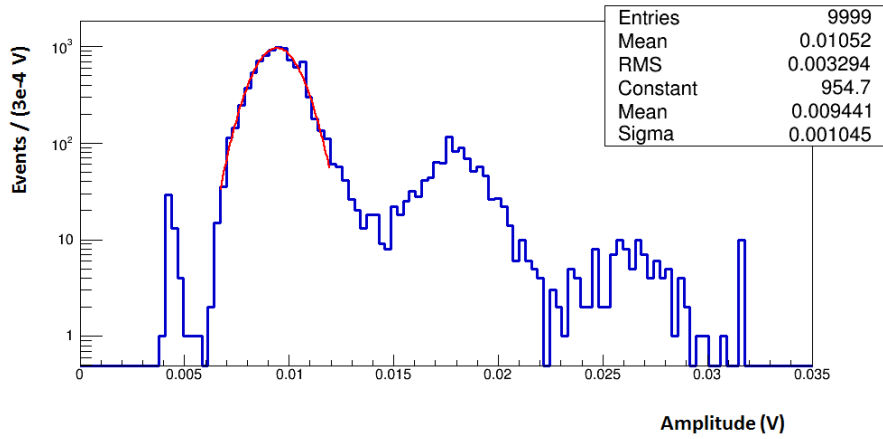


Figure 4.25: Distribution of the amplitude of the signals due to SiPM dark noise. The peak higher than 5 mV are due respectively to one, two and three photoelectrons signal. The peak below 5 mV is due to pedestal.

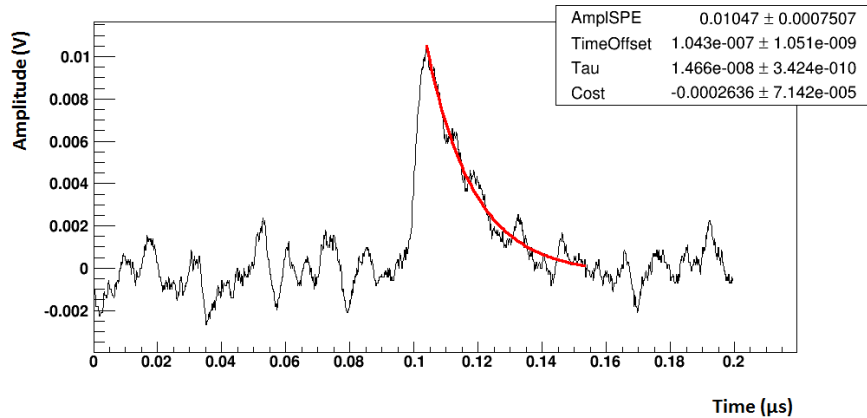


Figure 4.26: Typical single photoelectron waveform collected. A fit with an exponential function has been performed on the falling part of the waveform. The baseline is affected by the residual radio-frequency noise survived to the frequency cut of the CHANTI-FE.

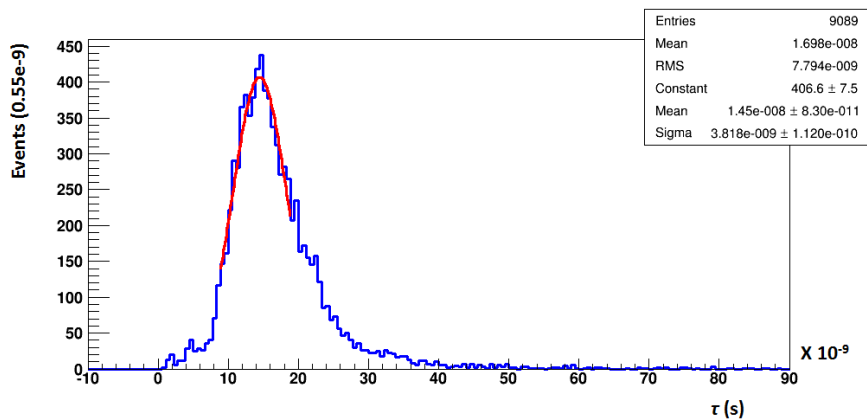


Figure 4.27: Distribution of the  $\tau$  measured fitting the falling part of the collected single photoelectron signal using in eq. 4.8.

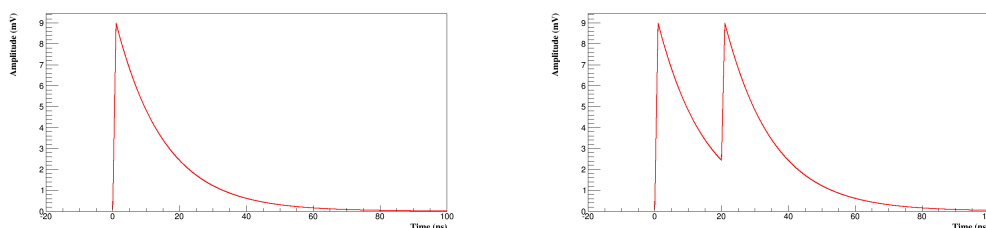


Figure 4.28: Left: single photoelectron signal simulated. Right: signal simulated due to two photons hitting the same microcell of the SiPM

(see left figure 4.28):

- a linear rising part, with a rise time of 1 ns [68], starting from 0 (at time  $T_i$ ) up to its amplitude  $A_i$ ; the amplitude  $A_i$  of this signal is randomly generated from a gaussian distribution, with mean and sigma parameters equals to the gaussian function obtained from the fit on the amplitude distribution of the waveform collected shown in figure 4.25;
- a falling part made up of an exponential decay with a characteristic time  $\bar{\tau}$  (evaluated as the mean parameter of the gaussian function that is used to fit the distribution in figure 4.27).

If another photon hits the same single microcell within its recovery time (that is described by the exponential decay with characteristic time  $\bar{\tau}$ ), then the amplitude

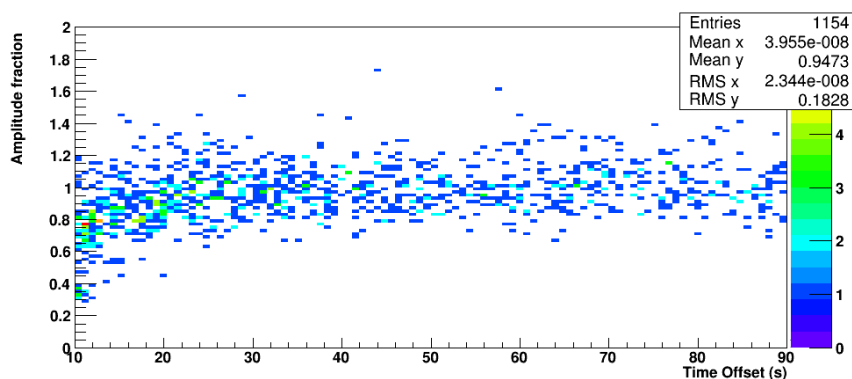


Figure 4.29: Ratio of the amplitude of AP over the amplitude of the original pulse as a function of the time difference of the AP and the original pulse.

of the signal of this photon is reduced in order to have a maximum amplitude of the sum of the signals due to the two photons equals  $A_i$  (see right figure 4.28) . Also the afterpulse (AP) effect has been simulated: during an avalanche of the APD, charge carriers can be trapped in the silicon lattice and be released after a characteristic time; this can cause a delayed second avalanche breakdown faking a photon signal. In order to evaluate this effect, the presence of AP has been identified looking at the waveform collected. In particular an algorithm that searches for a second pulse (after the triggering one) has been implemented. Obviously this algorithm detects secondary pulses due to both AP mechanism and accidental coincidence. The ratio of the amplitude of the second pulse over the amplitude of the original pulse as a function of the time difference of the second pulse and the original pulse has been evaluated (see figure 4.29). Observing the time distribution of the second pulse (see figure 4.30, that is the projection along time axis of the plot in figure 4.29), it is possible to distinguish two regions: in the region of low time distance between the two pulses, both afterpulses and accidental coincidence are present, while for higher time distance just the accidental coincidences occur. A fit on this distribution using an exponential function plus a constant has been performed ( $x_0 = 10\text{ns}$ ):

$$y = p0 \cdot \exp^{-(x-x_0)/p2} + p3 \quad (4.9)$$

The probability of an accidental coincidences can be evaluated using the constant parameter of the fit. Taking into account the number of single photoelectron

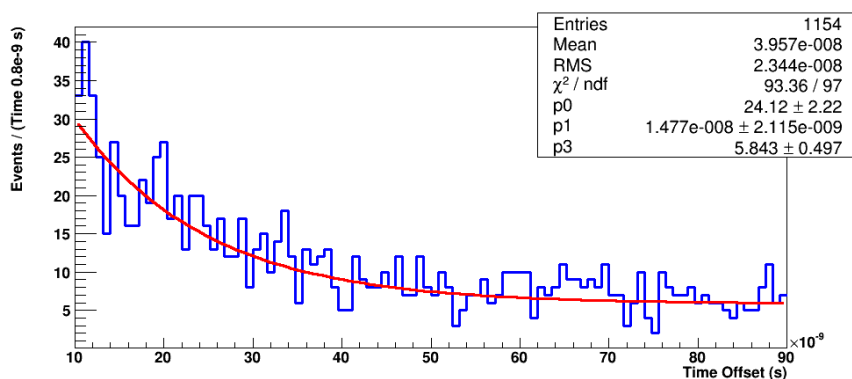


Figure 4.30: Distribution of the time offset of the AP peak respect to the primary signal pulse.

signals analyzed, the result is consistent with a dark rate of the order of  $\sim 800$  KHz, that is a typical value provided by Hamamatsu for this kind of device. Then the probability of AP can be evaluated using the number of entries of the histogram after subtracting the number of entries due to accidental coincidence. The result is  $(5.9 \pm 0.2)\%$ . Each time a photon hits a microcell, an AP is generated with this probability. The starting time of the afterpulse is randomly generated according to the exponential function which fits the measured time distribution of the AP. The amplitude of the AP is correlated with the time distance of the AP itself respect to the original pulse. So, once the time at which the AP occurs has been evaluated, it is possible to compute the amplitude fraction of AP respect to the primary pulse from the profile histogram <sup>1</sup>(see figure 4.31) of the plot in figure 4.29. A fit to this profile function with an exponential function has been performed. Thus the amplitude fraction of afterpulse is randomly generated from a gaussian distribution with a mean equal to the value of the fit function at which the AP starts and a sigma equal to the standard deviation of the amplitude fraction distribution inside the bin containing the AP time.

The sum  $S$  of the signals of all photons is evaluated. Then a Fourier Transform is applied to  $S$  (using the FFTW toolkit [69]). A low pass filter with a cut-off frequency of 80 MHz has been implemented in order to simulate the bandwidth of

<sup>1</sup>Profile histograms are used to display the mean value of Y (the amplitude fraction in our case) and its uncertainty for each bin in X (time distance between AP and primary pulse). The displayed uncertainty is the standard deviation of the distribution in the X bin.

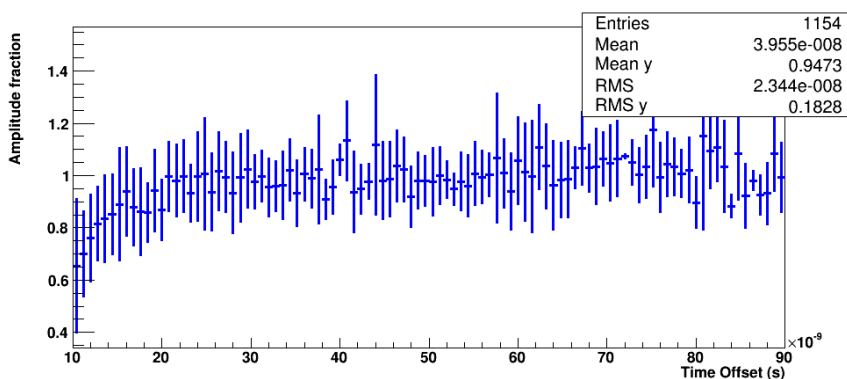


Figure 4.31: Profile histogram of the plot in figure 4.29 showing the amplitude fraction of AP respect to the original pulse as a function of the time offset of the AP respect the original pulse.

the CHANTI-FE board. The filter is applied to  $S$  and then an Inverse Fourier Transform is performed in order to obtain the waveform in the time domain. Finally all the main features of signal like ToT can be evaluated.

In order to validate the simulation procedure, a comparison between the data collected during the bars test (with a telescope of two small scintillation counters as trigger, see section 3.3.3) and the simulation of the response of a bar has been performed. Thanks to the Geant4 toolkit, muons are simulated according to the angular distribution obtained in the telescope used in the experimental setup. Figure 4.32 shows the maximum amplitude of the signal as a function of number of photoelectrons collected by the SiPM for this kind of simulated event. The number photoelectrons is given by the ratio of the charge of the output simulated signal and the one of the single photoelectron signal. Figure 4.33 shows the analogue plot for real data. It is important to stress that the slope of linear fit performed on the previous distributions is not equal to  $9 \text{ mV}/N_{\text{ph}}$  as one can expect because of the amplitude of the single photoelectron signal. The value obtained, both in measured and simulated data, is lower and this is due to the spread that characterized the arrival times of the photons on the SiPM surface.

Figure 4.34 shows the efficiency of signal detection as a function of the threshold applied for signals that pass the 80 mV threshold both for simulation and data. Finally figure 4.35, 4.36 and 4.37 show the distribution of the ToT as a function of the number of photoelectron collected for different values of the threshold applied

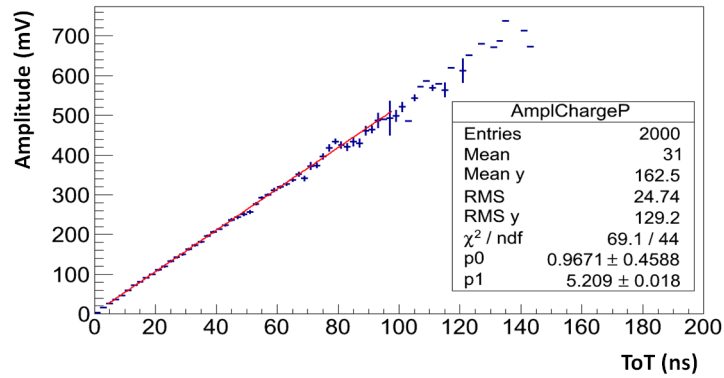


Figure 4.32: Maximum amplitude of the signal as a function of number of photoelectron collected by the SiPM obtained with the whole simulation of a CHANTI bar hit by muons and the digitization of the signal.

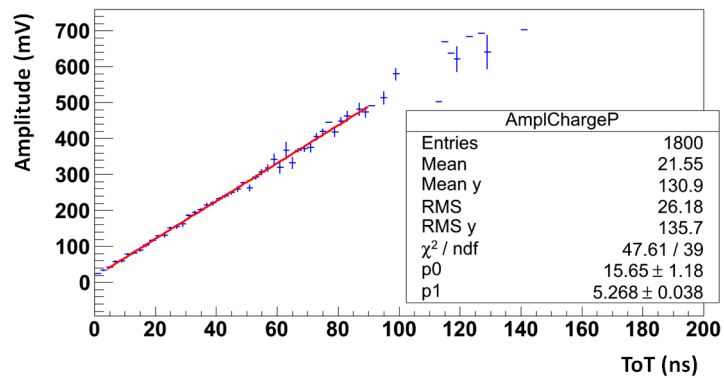


Figure 4.33: Maximum amplitude of the signal as a function of number of photoelectron collected by the SiPM obtained with real data in the experimental setup with a telescope of two small scintillation counters as trigger, see section 3.3.3.

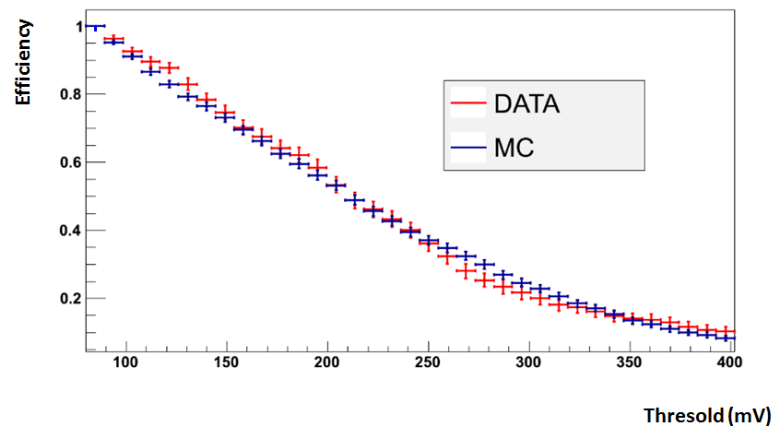


Figure 4.34: Efficiency of signal detection as a function of the threshold applied for signals that passes the 80 mV threshold both for simulation and data.

to the signal.

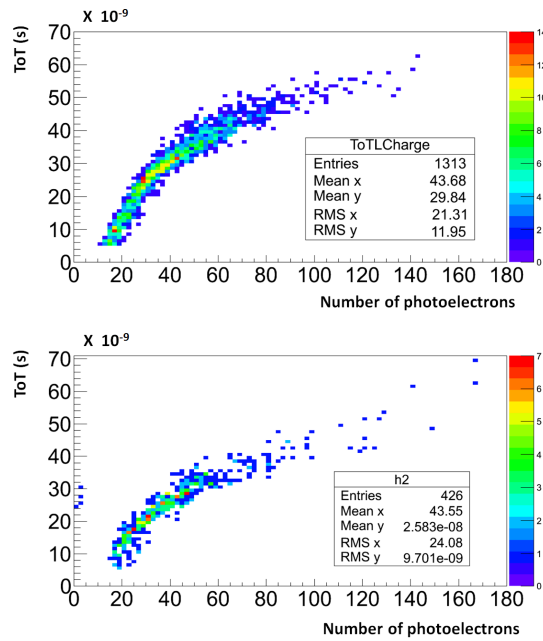


Figure 4.35: Distribution of the ToT as a function of the number of photoelectron collected for a threshold equals 80 mV for MC (up) and data (bottom).

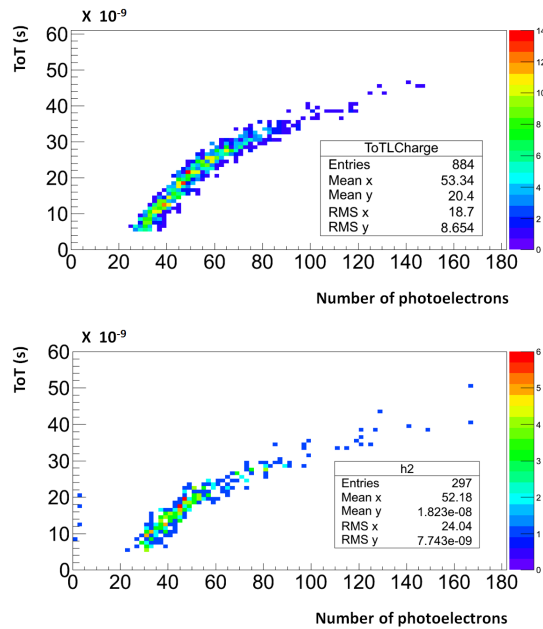


Figure 4.36: Distribution of the ToT as a function of the number of photoelectron collected for a threshold equals 150 mV for MC (up) and data (bottom).

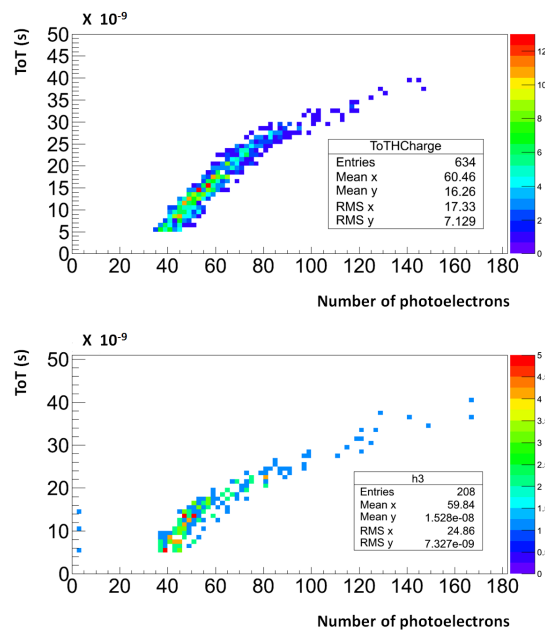


Figure 4.37: Distribution of the ToT as a function of the number of photoelectron collected for a threshold equals 200 mV for MC (up) and data (bottom).

# Chapter 5

## Detector performance

The performance of the detector has been thoroughly tested on the final experimental setup during the run of NA62 in 2015 (but also on several prototypes, both using cosmic rays in Naples laboratory and tests beam). Tests have concentrated on the main figures of merit for the detector, namely its time resolution and its efficiency. But also the accidental veto introduced by the detector and its spatial resolution have been evaluated.

### 5.1 CHANTI during the NA62 run in 2015

In the course of 2014 the construction of CHANTI was completed. Figure 5.1 shows the first five CHANTI stations assembled in their vacuum vessel. The sixth stays in a vacuum chamber extension at about one meter from the fifth. The whole detector, consisting of six separate stations for a total of 288 physical channels and 576 electronic channels, was installed at CERN on the NA62 beam line (see figure 5.2). The experiment started data taking with a run carried out between October and December 2014 (the so-called Pilot Run). The main purpose of the run was the "commissioning" of the NA62 apparatus. In 2015 the first physics run started with the main purpose of evaluating detector performances and starting the data analysis.

Data were collected in two different conditions:

- with a beam of hadrons,



Figure 5.1: The first five CHANTI stations assembled in their vacuum vessel.

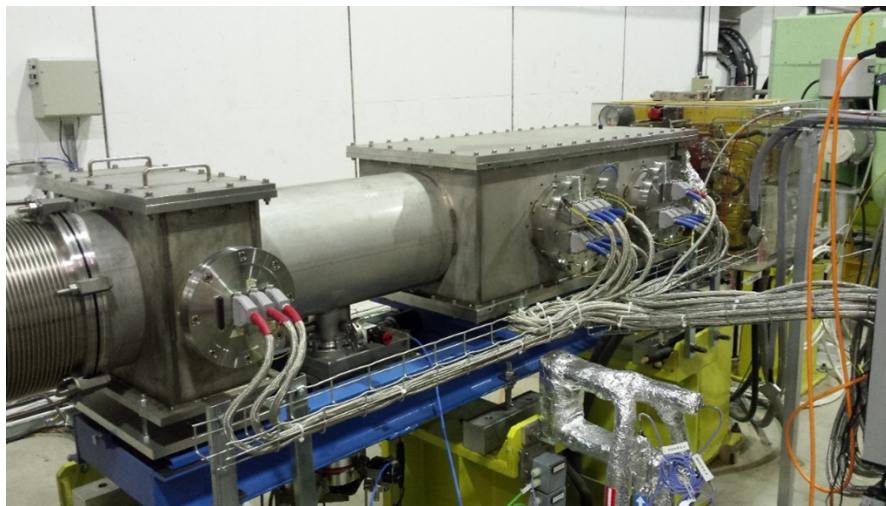


Figure 5.2: The two vessels containing the six CHANTI stations, installed on the K12 beam line at CERN. The flange and the cabling that carry out SiPM signals are also visible.

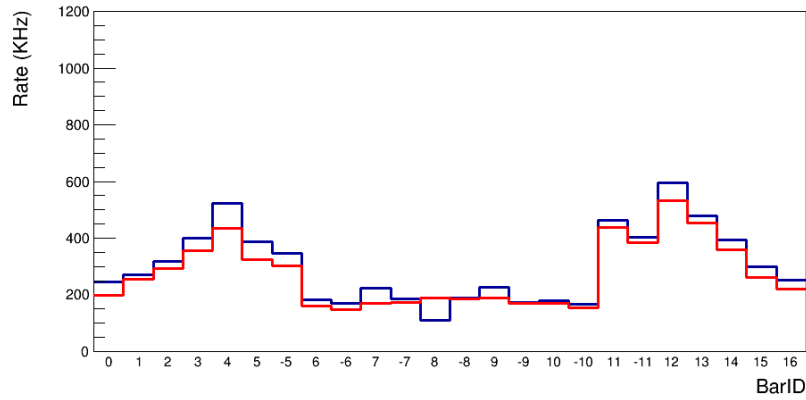


Figure 5.3: Rate of the bars of one layer with a 40% intensity beam with respect to the nominal one. In blu the rate from real data, in red the rate obtained via simulation scaling linearly with beam intensity.

- with a beam of muons.

The second condition corresponds to the situation of beam but with the presence of a "filter" (the TAX along the beam line were closed) according to which the particles that reach the detector are essentially muons. Using these two different configurations, the performance of the CHANTI has been evaluated. The rate of particle hitting CHANTI was measured and compared with the simulation performed in section 3.4. The comparison is shown in figure 5.3. In this case the beam intensity was 40% of the nominal one, so the simulated rate has been scaled linearly by a factor 0.4 in order to take into account this effect. The energy threshold for simulated data was chosen to match the threshold in mV applied to real signal. The comparison shows a reasonable agreement, even if the observed rate is systematically higher than expected by 10-20%. This may be due to the non perfect simulation of the beam interaction with the material before CHANTI.

## 5.2 Time resolution

Regarding the time resolution, the basic ingredient to reach the needed performance is the ability to perform the appropriate time walk correction<sup>1</sup>, without measuring the integrated signal charge. This is done using two features of the front-end electronics, namely the possibility to measure the time at which the signal crosses two different thresholds (so called Low and High threshold respectively), and the time it stays above each of them. Signals passing both the low and high thresholds allow the determination of the time  $t$  a particle passes through the detector; in fact, in linear approximation,

$$t = t_L - \delta t = t_L - V_L \frac{t_H - t_L}{V_H - V_L} \quad (5.1)$$

where  $V_H$  and  $V_L$  are the high and low thresholds and  $t_H$  and  $t_L$  are the "leading times" corresponding to the high and the low thresholds (see figure 5.4).

The  $\delta t$  correction is correlated to  $ToT$  as can be seen from the distribution in

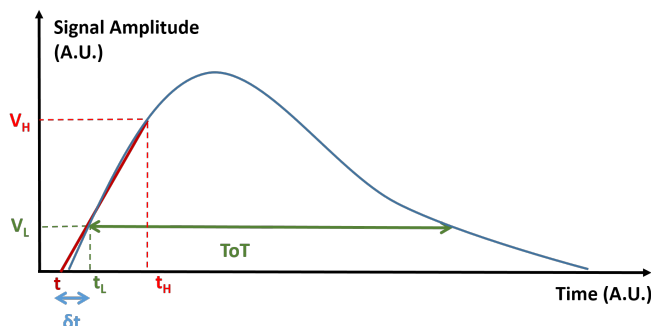


Figure 5.4: Time-walk correction ( $\delta t$ ) in linear approximation (eq. 5.1).

figure 5.5. In order to apply the time-walk correction also to the signals which only cross the low threshold, the distribution in figure 5.5 has been fitted and the  $\delta t$  correction has been parametrized as a logarithmic function of the  $ToT$ . Tests on CHANTI prototypes have been performed during the test beam called "Technical Run" of NA62 in 2012. These measurements, done in different conditions, have all pointed towards a single hit time resolution of the CHANTI (after time

<sup>1</sup>The time the analog signal from CHANTI-FE crosses a threshold depends on the amplitude of the signal itself because the rise time of the signal is constant. This is the time walk effect and it has to be corrected in order to remove this dependence.

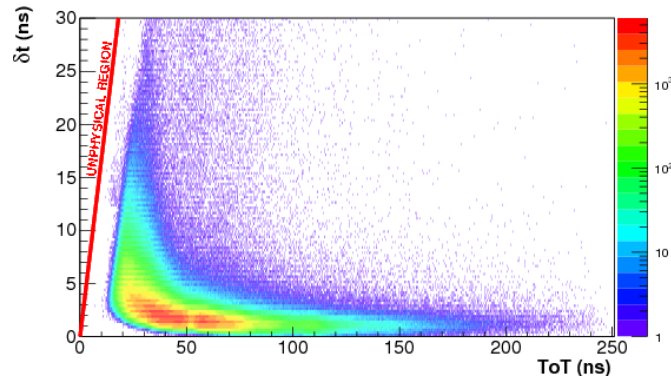


Figure 5.5: Time walk correction vs  $ToT$  for events passing both thresholds. The unphysical region, at the left of the red line, is defined by the condition  $t_H - t_L > ToT$ .

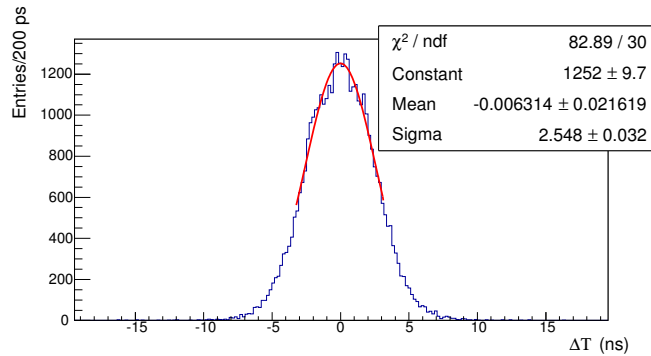


Figure 5.6: Difference between the "leading times" of signals from two adjacent bars. The resolution of the detector can be evaluated from the ratio of the Sigma parameter of the gaussian fit over the square root of 2.

walk corrections are applied) of order 1 ns (cfr.  $1.03 \pm 0.01$  in [70]). Using part of the collected data in 2015, the time resolution of the detector was re-measured by the method of the difference between the "leading times" of signals from bars produced by the same track. In order to do this, just the difference between adjacent bars (belonging to the same layer and positioned next to each other) has been performed: this avoids any positional effect that has to be taken into account if bars belonging to different layers are considered.

A plot of this difference, not corrected for time-walk and  $t_0$  time difference between channels (e.g due to different cables lengths for example), is shown in figure 5.6. The first correction was parameterized according to the  $ToT$  with the method

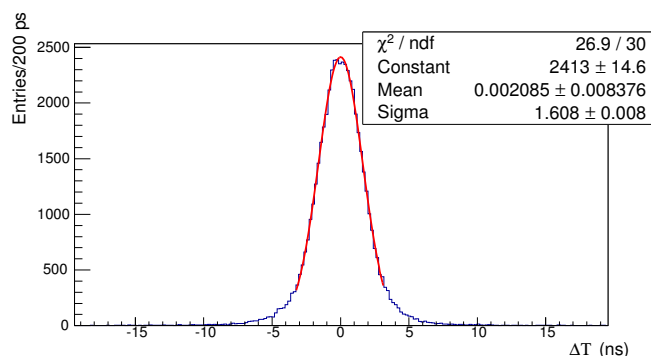


Figure 5.7: Difference between the "leading times" of signals from two adjacent bars after time walk and reference detector time corrections. The resolution of the detector can be evaluated from the ratio of the Sigma parameter of the gaussian fit over the square root of 2.

illustrated before (e.g. linear extrapolation for signals passing both thresholds and parametrization with the ToT for signals passing only the low threshold); the second (time offset between channels) was estimated by the difference in the transit time of particles of the same event recorded by each CHANTI channel and by the KTAG; then, for each channel, a gaussian fit has been performed on the distribution of the difference in the transit time and the mean value of the gaussian function has been subtracted to each channel. Figure 5.7 shows the corrected distribution, from which one gets a time resolution of 1.14 ns, in agreement with the result of tests on prototypes.

A different approach has also been used in order to evaluate the time resolution of the detector. The difference of the time recorded by each CHANTI channel and the one recorded by the KTAG in the same event has been evaluated (after time walk and  $t_0$  corrections) and a gaussian fit has been performed on the core of this distribution (see figure 5.8). Taking into account the time resolution of the KTAG ( $\sim 100$  ps), the single bar time resolution is 1.38 ns: in this calculation the time resolution gets worse with respect to the previous configuration because points hit by particle crossing both X and Y layers of one CHANTI station have different distance respect to the SiPM. However time resolution still satisfies CHANTI requirements. An algorithm of bars clusterization has been implemented in order to improve time resolution and define the basic CHANTI elements that will be used during the analysis. First a view-cluster of bars is defined as a set of adjacent bars

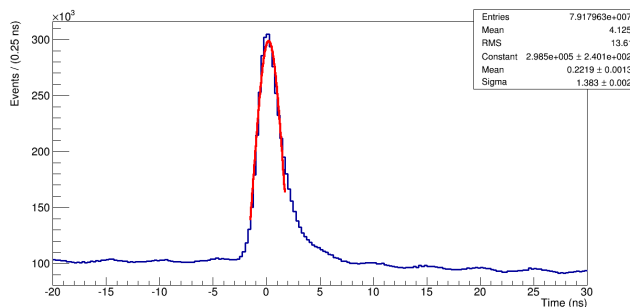


Figure 5.8: Difference between time recorded by each CHANTI bar and the KTAG.

belonging to the same layer (X or Y) of the same station and fired at the same time. Since the  $ToT$  has a logarithmic dependence from the charge generated by the particle that passes through the bar, a pseudo-charge  $Q_p$  may be associated to each signal, defined as  $Q_p = \exp(ToT/ToT_0)$ , with  $ToT_0 \equiv 38$  ns. This formula has been determined by the MC program that simulates the CHANTI output signal (see section 4.4). The X (or Y) position and the time of the cluster is evaluated doing a charge weighted average of the nominal positions and times (after time walk and  $t_0$  corrections) of the bars. If a time and X-Y match is found between view-cluster belonging to different layers of the same station, then a CHANTI candidate, made up the bars of these two view-clusters, is created with the proper time (average of the two cluster times) and X-Y coordinates. If there are no time or X-Y matches between the found view-clusters, then the CHANTI candidate is defined with only the cluster of one layer (in this case just one coordinate, X or Y, is well defined). The difference of the time recorded by each CHANTI candidate and the one recorded by the KTAG in the same event has been evaluated and a gaussian fit has been performed on the core of this distribution (see figure 5.9). Taking into account the time resolution of the KTAG ( $\sim 100$  ps), the CHANTI candidate time resolution is 930 ps.

### 5.3 Detection efficiency

Regarding the efficiency, the first measurement was carried out in Naples laboratory using a prototype made of 5 bars. A 4-fold coincidence of small scintillator counters selected vertical muons crossing the three central bars of the prototype.

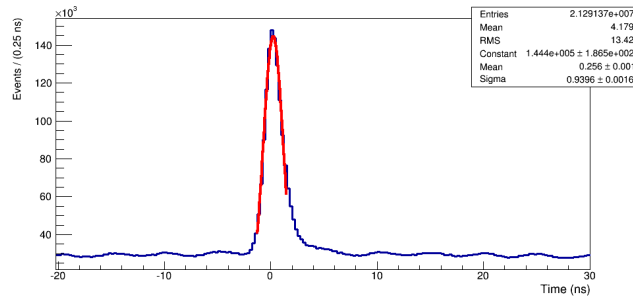


Figure 5.9: Difference between time recorded by each CHANTI candidate and the KTAG.

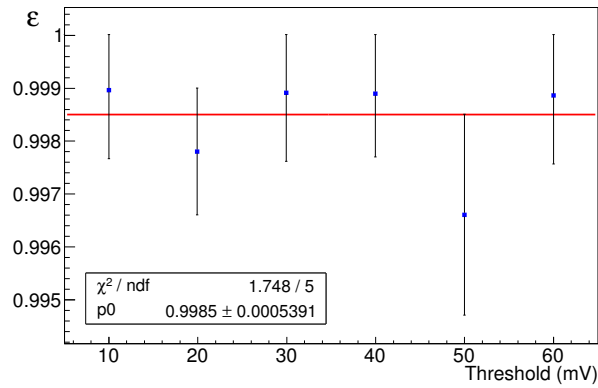


Figure 5.10: Layer efficiency, measured with a prototype made of 5 bars, as a function of threshold.

The signals from the five bars were processed by the CHANTI front-end card and sent to the "ToT" card which converted the analog input signals into LVDS digital signals. The LVDS signals were then processed by a TDC VME module (equipped with the same TDC of the TEL62 card) whose outputs (leading and trailing times) were acquired by a PC. A good event was defined by at least one bar fired giving an analog signal over a fixed threshold and a corresponding full LVDS signal, i.e. a signal with a leading and trailing times, in the time window of the trigger. Data were collected for 6 monospaced different thresholds ranging from 10 to 60 mV. Events were collected at each threshold. Figure 5.10 shows the efficiency as a function of the threshold. As can be seen the efficiency is the same, within error, for all thresholds and its mean value is  $0.9986 \pm 0.0005$ . Anyway the two lower thresholds, which correspond to a signal of about  $1 \div 2$  pe, are not

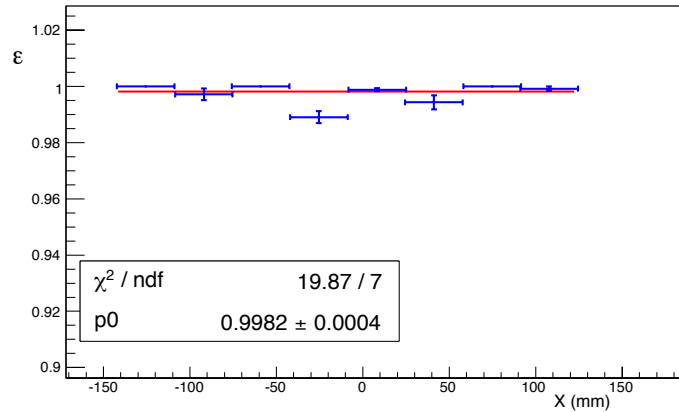


Figure 5.11: Single layer efficiency measured on data.

usable in practice in the final experimental setup; indeed, given the SiPM thermal noise, they would generate a single channel accidental activity in the CHANTI of the order of (or even above) the physical signal rate at full intensity.

During the NA62 run in 2015, using muon beam condition, the CHANTI efficiency was studied thanks to the tracks of passing particles ("muons") parallel to the beam direction. The efficiency was studied for each station and for each view, both for coordinates  $x$  (view with vertical bars) and  $y$  (view with horizontal bars) separately and as a function of the  $xy$  position. Let us consider, for example, the study of efficiency as a function of  $x$ . A "muon" is defined as an event that gives at least one hit in two vertical coupled bars of a station and in the corresponding bars of four other stations; the sixth station is defined efficient if it presents for the same event at least one hit in the corresponding coupled bars or in one of the two immediately nearby bars. Efficiency is defined as the ratio between the number of times the station was efficient and the total number of selected events. Figure 5.11 shows the efficiency of the  $X$  layer of the first station as a function of the position of the vertical bars. The single layer efficiency, defined as above, resulted  $> 0.99$ . It is worth noting that a layer efficiency  $\geq 0.99$  ensures that the CHANTI inefficiency for detecting a charged particle, passing through both layers of a station, is less than 0.1%.

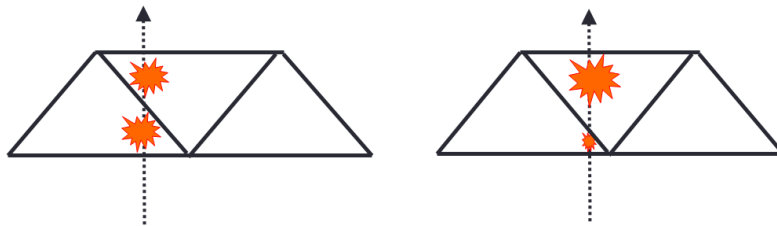


Figure 5.12: Because of the triangular section of the bars, for muons crossing perpendicularly the CHANTI an anticorrelation exists between the energy release in two coupled bars. This leads to an anticorrelation between the amplitudes, and then between the  $ToT$ , of the signals recorded in the two coupled bars.

## 5.4 Spatial resolution

A minor issue of the CHANTI is the capability to perform some particle tracking in order to validate our inelastic event simulation and to study the beam halo. So also the spatial resolution of the detector has been evaluated.

During muon run, muons proceed in a direction parallel to the beam and cross the CHANTI stations perpendicularly to their plane frames. Due to the triangular section of the bars, for these particles an anticorrelation exists between the amplitudes, and then between the  $ToT$ , of the signals recorded in two coupled bars (see figure 5.12). The pseudo-charge  $Q_p$  can be used to determine the position where the particle impacts two coupled bars doing a charge weighted average of the nominal positions of the bars and, thus, to study the spatial resolution of the detector. In figure 5.13 it is shown, as an example, the difference between the x-coordinate (vertical bars) determined by the positions of two coupled bars of the third station and the corresponding one of the fourth station. Assuming, as it is reasonable to do, the two stations have the same spatial resolution, from that plot one obtains  $\sigma_x = 2.6$  mm. A systematic study of all stations led to the result  $\sigma_{x/y} \simeq 2.5$  mm. This has to be compared with the rms (4.9 mm) of a flat distribution with a pitch of half of a bar base.

## 5.5 Accidental veto

In order to evaluate the accidental veto introduced by the CHANTI, a sample of kaon decays with one charged particle in the final state ( $K_{2\pi}$  and  $K_{\mu 2}$ ) has been

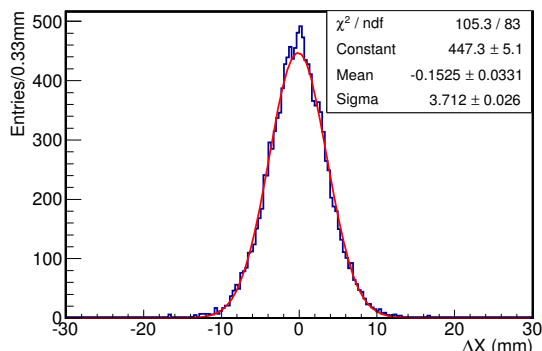


Figure 5.13: Difference between X position of two hit points on different station for tracks parallel to beam direction.

selected from data at different beam intensity. The minimum number of detector is used to select these samples: this avoids uncertainty introduced by the different conditions of some detectors in the various sets of data collected. Then, for the events identified as ( $K_{2\pi}$  or  $K_{\mu 2}$ ), the number of times CHANTI bars are fired has been evaluated. This analysis uses the NA62 Reconstruction algorithm (ver. 834) in order to handle the data collected from the detectors. The data are collected with two kinds of trigger:

1. CHOD: data recorded when there are hits in the charged hodoscope
2. CHOD and !MUV3: data recorded when there are hits in the charged hodoscope and, at the same time, nothing in the MUV3

The run used for this analysis are

- run 3810 - beam intensity at 1% of the nominal one
- run 4069 - beam intensity at 10% of the nominal one
- run 3767 - beam intensity at 40% of the nominal one

### 5.5.1 Selection of $K_{2\pi}$ sample

In order to select a  $K_{2\pi}$  sample, STRAW, LKr, CHOD, KTAG and MUV3 are used. Figure 5.14 shows the topology of a  $K_{2\pi}$  event: an initial state with a kaon,

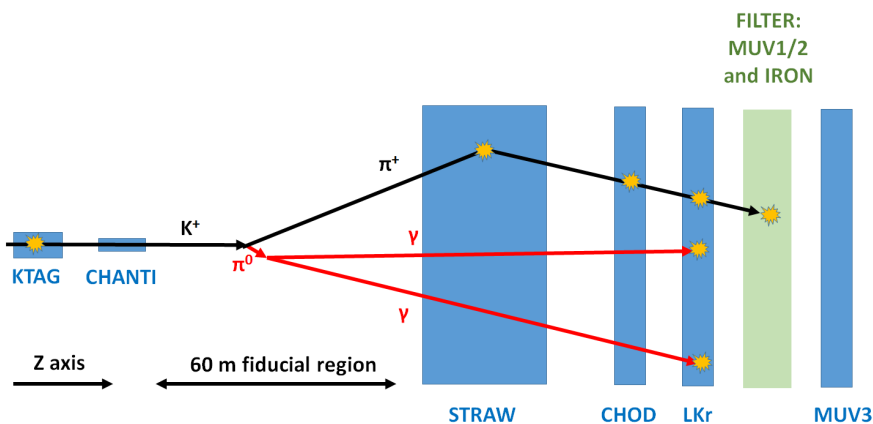


Figure 5.14: Topology of a  $K_{2\pi}$  event. The kaon, identified by the KTAG, decays inside the fiducial volume. The  $\pi^+$  is in the geometrical acceptance of STRAW, CHOD and LKr and its momentum is measured by the STRAW; finally there is a pion shower in the hadronic calorimeter (MUV1/2) or in the iron layer before MUV3. The  $\pi^0$  decays into two photons that hit the LKr.

recognized by KTAG, and a final state with a charged particle and two photons hitting the LKr. Since the data from the beam spectrometer (the GTK system) are not used, nominal beam parameters (in terms of momentum and direction of the beam particle, e.g. the kaon) have to be used in this kind of selection.

The basic requirements for the  $K_{2\pi}$  search are the following one:

- one CHOD candidate that means one charged particle in the final state that is detected by the X and Y layer of the charged hodoscope; the time of the CHOD candidate represents the reference time for all detectors
- at least one KTAG candidate, corresponding to a charged particle passing through the Cherenkov detector, that has to be recognized as a kaon and in time with the CHOD candidate. Figure 5.15 shows the time difference of the CHOD and all the kaon KTAG candidates for the run 3767: if the time difference of CHOD and KTAG is less than 1 ns ( $\sim 3\sigma$  of the gaussian function that fits the peak of the distribution), then the two candidates are considered in time. If more than one kaon KTAG candidate is in time with the CHOD one, then the closest in time to the CHOD is chosen as the effective kaon that originates the eventual  $K_{2\pi}$  decay.

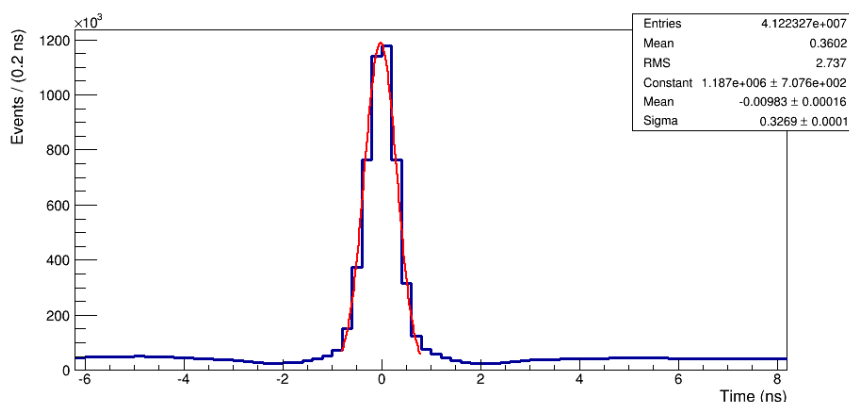


Figure 5.15: Distribution of the time difference between the CHOD candidate and all the kaon KTAG candidates for the run 3767. The gaussian function that fits the peak of the distribution has a sigma of 0.3 ns. Thus a kaon KTAG candidate is considered in time with the CHOD one if the time difference between them is less than 1 ns ( $\sim 3\sigma$ ).

Once the presence of a kaon in the initial state and a charged particle in the final state has been ensured, it is possible to search for a single track event in the STRAW with the following characteristics.

- Track has to represent a particle with a positive charge
- Track has to be in the geometrical acceptance of LKr, CHOD and MUV3
- Track has to be in time with the CHOD candidate (difference less than 15 ns) and the projection of the track on the CHOD plane must have a X and Y distance respect to the CHOD candidate less than 5 cm
- The Distance of Closest Approach (DCA) between the track and the nominal beam direction can be used in order to find the decay vertex of the charged kaon. Figure 5.16 shows the DCA between the two tracks (beam kaon and charged particle) as a function of the Z coordinate of the decay vertex for the run 3767. The decay vertex is required to be inside the fiducial volume of the NA62 experimental apparatus, that means a Z coordinate of the decay vertex between 10500 cm and 16500 cm. Moreover a cut on the DCA is applied: it has to be less than 3.6 cm, corresponding to 3 times the characteristic length of the exponential decay that describes the DCA distribution.

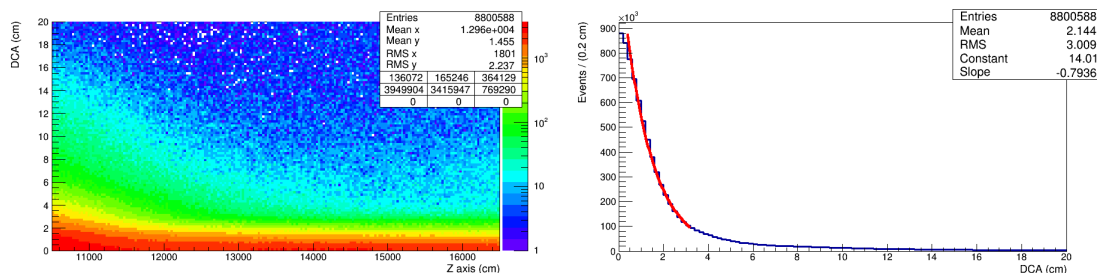


Figure 5.16: On the left the distribution DCA between the beam kaon and the charged particle as a function of the Z coordinate of the decay vertex for the run 3767 inside the fiducial volume. On the right an exponential fit has been performed on the DCA distribution; the characteristic length of the exponential decay is of the order of 1.2 cm

Only events that have just one track from STRAW satisfying all the previous requirements are considered "single track event". If  $P_K$  is the 4-momentum of the beam particle under the kaon hypothesis and  $P_{\pi^+}$  is the 4-momentum of the charged particle seen by the STRAW under the  $\pi^+$  hypothesis, it is possible to evaluate the missing mass of the process

$$m_{miss}^2 = (P_K - P_{\pi^+})^2 \quad (5.2)$$

as a function of the momentum of the charged particle in the final state (see figure 5.17 on the left). In the projection along the  $m_{miss}^2$  variable of the previous function (see figure 5.17 on the right) it is possible to distinguish:

- a peak for negative value of  $m_{miss}^2$  corresponding to  $K_{\mu 2}$  events
- a region at values  $m_{miss}^2 > 0.07 \text{ GeV}^2/c^4$  dominated by  $K^+ \rightarrow \pi^+ \pi^- \pi^+$  process.
- a peak around the value  $m_{\pi^0}^2$ , where  $m_{\pi^0}$  is the mass of the neutral pion ( $0.1349766 \pm 0.0000006 \text{ GeV}/c^2$  [71])

The latter peak is due to  $K_{2\pi}$  events that we want to select. In order to do this, also the information coming from the LKr can be used. First we search for a unique LKr candidate defined as a cluster of close cells of the LKr calorimeter fired at the same time with a well defined X-Y position. It has to be compatible in time with the CHOD and in space with the track requiring that the time difference between

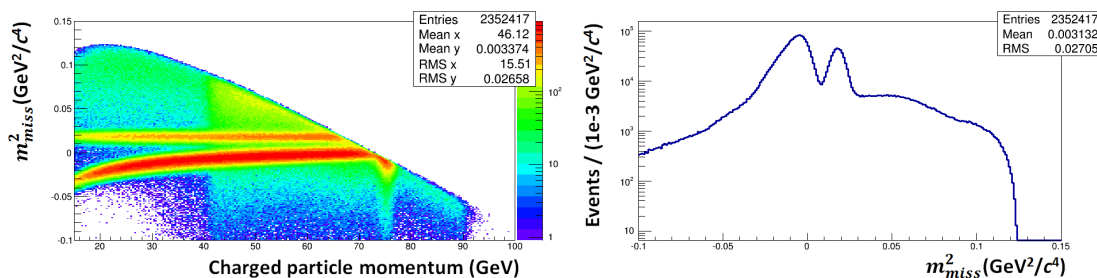


Figure 5.17: On the left the  $m_{miss}^2$  parameter of eq. 5.2 as a function of the momentum of the charged particle in the final state (e.g. the pion candidate). On the right the distribution of  $m_{miss}^2$ .

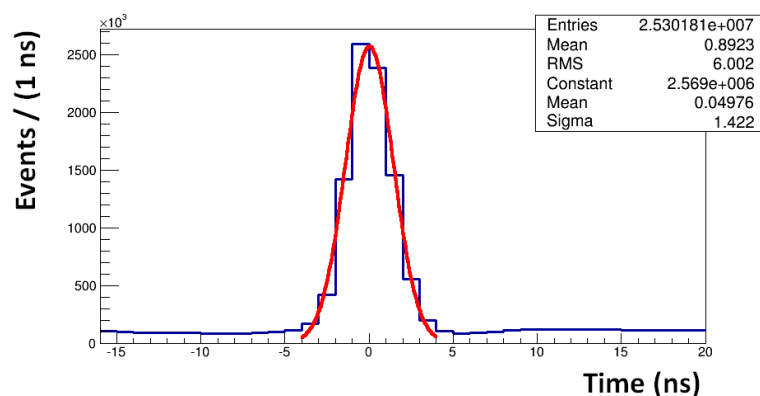


Figure 5.18: Distribution of time difference of CHOD and LKr clusters for run 3767. The gaussian fit on the peak has a sigma equal to 1.4 ns; thus when the time difference of of CHOD time and LKr cluster is in the range  $\pm 3\sigma$ , the LKr cluster are considered in time.

the LKr cluster and CHOD is less than 4.2 ns (see figure 5.18) and the space difference in X and Y between the LKr cluster position and the extrapolation of the track on the LKr plane is less than 3 cm (see figure 5.19).

Then a cut on the  $E/p$  value of the pion candidate (ratio of the energy released by the pion inside the LKr and the momentum measured with the straw) is applied. Figure 5.20 shows the  $E/p$  distribution for single track event with LKr cluster associated. The peak for low value of  $E/p$  is due to MIP, while the peak at  $E/p \sim 1$  is due to electrons or catastrophic Bremsstrahlung of muons; the central region between the peak is dominated by hadronic showers. Thus the events with

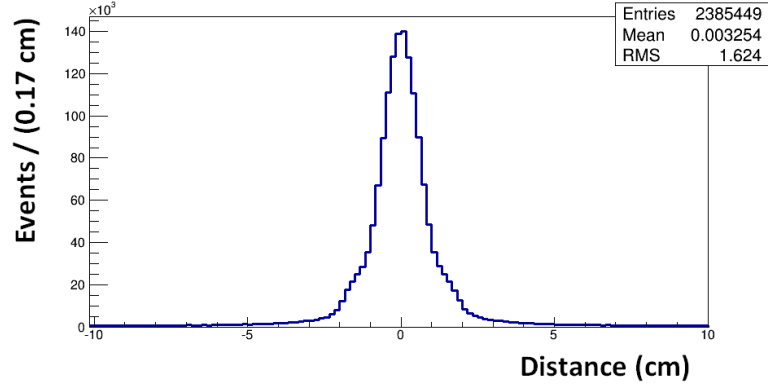


Figure 5.19: Distribution of Y space difference of LKr clusters and extrapolation of the track on the LKr plane for run 3767.

$E/p > 0.8$  are rejected.

In order to detect the two photons coming from the  $\pi^0 \rightarrow \gamma\gamma$  decay, just two clusters, different from the one associated with the STRAW track, are required in the LKr. These two clusters have to be time compatible with the CHOD candidate and not space compatible with the projection of track on the LKr plane; only cluster with an energy release greater than 3 GeV are considered in order to have a good time and space resolution of the cluster.

Finally events with a MUV3 candidate, with a time difference with respect to the CHOD less than 1.8 ns (see figure 5.21) and a space difference in X and Y with respect to extrapolation of track on the MUV3 plane less than 10 cm (see figure 5.22), are rejected. This allows the suppression of events with a muon in the final state.

It is still possible to use the information, provided by the LKr, of the X-Y position of the electromagnetic clusters associated with the two photons. Indeed the 4-momentum of the two photons, and so the 4-momentum  $P_{\pi^0}$  of the  $\pi^0$ , can be calculated using the position and the energy of the clusters and the kaon decay vertex. Thus another missing mass can be evaluated:

$$\overline{m_{miss}^2} = (P_K - P_{\pi^0})^2 \quad (5.3)$$

whose distribution, for the  $K_{2\pi}$  events, is expected to have a peak at  $m_{\pi^+}^2$ , where  $m_{\pi^+}$  is the mass of the charged pion ( $0.13957018 \pm 0.00000035$  GeV/ $c^2$  [71]). Figure 5.23 shows the distribution of  $\overline{m_{miss}^2}$  as a function of  $m_{miss}^2$ . In order to have a

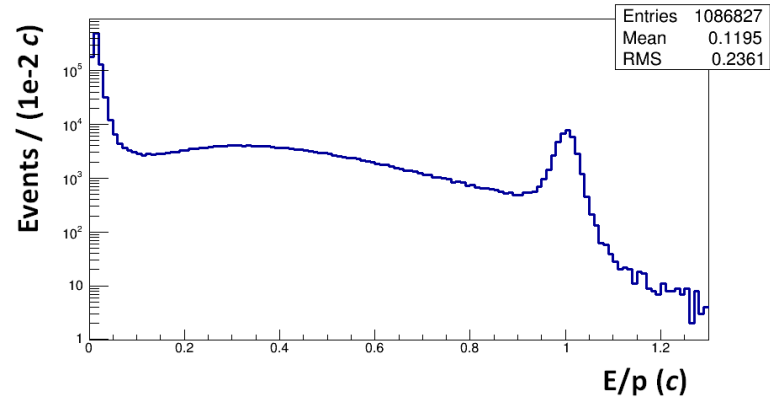


Figure 5.20: Distribution of  $E/p$  for the single track particle detected in the final state. Momentum is measured with STRAW, the energy release by the LKr.

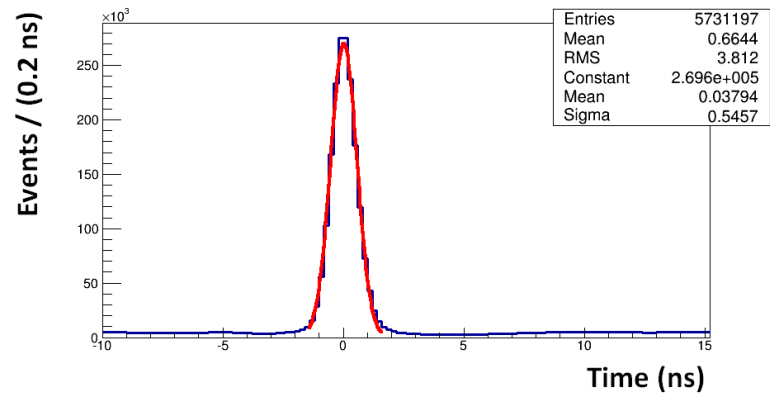


Figure 5.21: Distribution of time difference of CHOD and MUV3 candidates for run 3767. The gaussian fit on the peak has a sigma equal to 0.55 ns; thus when the time difference of of CHOD and MUV3 is in the range  $\pm 3\sigma$ , the MUV3 candidate is considered in time

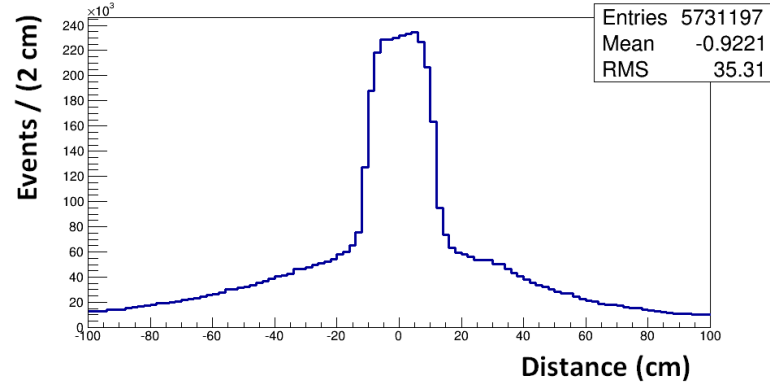


Figure 5.22: Distribution of X space difference between the MUV3 candidates and extrapolation of track on the MUV3 plane for run 3767.

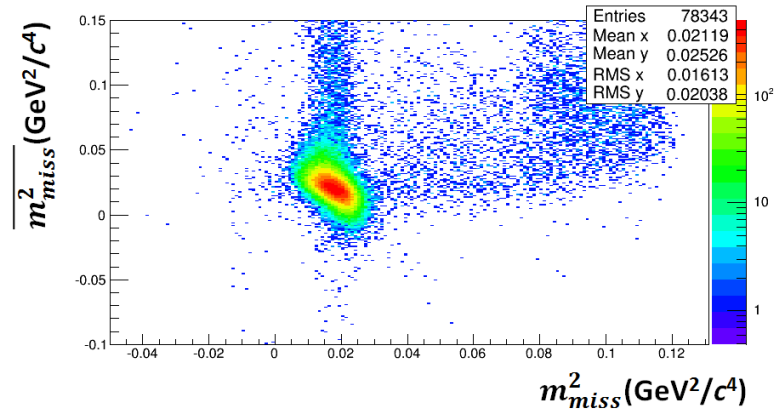


Figure 5.23: Distribution of  $\overline{m_{miss}^2}$  as a function of  $m_{miss}^2$ .

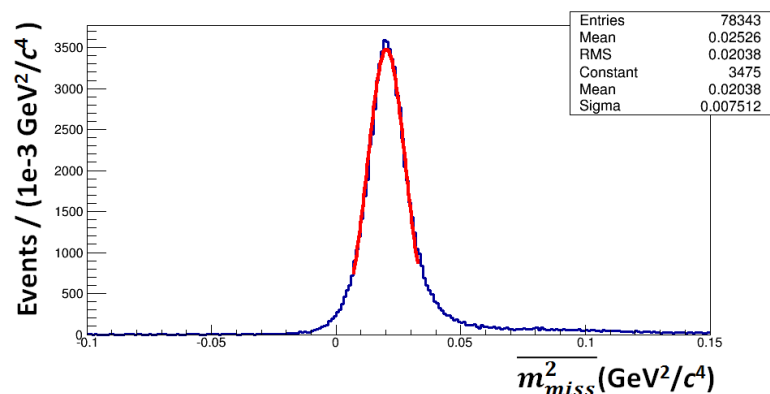


Figure 5.24: Distribution of  $\overline{m_{miss}^2}$  with a gaussian fit around the peak.

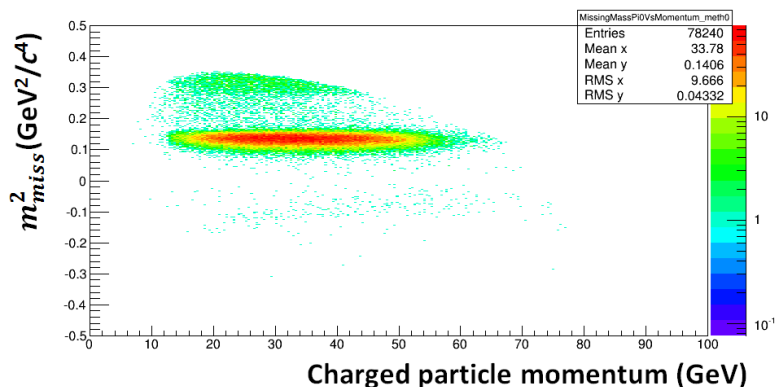


Figure 5.25: Distribution of  $m_{miss}^2$  parameter as a function of the momentum of the charged particle in the final state (e.g. the pion candidate) after all cuts for run 3767.

clean sample of  $K_{2\pi}$  process a cut on the  $\overline{m_{miss}^2}$  is applied: all the rejected events are the ones with  $\overline{m_{miss}^2}$  outside the  $\pm 5\sigma$  interval around the peak of the gaussian that fits the  $\overline{m_{miss}^2}$  distribution (see figure 5.24). After applying all the previous cuts, the distribution of the  $m_{miss}^2$  variable as a function of the momentum of the charged pion candidate for run 3767 becomes the one shown in figure 5.25. Figure 5.26 shows the  $m_{miss}^2$  distribution in the full pion momentum range (left) and for pion momentum between 15 GeV and 35 GeV (right), the one that will be used for the final  $K^+ \rightarrow \pi^+ \nu \bar{\nu}$  analysis. The same work has been done for the other runs 3810 and 4069: figures 5.27 and 5.28 show the final  $m_{miss}^2$  in the two different momentum ranges of the pion candidate.

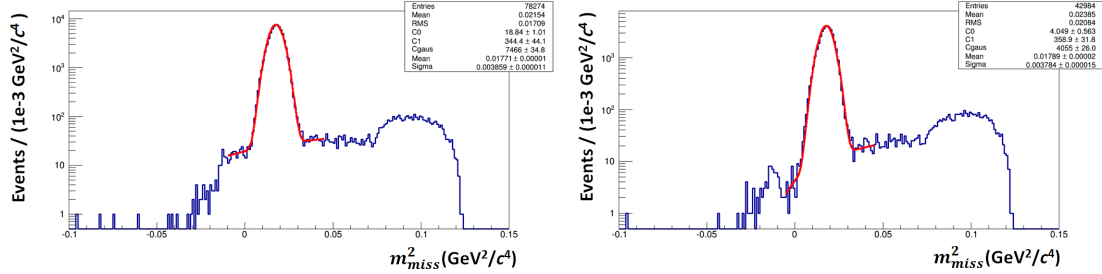


Figure 5.26:  $m^2_{miss}$  distribution in the full pion momentum range (left) and for pion momentum between 15 GeV and 35 GeV (right) for run 3767.

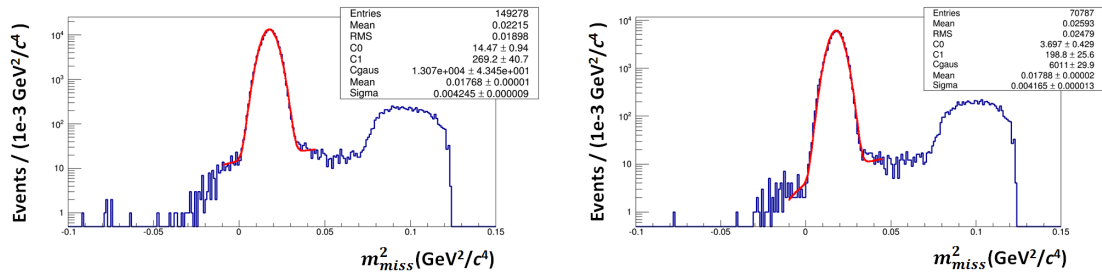


Figure 5.27:  $m^2_{miss}$  distribution in the full pion momentum range (left) and for pion momentum between 15 GeV and 35 GeV (right) for run 4068.

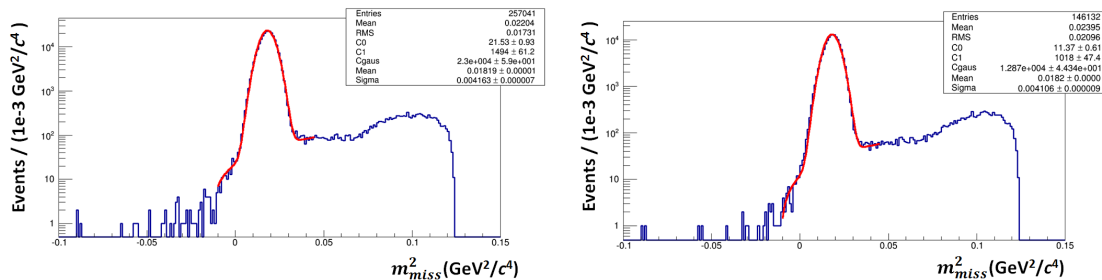


Figure 5.28:  $m^2_{miss}$  distribution in the full pion momentum range (left) and for pion momentum between 15 GeV and 35 GeV (right) for run 3810.

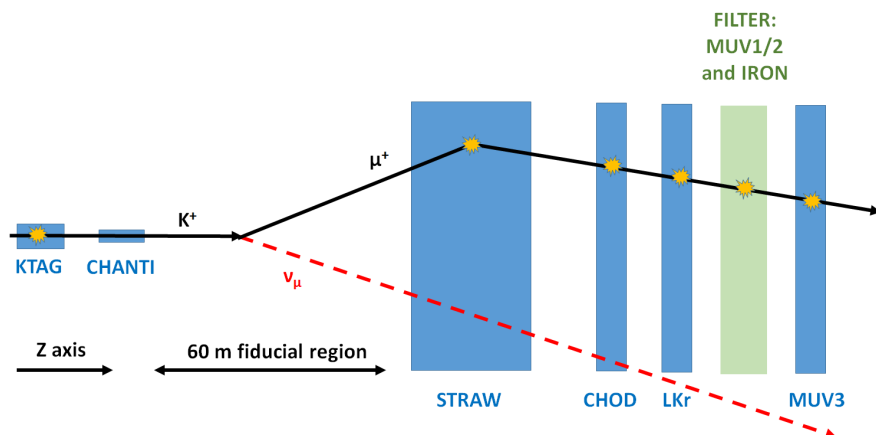


Figure 5.29: Topology of the  $K_{\mu 2}$  event. The kaon, identified by the KTAG, decays inside the fiducial volume. The  $\mu^+$  is in the geometrical acceptance of STRAW, CHOD, LKr and MUV3 and its momentum is measured by the STRAW; muon passes through the hadronic calorimeters (MUV1/2) and the iron layer and it releases energy inside MUV3.

In order to select  $K_{2\pi}$  events a cut on the  $m_{miss}^2$  is applied. A fit with a gaussian plus a linear function has been performed on the core of the  $m_{miss}^2$  distributions. The linear function represents a very simple model of the residual background for the  $K_{2\pi}$ , visible also at the side of the gaussian peaks. The region of events tagged as  $K_{2\pi}$  is chosen symmetric around the mean value of the gaussian function. Its width changes for the different analyzed runs in order to keep constant the ratio between signal and background.

### 5.5.2 Selection of $K_{\mu 2}$ sample

The  $K_{\mu 2}$  selection procedure follows the same steps described for the  $K_{2\pi}$  decay. So it uses again the CHOD, KTAG, STRAW, LKr and MUV3 detectors as shown in figure 5.29. First, events with one CHOD candidate and a kaon KTAG candidate in time are selected. Then only the "single track events" (see section 5.5.1) are considered in this analysis. At most one LKr cluster, that has to be associated in time and spaced with the track extrapolated on LKr plane, is accepted. When this cluster is found, the same cut on the  $E/p$  parameter has been used in order to reject electron-like tracks. Finally a MUV3 candidate compatible both in time and in space with the charged particle is also mandatory to identify the single muon

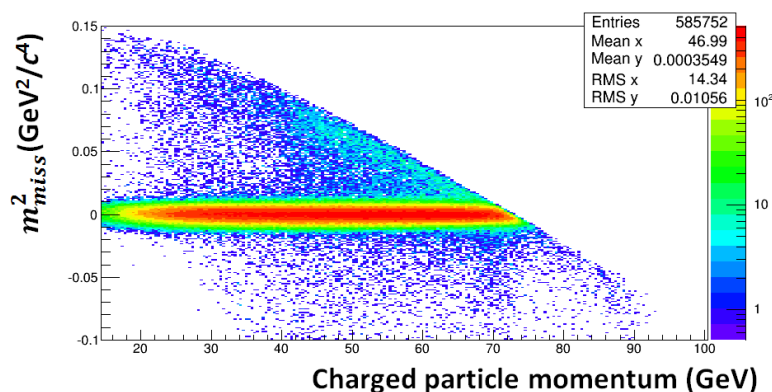


Figure 5.30: Distribution of  $m^2_{miss}$  parameter as a function of the momentum of the charged particle in the final state (e.g. the muon candidate) after all cuts for run 3767.

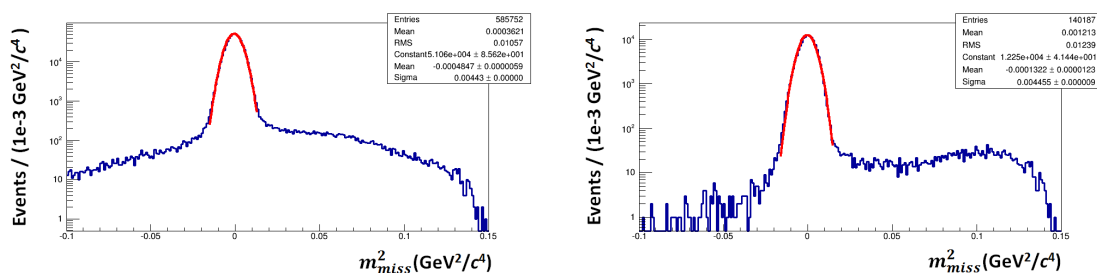


Figure 5.31:  $m^2_{miss}$  distribution in the full muon momentum range (left) and for muon momentum between 15 GeV and 35 GeV (right) for run 3767.

in the final state.

In this case the missing mass variable is evaluated with the muon hypothesis for the charged particle detected by STRAW. The distribution of the  $m^2_{miss}$  as a function of the momentum of the charged muon candidate is shown in figure 5.30 for the run 3767. Figure 5.31 shows the  $m^2_{miss}$  distribution in the whole muon momentum range (left) and for muon momentum between 15 GeV and 35 GeV (right). The same work has been done for the other runs: figures 5.32 (run 4068) and 5.33 (run 3810) show the final  $m^2_{miss}$  in the two different momentum ranges of the muon candidate.

In order to select  $K_{\mu 2}$  events a cut on the  $m^2_{miss}$  is applied. For this channel just a simple gaussian fit has been performed on the core of the  $m^2_{miss}$  distributions. Then the region of events tagged as  $K_{\mu 2}$  is chosen symmetric ( $\pm 3\sigma$  of the gaussian

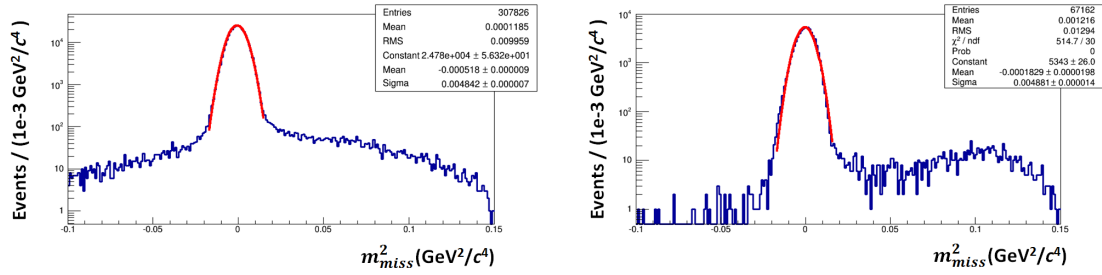


Figure 5.32:  $m^2_{miss}$  distribution in the full muon momentum range (left) and for muon momentum between 15 GeV and 35 GeV (right) for the run 4068.

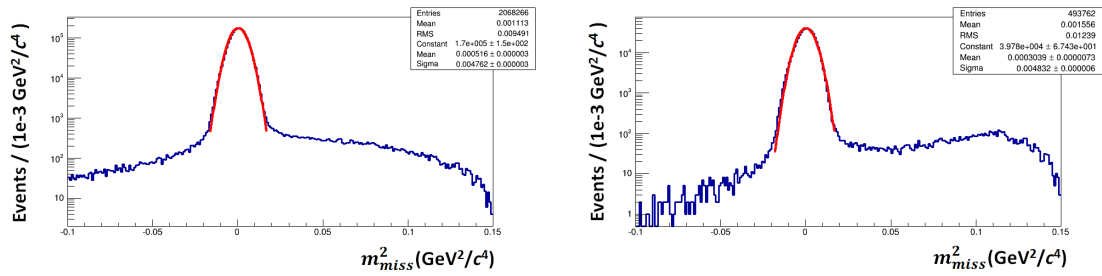


Figure 5.33:  $m^2_{miss}$  distribution in the full muon momentum range (left) and for muon momentum between 15 GeV and 35 GeV (right) for the run 3810.

distribution) around the mean value.

### 5.5.3 CHANTI fake veto for $K_{2\pi}$ and $K_{\mu 2}$

Once the  $K_{2\pi}$  and  $K_{\mu 2}$  samples have been selected, it is possible to evaluate the accidental veto introduced by CHANTI. The procedure consists in counting the number of time a CHANTI candidate is fired in a time window around a given reference time; for the CHANTI the reference time is given by the KTAG candidate in which the kaon of the  $K_{2\pi}$  or the  $K_{\mu 2}$  process has been recognized. Thus the time window is centered around this reference time with a half time width equal to  $\Delta t$ . Two different definition of "CHANTI fired" can be used.

**Single** CHANTI is fired when at least one bar is fired in the given time window.

**Cross** CHANTI is fired when at least one candidate in one CHANTI station (see section 5.2 for CHANTI candidate definition) with a well defined X-Y position is fired. This means that there are at least two crossing bars, belonging to the same CHANTI station but different layer, fired at the same time.

Figure 5.34 shows the fraction of  $K_{2\pi}$  events (without any cut on the momentum range of the pion) that would be vetoed by CHANTI in **Single**(left) and **Cross**(right) configuration as a function of  $\Delta t$  for the run 3767. Figure 5.35 shows the same quantity considering  $K_{2\pi}$  events with the pion momentum between 15 GeV and 35 GeV. The same plots are reported for the runs 4068 (see figure 5.36 and 5.37) and 3810 (see figure 5.38 and 5.39).

Similar plots for the  $K_{\mu 2}$  channel are shown in figure 5.40, 5.41, 5.42, 5.43, 5.44, 5.45.

As expected the cut with **Single** configuration introduces a high accidental veto due to quasi-elastic event. The values of the fraction of vetoed events for a  $\Delta t=3$  ns, corresponding to three times the time resolution of the CHANTI, are reported in table 5.1 for the **Cross** configuration and a momentum range, for the charged particle in the finale state, between 15 GeV and 35 GeV. The accidental veto increases with beam intensity in a non linear way: it increases by a factor of 20 while the beam intensity scales by a factor of 40. The reason for this non linearity results are more clear by comparing figures 5.34 and 5.35 with figures 5.38

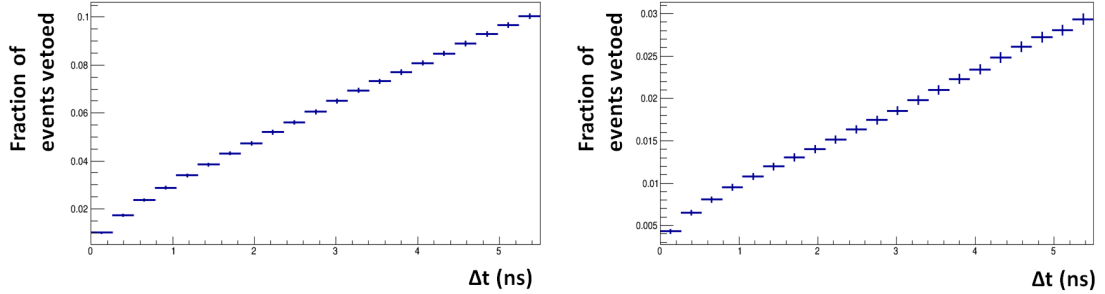


Figure 5.34: Fraction of  $K_{2\pi}$  events (without any cut on pion momentum) that would be vetoed by CHANTI in **Single**(left) and **Cross**(right) configuration as a function of  $\Delta t$  for the run 3767.

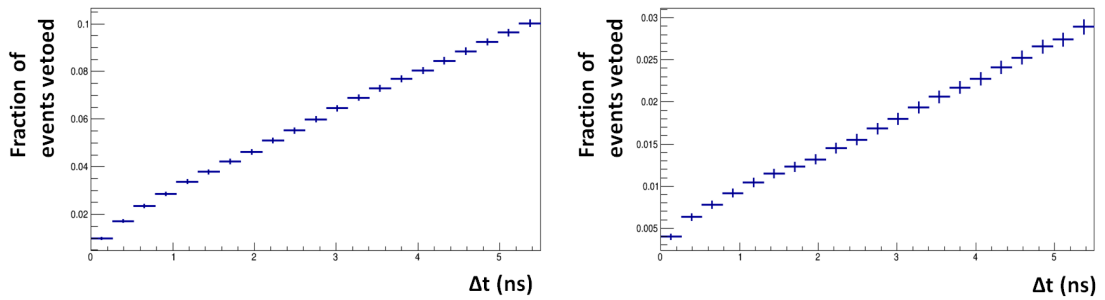


Figure 5.35: Fraction of  $K_{2\pi}$  events, with a pion momentum between 15 GeV and 35 GeV, that would be vetoed by CHANTI in **Single**(left) and **Cross**(right) configuration as a function of  $\Delta t$  for the run 3767.

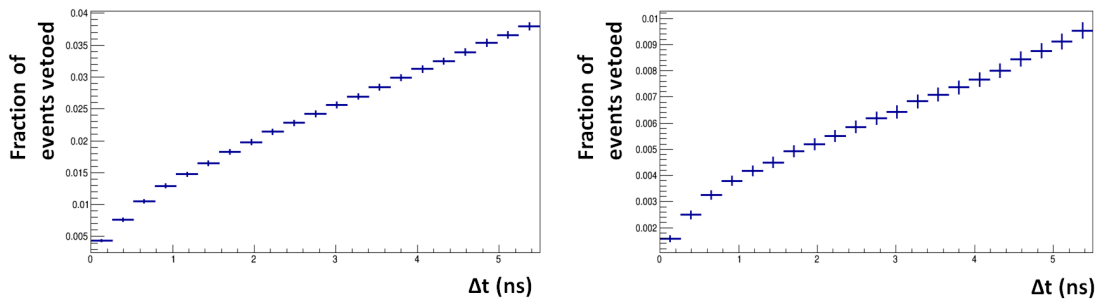


Figure 5.36: Fraction of  $K_{2\pi}$  events (without any cut on pion momentum) that would be vetoed by CHANTI in **Single**(left) and **Cross**(right) configuration as a function of  $\Delta t$  for the run 4068.

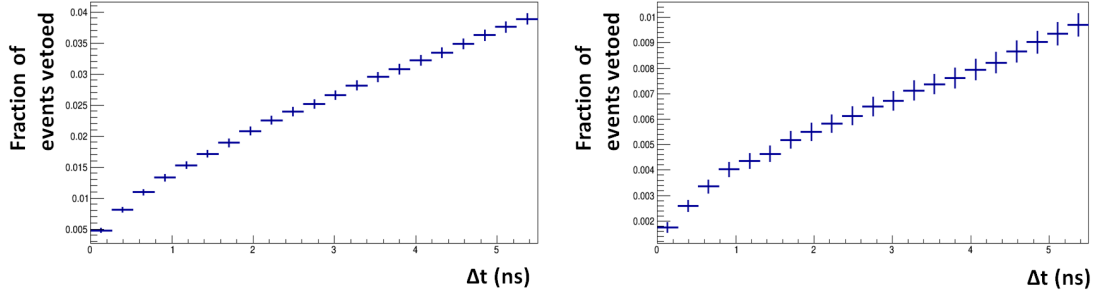


Figure 5.37: Fraction of  $K_{2\pi}$  events, with a pion momentum between 15 GeV and 35 GeV, that would be vetoed by CHANTI in **Single**(left) and **Cross**(right) configuration as a function of  $\Delta t$  for the run 4068.

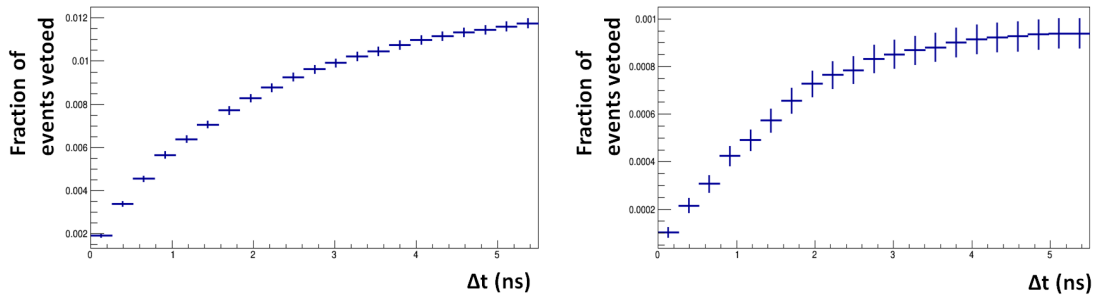


Figure 5.38: Fraction of  $K_{2\pi}$  events (without any cut on pion momentum) that would be vetoed by CHANTI in **Single**(left) and **Cross**(right) configuration as a function of  $\Delta t$  for the run 3810.

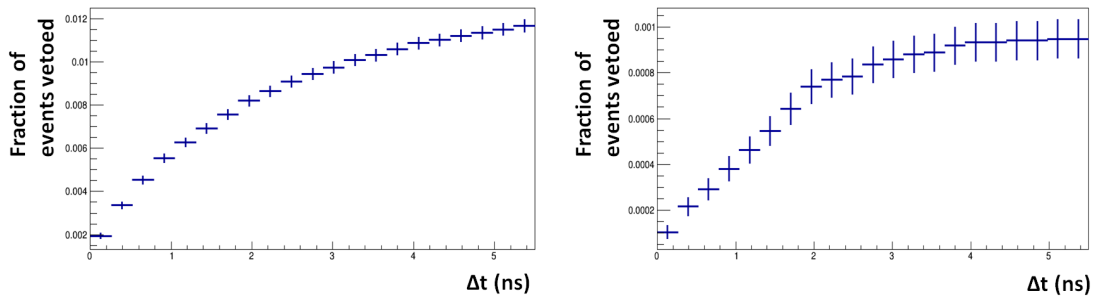


Figure 5.39: Fraction of  $K_{2\pi}$  events, with a pion momentum between 15 GeV and 35 GeV, that would be vetoed by CHANTI in **Single**(left) and **Cross**(right) configuration as a function of  $\Delta t$  for the run 3810.

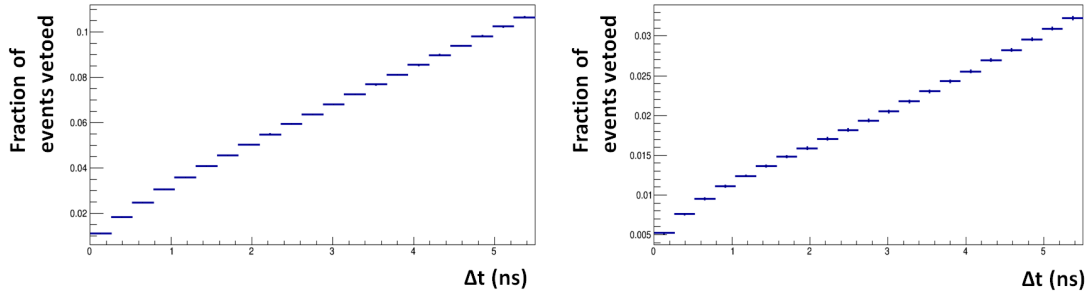


Figure 5.40: Fraction of  $K_{\mu 2}$  events (without any cut on the muon momentum) that would be vetoed by CHANTI in **Single**(left) and **Cross**(right) configuration as a function of  $\Delta t$  for the run 3767.

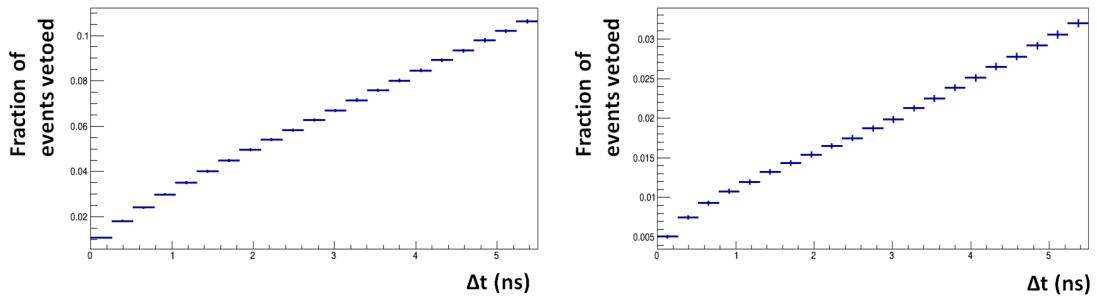


Figure 5.41: Fraction of  $K_{\mu 2}$  events, with a muon momentum between 15 GeV and 35 GeV, that would be vetoed by CHANTI in **Single**(left) and **Cross**(right) configuration as a function of  $\Delta t$  for the run 3767.

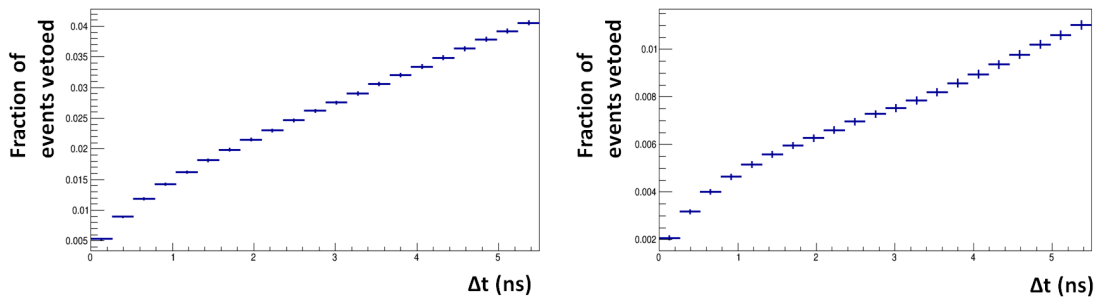


Figure 5.42: Fraction of  $K_{\mu 2}$  events (without any cut on the muon momentum) that would be vetoed by CHANTI in **Single**(left) and **Cross**(right) configuration as a function of  $\Delta t$  for the run 4068.

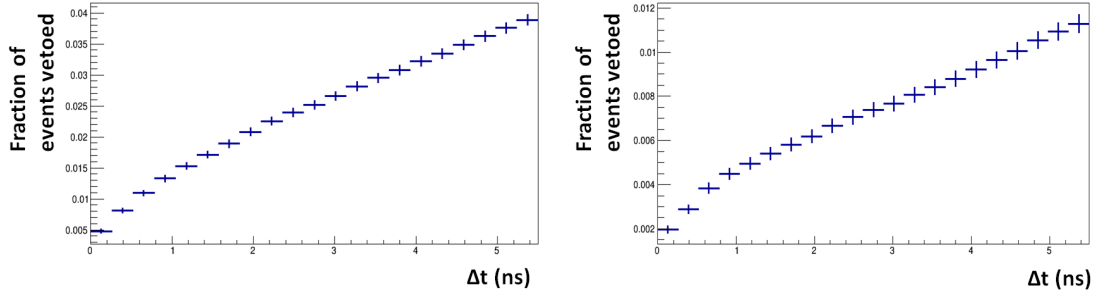


Figure 5.43: Fraction of  $K_{\mu 2}$  events, with a muon momentum between 15 GeV and 35 GeV, that would be vetoed by CHANTI in **Single**(left) and **Cross**(right) configuration as a function of  $\Delta t$  for the run 4068.

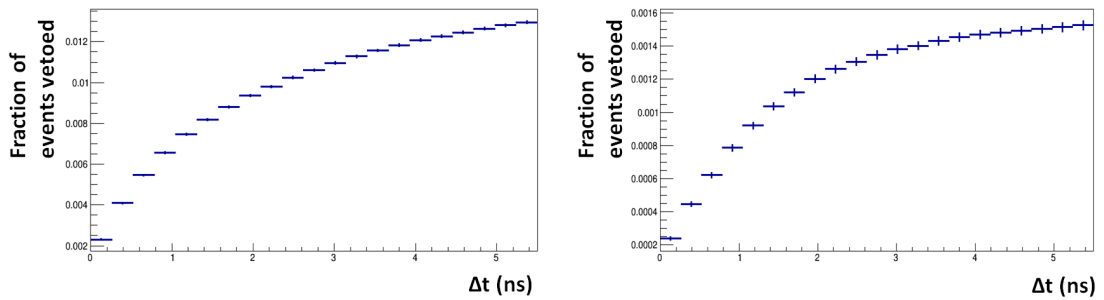


Figure 5.44: Fraction of  $K_{\mu 2}$  events (without any cut on the muon momentum) that would be vetoed by CHANTI in **Single**(left) and **Cross**(right) configuration as a function of  $\Delta t$  for the run 3810.

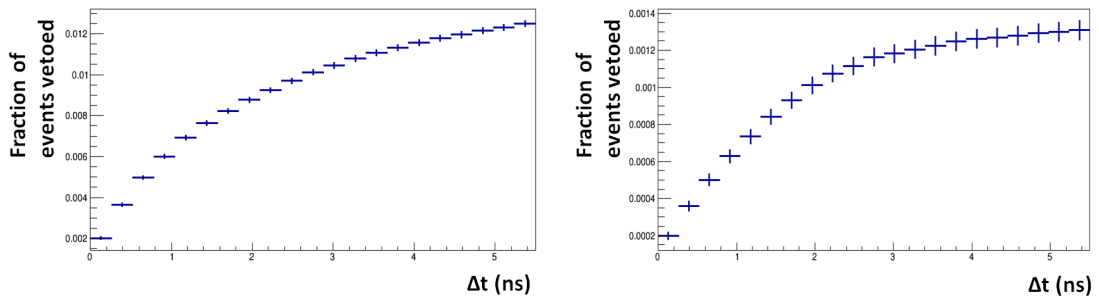


Figure 5.45: Fraction of  $K_{\mu 2}$  events, with a muon momentum between 15 GeV and 35 GeV, that would be vetoed by CHANTI in **Single**(left) and **Cross**(right) configuration as a function of  $\Delta t$  for the run 3810.

Beam Intensity	$K_{2\pi}$	$K_{\mu 2}$
1%	0.085%	0.12%
10%	0.7%	0.8%
40%	1.8%	2%

Table 5.1: Fraction of events vetoed by CHANTI with a  $\Delta t = 3$  ns for the **Cross** configuration.

and 5.39. At low intensity (figures 5.38 and 5.39) a clear peak of activity correlated in time with the KTAG candidate is observed in the CHANTI (steeper slope below 2 ns), above a flat accidental coincidence rate which increases more slowly and proportionally to the time window  $\Delta t$  (above 2 ns). The latter coincidences are generated by muons from beam halo crossing the CHANTI and pileup events where a pion (or proton, or another kaon) of the beam interacts with the GTK while the kaon, tagged by KTAG, is crossing it. The fraction of activity correlated in time with the KTAG is of course the fraction of kaons quasi-elastic and inelastic interactions observed by CHANTI. Thus it does not depend on beam intensity because it is only related to the kaon cross section on GTK material and to the CHANTI acceptance. On the other hand the fraction of pileup and halo events in a fixed  $\Delta t$  interval obviously increases with intensity and dominates the fraction of vetoed events in figures 5.34 and 5.35, which thus show an almost linear trend with  $\Delta t$ . With this in mind one can expect that at full intensity roughly 5% of the kaon decays will be vetoed by a  $\Delta t = 3$  ns time window on CHANTI.

# Conclusions

This work was focussed on the design, development, construction, simulation and testing of the detector CHANTI. Almost all the steps of the realization of a particle physics detector have been touched during my PhD research. The detector has been proposed by Naples group in the NA62 experiment in order to reduce the background induced by beam inelastic interactions with the beam spectrometer. In this thesis the design philosophy, the construction procedure and the quality tests, adopted during the assembly of the detector, are reported. The basic CHANTI structure is a triangular shape scintillating bar read by a WLS fiber coupled to a SiPM. The simulation of the detector, implemented to evaluate data rate, led to a change in the CHANTI design since some long bars were divided into two halves in order to satisfy the front-end electronics requirements. The data acquired for the characterization of the bars have been used to develop a simulation of the scintillating bar, including all the optical processes, and the complete digitization of the signals produced.

A careful calibration procedure for the CHANTI-FE and ToT boards has been setup in order to precisely control and readout the value of the bias voltage and threshold setting and to monitor the current of each channel. In particular the hysteresis measurement procedure has been used by all the detectors that have the ToT boards in the front-end electronics. It has been very useful because it led to the discovery of a mistake in the design of the comparator inside the board. The full calibration scheme was finally validated by counting the dark rate of SiPM at different values of the threshold.

Finally CHANTI has been installed in June 2014 on the beam line in the North Area at CERN and it started to take data with beam during the Pilot run of the NA62 experiment occurred in October 2014. During this first run the commissioning of the detector was completed and it was ensured the capability of CHANTI to

take data in the experimental environment. Then in 2015, first real data useful for the analysis were acquired and they were used in order to evaluate the main figures of merit for the detector. It has been shown that the single layer efficiency resulted  $> 0.99$ : this ensures that the CHANTI inefficiency for detecting a charged particle, passing through both layers of a station, is well below the  $O(0.1\%)$  geometrical inefficiency of the detector [62]. It was proved that the CHANTI candidate, that is the basic element of the data analysis defined as an appropriate bars cluster, can reach a time resolution  $\sigma_t$  below 1 ns. Then also the spatial resolution of the detector has been evaluated, which is relevant to select pure control samples of inelastic and beam halo events: a result of  $\sigma_{x/y} \simeq 2.5$  mm has been obtained. Finally, selecting samples of  $K_{2\pi}$  and  $K_{\mu 2}$  events, the accidental veto introduced has been calculated. A clear evidence was that two bars crossing in one station should be the minimal requirements to perform a veto with this detector because of the quasi-elastic events of beam particle. A dependence of this parameter on the beam intensity has been shown: at 40% beam intensity the fake veto introduced by CHANTI is less than 2% with a time window around the reference time equal to  $\pm 3\sigma_t$ .

The construction, setup and commissioning phase of the detector ended successfully with this work. Now another phase regarding data analysis starts whose groundwork has already been layed here. The CHANTI, in fact, beyond acting as a veto can play a relevant role in the selection of control samples of inelastic events, by exploiting its tracking and timing capabilities. The exploiting of this potential has just started, preliminary results have been shown at last NA62 Analysis Meeting in March 2016 [72].

# Bibliography

- [1] G. D. Rochester and C. C. Butler, *Evidence for the existence of new unstable elementary particles*, Nature 160 (1947) 855-857
- [2] *CHANTI: a fast and efficient charged particle veto detector for the NA62 experiment at CERN*, Journal of Instrumentation, Volume 11, P03029, March 2016, <http://dx.doi.org/10.1088/1748-0221/11/03/P03029>
- [3] A.J. Buras, D. Buttazzo, J. Girrbach-Noe, R. Knegjens,  $K^+ \rightarrow \pi^+ \nu \bar{\nu}$  and  $K_L \rightarrow \pi^0 \nu \bar{\nu}$  in the Standard Model: Status and Perspective, arXiv:1503.02693[hep-ph]
- [4] G. Isidori, F. Mescia, P. Paradisi, C. Smith, and S. Trine, JHEP 0608, 064 (2006)
- [5] M. Blanke, A. J. Buras, B. Duling, S. Recksiegel, and C. Tarantino, Acta Phys. Polon. B 41, 657 (2010).
- [6] A. V. Artamonov et al., Phys. Rev. D 79, (E949 collaboration), 092004 (2009).
- [7] M. Kobayashi, T. Maskawa, Prog. Theor. Phys. 49, 652 (1973).
- [8] L. Wolfenstein, Phys. Rev. Lett. 51, 1945 (1983).
- [9] J. Beringer et al., Phys. Rev. D 86, (Particle Data Group), 010001 (2012).
- [10] A. Abulencia et al., Phys. Rev. Lett. 97, 242003 (2006).
- [11] R. Aaij et al., Phys. Lett. B 709, 177 (2012).
- [12] G. Buchalla and A. J. Buras, *The rare decays  $K \rightarrow \pi \nu \bar{\nu}$ ,  $B \rightarrow X \nu \bar{\nu}$  and  $B \rightarrow l^+ l^-$ : An Update*, Nucl. Phys. B548 309 (1999) [hep-ph/9901288].
- [13] G. Buchalla and A. J. Buras,  *$K \rightarrow \pi \nu \bar{\nu}$  and high precision determinations of the CKM matrix*, Phys. Rev. D54 (1996) 6782-6789, [hep-ph/9607447]
- [14] G. Buchalla, A. J. Buras, and M. E. Lautenbacher, *Weak decays beyond leading logarithms*, Rev. Mod. Phys. 68 (1996) 1125-1144, [hep-ph/9512380]
- [15] G. Buchalla and A. J. Buras.  $\sin 2\beta$  from  $K \rightarrow \pi \nu \bar{\nu}$ . In: Physics Letters B 333.1-2 (1994), pp. 221-227. DOI: [http://dx.doi.org/10.1016/0370-2693\(94\)91034-0](http://dx.doi.org/10.1016/0370-2693(94)91034-0).

- [16] F. Mescia and C. Smith, *Improved estimates of rare K decay matrix-elements from  $K_{l3}$  decays*, Phys. Rev. D76 (2007) 034017, [arXiv:0705.2025].
- [17] G. Buchalla and A. J. Buras, *QCD corrections to rare K and B decays for arbitrary top quark mass*, Nucl. Phys. B400 (1993) 225-239.
- [18] M. Misiak and J. Urban, *QCD corrections to FCNC decays mediated by Z penguins and W boxes*, Phys. Lett. B451 (1999) 161-169, [hep-ph/9901278].
- [19] J. Brod, M. Gorbahn, and E. Stamou, *Two-Loop Electroweak Corrections for the  $K \rightarrow \pi\nu\bar{\nu}$  Decays*, Phys. Rev. D83 (2011) 034030, [arXiv:1009.0947].
- [20] D. Buttazzo, G. Degrassi, P. P. Giardino, G. F. Giudice, F. Sala, et al., *Investigating the near-criticality of the Higgs boson*, JHEP 1312 (2013) 089, [arXiv:1307.3536].
- [21] G. Isidori, F. Mescia, and C. Smith, *Light-quark loops in  $K \rightarrow \pi\nu\bar{\nu}$* , Nucl. Phys. B718 (2005) 319-338, [hep-ph/0503107].
- [22] J. Bijnens and K. Ghorbani., *Isospin breaking in  $K\pi$  vector form-factors for the weak and rare decays  $K_{l3}$ ,  $K \rightarrow \pi\nu\bar{\nu}$  and  $K \rightarrow \pi l^+ l^-$* . In: (2007). arXiv: 0711.0148 [hep-ph].
- [23] G. Buchalla and A. J. Buras, *The rare decays  $K^+ \rightarrow \pi^+\nu\bar{\nu}$  and  $K_L \rightarrow \mu^+\mu^-$  beyond leading logarithms*, Nucl. Phys. B412 (1994) 106-142,[hep-ph/9308272].
- [24] A. J. Buras, M. Gorbahn, U. Haisch, and U. Nierste, *The rare decay  $K^+ \rightarrow \pi^+\nu\bar{\nu}$  at the next-to-next-to-leading order in QCD*, Phys. Rev. Lett. 95 (2005) 261805, [hep-ph/0508165].
- [25] A. J. Buras, M. Gorbahn, U. Haisch, and U. Nierste, *Charm quark contribution to  $K^+ \rightarrow \pi^+\nu\bar{\nu}$  at next-to-next-to-leading order*, JHEP 11 (2006) 002, [hep-ph/0603079].
- [26] J. Brod and M. Gorbahn, *Electroweak Corrections to the Charm Quark Contribution to  $K^+ \rightarrow \pi^+\nu\bar{\nu}$* , Phys. Rev. D78 (2008) 034006,[arXiv:0805.4119].
- [27] K. Chetyrkin, J. Kuhn, A. Maier, P. Maierhofer, P. Marquard, et al., *Charm and Bottom Quark Masses: An Update*, Phys. Rev. D80 (2009) 074010, [arXiv:0907.2110].
- [28] Particle Data Group Collaboration, J. Beringer et al.,*Review of Particle Physics (RPP)*, Phys. Rev. D86 (2012) 010001. <http://pdg.lbl.gov>.
- [29] UTfit Collaboration, M. Bona et al., *The Unitarity Triangle Fit in the Standard Model and Hadronic Parameters from Lattice QCD: A Reappraisal after the Measurements of  $\Delta m(s)$  and  $BR(B \rightarrow \tau\nu_{\tau}au)$* , JHEP 0610 (2006) 081, [hep-ph/0606167]. Updates on <http://www.utfit.org>.

- [30] J. Charles et al., *Current status of the Standard Model CKM fit and constraints on  $\Delta F = 2$  New Physics*, Phys. Rev. D91 (2015) 073007, [arXiv:1501.05013]. Updates on <http://ckmfitter.in2p3.fr>.
- [31] M. Togawa, *Status of KOTO Experiment at J-PARC*, In: Journal of Physics: Conference Series 556.1 (2014), p. 012046.
- [32] M. Blanke, *Insights from the Interplay of  $K \rightarrow \pi\nu\bar{\nu}$  and  $\epsilon_K$  on the New Physics Flavour Structure*, Acta Phys.Polon. B41 (2010) 127, [arXiv:0904.2528].
- [33] R. Barbieri, D. Buttazzo, F. Sala, and D. M. Straub, *Flavour physics and flavour symmetries after the first LHC phase*, JHEP 1405 (2014) 105, [arXiv:1402.6677].
- [34] M. Blanke, A. J. Buras, B. Duling, S. Recksiegel, and C. Tarantino, *FCNC Processes in the Littlest Higgs Model with T-Parity: a 2009 Look*, Acta Phys.Polon. B41 (2010) 657-683, [arXiv:0906.5454].
- [35] A. J. Buras, F. De Fazio, and J. Girrbach, *The Anatomy of  $Z'$  and  $Z$  with Flavour Changing Neutral Currents in the Flavour Precision Era*, JHEP 1302 (2013) 116, [arXiv:1211.1896].
- [36] A. J. Buras, D. Buttazzo, J. Girrbach-Noe, and R. Knegjens, *Can we reach the Zeptouniverse with rare  $K$  and  $B_{s,d}$  decays?*, JHEP 1411 (2014) 121, [arXiv:1408.0728].
- [37] M. Blanke, A. J. Buras, B. Duling, K. Gemmler, and S. Gori, *Rare  $K$  and  $B$  Decays in a Warped Extra Dimension with Custodial Protection*, JHEP 03 (2009) 108, [arXiv:0812.3803].
- [38] A. J. Buras, D. Buttazzo, and R. Knegjens,  *$K \rightarrow \pi\nu\bar{\nu}$  and  $\epsilon'/\epsilon$  in Simplified New Physics Models*, arXiv:1507.08672.
- [39] J. Charles et al., *CP violation and the CKM matrix: assessing the impact of the asymmetric  $B$  factories.*, In: The European Physical Journal C - Particles and Fields 41.1 (2005), pp. 1-131. DOI: 10.1140/epjc/s2005-02169-1.
- [40] A. V. Artamonov et al., Phys. Rev. D 79, (E949 collaboration), 092004 (2009).
- [41] H. W. Atherton et al., *Precise measurements of particle production by 400 GeV/c protons on beryllium targets*, tech. rep., CERN Yellow Report: CERN 80-07 (1980).
- [42] E. Cortina et al., *NA62: Technical design document*, NA62-10-07, CERN, (2010), <http://na62.web.cern.ch/na62/Documents/TechnicalDesign.html>.
- [43] K. Ahmet et al., Nucl. Instrum. and Meth. A 305, OPAL Collaboration, 275 (1991).

- [44] F. Ambrosino et al., *The Large-Angle Photon Veto System for the NA62 Experiment at CERN*, arXiv:1111.4075
- [45] NA48 collaboration, *The Beam and Detector for the NA48 Neutral Kaon CP Violation Experiment at CERN*, NIM A574, pp. 433-471, (2007).
- [46] G. S. Atoian et al., Nucl. Instrum. Meth. A 531, 467 (2004).
- [47] B. Angelucci et al., *Pion-Muon separation with a RICH prototype for the NA62 experiment*, Nucl. Instrum. Meth. A 621, pp. 205-211 (2010).
- [48] Sozzi M., *A concept for the NA62 Trigger and Data Acquisition*. NA62Note 07-03 (2007).
- [49] [<http://ttc.web.cern.ch/TTC/intro.html>], *TTC: Timing, Trigger and Control Systems for LHC Detectors*.
- [50] M Pivanti et al., *Implementation of a PC-based Level 0 Trigger Processor for the NA62 Experiment.*, Journal of Physics: Conference Series 513.1 (2014), p. 012008.
- [51] D. Beznosko, A. Bross, A. Dyshkant, A. Pla-Dalmau, and V. Rykalin, *FNAL-NICADD extruded scintillator.*, 2004 IEEE Nuclear Science Symposium and Medical Imaging Conference (NSS / MIC), October, 16–22, 2004 Rome, Italy.
- [52] MINERVA Collaboration, MINERVA document 218-v4 (2006)
- [53] D0 Collaboration, Nucl. Instrum. Methods A565 (2006) 413
- [54] A. Pla-Dalmau, A. Bross and V. Rykalin, *Extruding plastic scintillator at Fermilab.*, prepared for IEEE Nuclear Science Symposium Conference Record (2003)
- [55] <http://outgassing.nasa.gov/>
- [56] <http://www.detectors.saint-gobain.com/fibers.aspx>, Saint-Gobain Crystals
- [57] Ronchetti (on behalf of the ALICE collaboration), Journal of Physics Conferences Series 160012012 (2009)
- [58] V. Palladino, *Simulation, realization and test of veto systems for NA62 experiment*. Ph D. Thesis 2010.
- [59] <http://www.fluka.org/fluka.php>, Fluka Home Page.
- [60] <http://geant4.web.cern.ch/geant4/>, Geant4 Home Page.
- [61] <http://www.keithley.it/products/dcac/currentvoltage/2400smu/?mn=2410>
- [62] D. Di Filippo, *Simulation and test of the CHANTI detector for the measurement of the ultra-rare branching ratio with  $K^+ \rightarrow \pi^+ \nu \bar{\nu}$  the NA62 experiment at CERN*. Ph D. Thesis 2011.

- [63] A. Antonelli et al., *The NA62 LAV front-end electronics.*, 2012 JINST 7 C01097 .
- [64] <http://www.ietlabs.com/decaderes/decade-resistor/hrrs-series-high-resistance-decade-box.html>
- [65] <http://www.tek.com/signal-generator/afg3000-function-generator>
- [66] [www.caen.it/csite/CaenProd.jsp?idmod=787&parent=11](http://www.caen.it/csite/CaenProd.jsp?idmod=787&parent=11)
- [67] Marco Mirra, *Simulation and test of the CHANTI detector for the measurement of the ultra-rare branching ratio  $K^+ \rightarrow \pi^+ \nu \bar{\nu}$  with the NA62 experiment at CERN*, Università degli Studi di Napoli "Federico II", Master Thesis, 2013
- [68] <http://www.hamamatsu.com>
- [69] <http://www.fft.w.org/>
- [70] F. Ambrosino et al, *The CHarged AntiCounter for the NA62 experiment at CERN.*, prepared for *14th ICATPP Conference on Astroparticle, Particle, Space Physics and Detector for Physics Application.* September, 23–27, 2013 Villa Olmo Como, Italy.
- [71] K.A. Olive et al., *Particle Data Group*, Chin. Phys. C, 38, 090001 (2014) and 2015 update.
- [72] M. Corvino, *CHANTI status and data analysis*, Presentation at NA62 Analysis Meeting, March 2016, <http://indico.cern.ch/event/506080/>